

https://dspace.org/

The interaction of three-dimensional vortex flows

Cooppan, Sambharthan

2014-09-02
http://hdl.handle.net/10539/15359

Downloaded from a DSpace repository. https://dspace.org/

The Interaction of Three-Dimensional Vortex Flows

Sambharthan Cooppan

A dissertation submitted to the Faculty of Engineering and the Built Environment, University of the Witwatersrand, Johannesburg, in fulfilment of the requirements for the degree of Master of Science in Engineering.

Johannesburg, March 2014

Declaration

I declare that this dissertation is my own, unaided work, except where otherwise acknowledged. It is being submitted for the degree of Master of Science in Engineering in the University of the Witwatersrand, Johannesburg. It has not been submitted before for any degree or examination at any other university.

Signed this __ day of _____ 20__

_____

Sambharthan Cooppan.

Acknowledgements

I would like to thank Professor Skews for firstly allowing me to work on such an interesting and challenging topic, secondly for his patience, guidance and positive feedback throughout my Masters, and finally for helping to get my Masters funded.

A big thanks goes to Randall Paton for teaching me how to use the equipment and help in setting up my computational simulations.

Armscor sponsored me and my Masters through the Fluxion program. This has made my life a lot easier and more enjoyable.

The Mechanical laboratory staff always has a high work ethic and have helped me out in times when I have really needed it. A special thanks goes to Shaun Riekert, Lionel Claassen and Marius Van Wyk.

Finally I would like to thank all my family and friends who have supported me throughout my Masters; especially my mother, sister and brother.

Abstract

The interaction of three dimensional vortex flows was investigated through vortex shedding off a discontinuous edge. Two 90° edges (up and downstream edges) were separated by an offset. The size of the offset (5mm, 10mm and 20mm) and the Mach number (Mach 1.32, 1.42 and 1.6) were the key parameters investigated. Experimental images were taken and computational simulations were run; a close relation was found between the two. This enabled the three dimensional effects of the flow to be studied and analysed. It was found, as the offset increased in size; the vortices shed off the up and downstream edges took a longer time to merge and the strength of the interaction was weaker. The vortex topology changed with a larger offset; the downstream vortex was thinner (in terms of cross sectional diameter), which is an indication of a change in denisty, than the rest of the vortex along the downstream diffraction edge, adjacent to the offset. This particular feature was more prevalent at lower Mach numbers. The effects of a higher Mach number were to increase the rate of dissipation of the vortices, lengthen the shear layer and make the vortex profile elliptical.

Published Work

Aspects of this thesis have been published in the following references:

1. Cooppan, S. & Skews, B. W. (2012). Interaction of Three-Dimensional Compressible Vortices. *30th International Congress on High-Speed Imaging and Photonics*. Pretoria, South Africa.

2. Cooppan, S. & Skews, B. W. (2013). Vortex Shedding over a Discontinuous Edge. *29th International Symposium on Shock Waves*. University of Wisconsin - Madison, USA.

Contents

Declaration i

Acknowledgements ii

Abstract iii

Published Work iv

Contents v

List of Figures ix

List of Tables xviii

List of Symbols xix

1 Introduction 1

1.1 Motivation 5

1.2 Objectives 6

2 Literature Review 7

2.1 Vortex Cores 8

2.2 Computational Modelling of Shock Wave Diffraction 9

2.3 Research Gap 10

3 Experimental Method **12**

3.1 Introduction 12

3.2 Test Piece Design 12

3.3 Seitz tube 14

3.3.1 Data Acquisition System 17

3.3.2 Pressure and Temperature Sensors 17

3.4 Methodology 17

3.5 Uncertainty in Results 19

3.6 Calibration 23

3.7 Flow Visualization 24

3.8 Conclusions 25

4 Computational Modelling of Vortex Shedding for Impulsive flow over a Discontinuous Edge **26**

4.1 Introduction 26

4.2 Geometry 26

4.3 Mesh 27

4.4 Boundary Conditions 29

4.5 Verification 34

4.5.1 Mesh Independence 34

4.5.2 Shape of Mesh 36

4.5.3 Type of Solver 38

4.5.4 Turbulence Models 39
4.6 Validation 39
4.7 Conclusions 41

5 Vortex Shedding from Impulsive flow over a Discontinuous Edge 42

5.1 Introduction 42
5.2 Mach 1.32 43
5.2.1 Free Vortices 47
5.2.2 Effect of Discontinuity 54
5.2.3 Diffracted Shock Wave 60
5.3 Quantitative Results 62
5.4 Mach 1.42 89
5.4.1 Effect of change in Mach number 92
5.4.2 Effect of Discontinuity 95
5.4.3 Shape of Diffracted Shock 97
5.5 Mach 1.6 99
5.5.1 Effect of Discontinuity 104
5.5.2 Shape of Diffracted Shock 106
5.5.3 Quantitative Results 107
5.6 Conclusions 109

6 Conclusions and Recommendations 110

6.1 Conclusions 110
6.2 Recommendations 111

References **111**

A Apparatus Specifications **114**

List of Figures

1.1 The shock wave diffraction over a 90° edge 1

1.2 Test piece design 4

1.3 Diffracted shock wave over a 10 mm discontinuous edge 4

3.1 Generic Mount 13

3.2 New test piece design 13

3.3 Dimensions of the Seitz tube 15

3.4 Seitz tube diaphragm section 15

3.5 Seitz tube 16

3.6 Control Console 16

3.7 Percentage uncertainty in Mach number 19

3.8 Time of shock diffraction over the diffraction edge for Mach 1.32 (left), 1.42 (centre), and 1.6 (left) 20

3.9 Z-arrangement for the optics set-up 24

4.1 The fluid domain 27

4.2 Sideview of the discontinuous edge 27

4.3 Meshing of the discontinuous edge 28

4.4 Side view of the mesh 28

4.5 Naming of the faces of the fluid domain; Pressure Inlet (left), Pressure Outlet (centre) and Walls (right) 29

4.6 Stationary Shock 29

4.7 Moving reference frame as attached to the shock 31

4.8 Density contours in the Z plane at the wall adjacent to the upstream edge for coarse (left), medium (middle), and fine (right) meshes at a time of ± 54μs after the shock has diffracted over the downstream edge for the 5mm model 35

4.9 Y-velocity contours in the Z plane at the wall adjacent to the upstream edge for coarse (left), medium (middle), and fine (right) meshes at a time of ± 54μs after the shock has diffracted over the downstream edge for the 5mm model 36

4.10 Quadrilateral (left) and Unstructured (right) meshes 36

4.11 Density contours in the Z plane at the wall adjacent to the upstream edge of quadrilateral (left) and unstructured (right) meshes at a time of ± 45μs for the 10mm model 37

4.12 Density iso-surfaces of 1.1kg/m^3 for quadrilateral (left) and unstructured (right) meshes for the 10mm model at a time of ± 45μs 37

4.13 Density contours at M1.42 for an offset edge length of 5mm of implicit (left), and explicit (right) solutions at ± 65μs 38

4.14 Density contours at M1.32 for an offset edge length of 5mm of Euler (left), and Navier-Stokes (right) solutions at ± 54μs 39

4.15 Comparison of experimental image (left) and CFD-density contours (right) at M1.32 of the 5mm offset edge length at time 70μs 40

4.16 Comparison of experimental image (left) and CFD-density contours (right) at M1.42 of the 5mm offset edge length at time 75μs 40

4.17 Comparison of experimental image (left) and CFD-density contours (right) at M1.6 of the 5mm offset edge length at time 58μs 41

5.1 Experimental image of shock diffraction for Mach 1.32 at a time of ± -13μs 43

5.2 Experimental image of shock diffraction for Mach 1.32 at a time of ± -3μs 43

5.3 Experimental image of shock diffraction for Mach 1.32 at a time of ± 10μs 43

5.4 Experimental image of shock diffraction for Mach 1.32 at a time of ± 18μs 44

5.5 Experimental image of shock diffraction for Mach 1.32 at a time of ± 30μs 44

5.6 Experimental image of shock diffraction for Mach 1.32 at a time of ± 39μs 44

5.7 Experimental image of shock diffraction for Mach 1.32 at a time of ± 52μs 44

5.8 Experimental image of shock diffraction for Mach 1.32 at a time of ± 56μs 45

5.9 Experimental image of shock diffraction for Mach 1.32 at a time of ± 66μs 45

5.10 Experimental image of shock diffraction for Mach 1.32 at a time of ± 80μs 45

5.11 Experimental image of shock diffraction for Mach 1.32 at a time of ± 92μs 45

5.12 Experimental image of shock diffraction for Mach 1.32 at a time of ± 100μs 46

5.13 Experimental image of shock diffraction for Mach 1.32 at a time of ± 108μs 46

5.14 Plots of iso-surfaces of density for a time delay of ± 10μs 47

5.15 Plots of vorticity magnitude at a time delay of ± 10μs in the Z plane at the wall adjacent to the upstream edge 48

5.16 Plots of vorticity magnitude at a time delay of ± 55μs in the Z plane at the wall adjacent to the upstream edge 48

5.17 An indication of the direction of flow and the isosurfaces are taken with regards to the entire flow domain 50

5.18 Isosurfaces of density of a value of 0.8 kg/m^3 on the inner surface and 1.1kg/m^3 on the outer surface at a time delay of ± 10μs 50

5.19 Isosurfaces of density of a value of 0.8 kg/m^3 on the inner surface and 1.1kg/m^3 on the outer surface at a time delay of ± 30μs 50

5.20 Isosurfaces of density of a value of 0.8 kg/m^3 on the inner surface and 1.1kg/m^3 on the outer surface at a time delay of ± 56μs 51

5.21 Isosurfaces of density of a value of 0.8 kg/m^3 on the inner surface and 1.1kg/m^3 on the outer surface at a time delay of ± 108μs 51

5.22 Density contours of the 20mm model in the XY plane at 109μs . . . 52

5.23 Slices of density contours at positions 1(left), 2(centre), and 3(right) 53

5.24 Slices of density contours at positions 4(left), 5(centre), and 6(right) 53

5.25 Slices of density contours at positions 7(left), 8(center), and 9(right) 53

5.26 Vorticity magnitude plots at the discontinuity at 10μs 54

5.27 Vorticity magnitude plots at the discontinuity at 27μs 54

5.28 Vorticity magnitude plots at the discontinuity at 65μs 54

5.29 Vorticity magnitude plots at the discontinuity at 109μs 54

5.30 Slices of Y velocity along the X plane (left) and slices of Z velocity along the Y plane (right) 56

5.31 Y velocity contours in the X plane taken along the offset edge length at a time of ± 53μs 57

5.32 Z velocity contours in the Y plane taken along the offset edge length at a time of ± 53μs 59

5.33 Velocity magnitude isosurfaces at a time of ± 10μs at Mach 1.32 . . 61

5.34 Contour of density for the 20mm model at a time of 54μs indicating where the y line was taken in order to extract the data 63

5.35 Variation of vorticity magnitude at the offset edge length along the y axis in the Z plane 65

5.36 Variation of tangential velocity at the offset edge length along the y axis in the Z plane 66

5.37 Variation of radial velocity at the offset edge length along the y axis in the Z plane 67

5.38 Variation of axial velocity at the offset edge length along the y axis in the Z plane 68

5.39 Contour of density in the X plane for the 20mm model at a time of 54μs indicating where the z line was taken in order to extract the data 69

5.40 Variation of vorticity magnitude at the offset edge length along the z axis in the X plane 70

5.41 Variation of vorticity magnitude at the offset edge length along the z axis in the X plane at different time instances 71

5.42 Variation of density at the offset edge length along the z axis in the X plane at different time instances 72

5.43 Contour of density in the Z plane for the 20mm model at a time of 71μs indicating where the y line was taken in order to extract the data 73

5.44 Variation of density at the offset edge length along the y axis in the Z plane at different time instances 74

5.45 Variation of tangential velocity at the offset edge length along the y axis in the Z plane at different time instances 75

5.46 Variation of radial velocity at the offset edge length along the y axis in the Z plane at different time instances 76

5.47 Variation of axial velocity at the offset edge length along the y axis in the Z plane at different time instances 77

5.48 Contour of velocity magnitude at the offset edge length along the y axis in the Z plane 78

5.49 Variation of velocity magnitude at the offset edge length along the y axis in the Z plane at different time instances 79

5.50 Mesh overlaid on contours of velocity magnitude at 54μs (left) and 71μs (right) 80

5.51 Zoomed in view of mesh overlaid on contours of velocity magnitude at 54μs (left) and 71μs (right) 80

5.52 Variation of vorticity magnitude at the offset edge length along the y axis at different slices in the Z plane 82

5.53 Surface plot of density at an angle of 310° for a 20mm model at a time of 54μs 83

5.54 Surface plot of density at an angle of 40° for a 20mm model at a time of 54μs 84

5.55 Surface plot of density at an angle of 120° for a 20mm model at a time of 54μs 85

5.56 Surface plot of vorticity magnitude at an angle of 310° for a 20mm model at a time of 54μs 86

5.57 Surface plot of vorticity magnitude at an angle of 40° for a 20mm model at a time of 54μs 87

5.58 Surface plot of vorticity magnitude at an angle of 120° for a 20mm model at a time of 54μs 88

5.59 Experimental image of shock diffraction for Mach 1.42 at a time of ± -7μs 89

5.60 Experimental image of shock diffraction for Mach 1.42 at a time of ± 2μs 89

5.61 Experimental image of shock diffraction for Mach 1.42 at a time of ± 11μs 89

5.62 Experimental image of shock diffraction for Mach 1.42 at a time of ± 23μs 90

5.63 Experimental image of shock diffraction for Mach 1.42 at a time of ± 37μs 90

5.64 Experimental image of shock diffraction for Mach 1.42 at a time of ± 45μs 90

5.65 Experimental image of shock diffraction for Mach 1.42 at a time of ± 51μs 90

5.66 Experimental image of shock diffraction for Mach 1.42 at a time of ± 67μs 91

5.67 Experimental image of shock diffraction for Mach 1.42 at a time of ± 75μs 91

5.68 Experimental image of shock diffraction for Mach 1.42 at a time of ± 86μs 91

5.69 Experimental image of shock diffraction for Mach 1.42 at a time of ± 94μs 91

5.70 Experimental image of shock diffraction for Mach 1.42 at a time of ± 101μs 92

5.71 Experimental image of shock diffraction for Mach 1.42 at a time of ± 111μs 92

5.72 Isosurfaces of density of a value of 0.8 kg/m^3 on the inner surface and 1.1kg/m^3 on the outer surface for Mach 1.42 at a time delay of ± 8μs 93

5.73 Isosurfaces of density of a value of 0.8 kg/m^3 on the inner surface and 1.1kg/m^3 on the outer surface for Mach 1.42 at a time delay of ± 34μs 93

5.74 Isosurfaces of density for Mach 1.42 a value of 0.8 kg/m^3 on the inner surface and 1.1kg/m^3 on the outer surface for Mach 1.42 at a time delay of ± 62μs 94

5.75 Isosurfaces of density of a value of 0.8 kg/m^3 on the inner surface and 1.1kg/m^3 on the outer surface for Mach 1.42 at a time delay of ± 106μs 94

5.76 Isosurfaces of density for Mach 1.42 of a value of 0.8 kg/m^3 on the inner surface and 1.1kg/m^3 on the outer surface at a time delay of ± 44μs 95

5.77 Plots of vorticity for Mach 1.42 at a time delay of ± 8μs 95

5.78 Plots of vorticity for Mach 1.42 at a time delay of ± 34μs 96

5.79 Plots of vorticity for Mach 1.42 at a time delay of ± 62μs 96

5.80 Plots of vorticity for Mach 1.42 at a time delay of ± 106μs 96

5.81 Velocity magnitude isosurfaces for Mach 1.42 at a time of ± 10μs at Mach 1.42 97

5.82 Experimental image of shock diffraction for Mach 1.6 at a time of ± -6μs 99

5.83 Experimental image of shock diffraction for Mach 1.6 at a time of ± 5μs 99

5.84 Experimental image of shock diffraction for Mach 1.6 at a time of ± 16μs 99

5.85 Experimental image of shock diffraction for Mach 1.6 at a time of ± 23μs 100

5.86 Experimental image of shock diffraction for Mach 1.6 at a time of ± 28μs 100

5.87 Experimental image of shock diffraction for Mach 1.6 at a time of ± 39μs 100

5.88 Experimental image of shock diffraction for Mach 1.6 at a time of ± 47μs 100

5.89 Experimental image of shock diffraction for Mach 1.6 at a time of ± 55μs 101

5.90 Experimental image of shock diffraction for Mach 1.6 at a time of ± 73μs 101

5.91 Experimental image of shock diffraction for Mach 1.6 at a time of ± 78μs 101

5.92 Experimental image of shock diffraction for Mach 1.6 at a time of ± 89μs 101

5.93 Isosurfaces of density for Mach 1.6 of a value of 0.8 kg/m^3 on the inner surface and 1.1kg/m^3 on the outer surface at a time delay of ± 13μs 103

5.94 Isosurfaces of density for Mach 1.6 of a value of 0.8 kg/m^3 on the inner surface and 1.1kg/m^3 on the outer surface at a time delay of ± 29μs 103

5.95 Isosurfaces of density for Mach 1.6 of a value of 0.8 kg/m^3 on the inner surface and 1.1kg/m^3 on the outer surface at a time delay of ± 74μs 103

5.96 Isosurfaces of density for Mach 1.6 of a value of 0.8 kg/m^3 on the inner surface and 1.1kg/m^3 on the outer surface at a time delay of ± 88μs 103

5.97 Plots of vorticity for Mach 1.6 at a time delay of ± 13μs 105

5.98 Plots of vorticity for Mach 1.6 at a time delay of ± 29μs 105

5.99 Plots of vorticity for Mach 1.6 at a time delay of ± 74μs 105

5.100Plots of vorticity for Mach 1.6 at a time delay of ± 88μs 105

5.101Velocity magnitude isosurfaces for Mach 1.6 at a time of ± 10μs . . 107

5.102Variation of vorticity magnitude along the y line for in the Z plane for the different Mach numbers 108

List of Tables

3.1 Diaphragm pieces used (measured in μm) 15

3.2 Summation of trigger delays used 19

3.3 Experimentation data for the 20mm offset edge length at Mach 1.6 . 21

3.4 Processed experimental data for the 20mm offset edge length at Mach 1.6 22

4.1 The number of elements used for the different offset edge lengths . . 29

4.2 Boundary conditions for the higher Mach numbers 32

4.3 Fluent Settings 33

4.4 Number of cells per model 34

4.5 Timesteps for the different mesh sizes 35

4.6 Time after the shock has diffracted (μs) for each Mach Number . . . 41

5.1 Time Delays 48

5.2 Non-dimensionalised time 49

A.1 Seitz Shock tube specifications 114

A.2 Compression Chamber specifications 114

A.3 Electric Motor specifications 114

A.4 Optics specifications 114

List of Symbols

M_s	Shock Mach number
M_1	Downstream Mach number
M_2	Upstream Mach number
M_{abs}	Downstream Mach number in the moving reference frame
t	Time
P_1	Downstream static Pressure
P_2	Upstream static Pressure
P_{01}	Downstream stagnation Pressure
P_{02}	Upstream stagnation Pressure
R	Gas constant for air
T_1	Downstream static Temperature
T_2	Upstream static Temperature
T_{01}	Downstream stagnation Temperature
T_{02}	Upstream stagnation Temperature
V_s	Shock Velocity
V_1	Downstream Velocity
V_2	Upstream Velocity
V_{abs}	Downstream Velocity in the moving reference frame

γ	Ratio of specific heats of air
C_p	Specific heat capacity of air

1 Introduction

Over the last century there has been extensive research into two dimensional vortices. The developments of technology in computational fluid dynamics (CFD) and high speed cameras has allowed for the study of vortex dynamics as a result of complex shapes as well as in three dimensions. The work done by Sun & Takayama (2002) has proved that detailed and accurate models can be created to simulate shock wave diffraction in two dimensions. It remains to be seen whether models to the same degree of accuracy can be used in three dimensions. The common practice is therefore a pictorial comparison of the numeric solutions to the experimental images.

A fundamental study of shock waves has been the shock wave diffraction over a 90° edge. The study was addressed extensively by Skews (1966), in which a number of key features were identified; the free vortex, shear layer, viscous vortex, expansion wave, and diffracted shock wave as can be seen in figure 1.1.

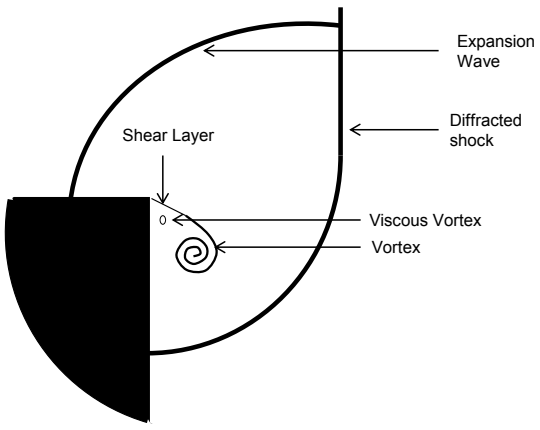

Figure 1.1: The shock wave diffraction over a 90° edge

Skews (1966) also investigated shock diffraction over convex and concave corners,

and thereafter showed that the process is pseudo-stationary, in other words self-similar. A feature that aids to the formation of the free vortex is the shear layer. A shear layer is a region where high velocity exists on the upper surface and interacts with the effectively stationary gas below it. Its existence is brought about by the inability of the shock accelerated gas to negotiate the corner. Skews states that the width of the shear layer increases as the distance from the corner increases. The shear layer becomes curved at the point furthest away from the corner. The low pressure area due to the vortex formation results in the curvature of the shear layer.

Skews (1966) identified the presence of secondary shock waves at high Mach numbers. The topic is addressed in detail by the work of Sun & Takayama (1996). The formation of a secondary shock at a sharp convex corner is due to the local supersonic flow. The subsonic flow behind the incident shock wave is accelerated to supersonic flow through expansion waves. The Mach number of the incident shock wave which is capable of producing a secondary shock wave is approximately 1.35. Sun & Takayama (1996) found that the formation of the secondary shock wave is independent of the configuration of the corner, on the condition that there is enough space for the formation of a free vortex.

The research completed by Skews (1966), and by Sun & Takayama (1996) dealt with two dimensional flows. In more recent times there have been studies with regards to three dimensional flows. Reeves (2010) investigated unsteady three dimensional compressible vortex flows at the University of Witwatersrand. The vortices were generated by passing a shock (of various strengths) over diffraction edges of different shapes. The shapes included a V and inverted V models as well as parabolic and inverted parabolic models.

The shock wave diffraction of the parabolic models was consistent with the two-dimensional case. The vortex formed expanded with time as it propagated downstream. Secondary shock waves were formed in the vortex in the region near the viewing window. The windows decelerated and guided the supersonic flow above the shear layer around the vortex. The vortex itself bent as it approached the window. The window acts as a solid boundary. The vortex core/axis is stretched in the region near the solid boundary. It is forced to bend so as to terminate at the boundary at 90°.

The V models created larger angles (45°) with the window in comparison to the parabolic models (25°). The vortex formed assumed a shape very similar to a conical envelope. However this shape was disrupted once the incident shock fully diffracted

over the edge, and when the vortices on either side of the V meet.

The vorticity was analysed through a number of plots: tangential, radial, upstream velocity and normalized pressure were also plotted against distance along the vortex. Normalized pressure is a ratio of the pressure at a particular point to the atmospheric pressure. The results for all the models were similar. The tangential velocity mirrored a Rankine vortex; the tangential velocity was proportional to the distance away from the core (near the core of the vortex). The radial velocity was randomly scattered, and the upstream velocity increased on the inner part of the bend of the vortex. The normalized pressure was 0.3 at the core. The pressure plots were taken at two planes. The first plane was a portion of the vortex where the core was straight and undisturbed by the distortions at the wall or centre of the flow domain. The second plane was through the vortex as it bent in the region near the solid boundary.

The bend in the vortex is a region of high vorticity in comparison to the rest of the vortex. Reeves (2010) suggests that in the portion of the bend, the vortex contracts. The contraction of the vortex means a maximum of the vorticity vector occurs in this region.

The vorticity production was normalized by RT_0. There was evidence to suggest that the vorticity production was independent of the diffracting edge profile, since the plot of normalized pressure against time only varied with Mach number. The effect of increasing the Mach number was for the shear layer to lengthen and for the vortex to take on an elliptical profile. As a result of the experimentation, two other conclusions were reached: one that the circulation is proportional to time and secondly that the rate of circulation is proportional to the shock strength.

A study was completed at undergraduate level with regards to three dimensional vortices. An extension of this study both computationally and experimentally will form the foundation of the current study. Vortex shedding over a discontinuous edge was investigated by the author (Cooppan (2011)). This study was carried out by designing test pieces which formed a discontinuous edge that varied in 5 mm increments. Three models were made; 5 mm, 10 mm, and 15 mm. Thereafter a shock was passed over the test pieces and the resulting flow was investigated.

Figure 1.3 shows the presence of a viscous vortex, shear layer, and a free vortex. These results correlate with the work done by Skews (1966), Sun & Takayama (1996), and Reeves (2010). However the key difference is in the shape of the diffracted shock wave.

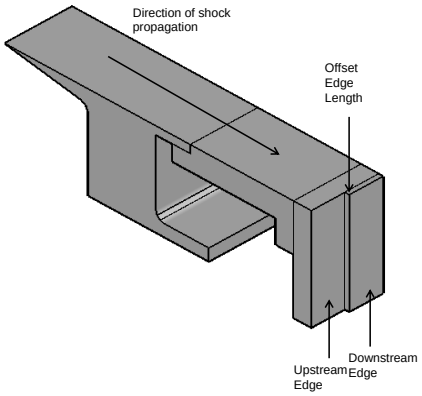

Figure 1.2: Test piece design

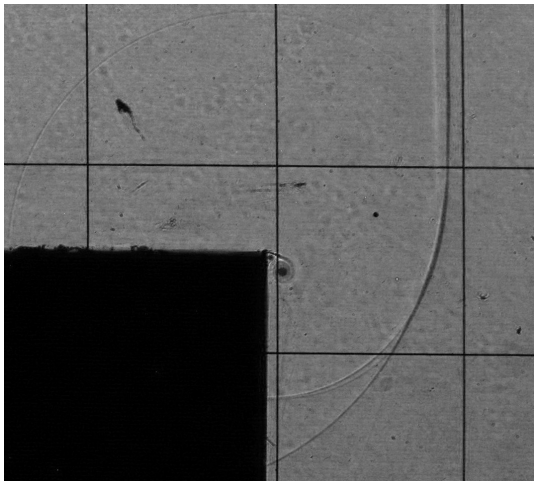

Figure 1.3: Diffracted shock wave over a 10 mm discontinuous edge

The shape of the diffracted edge, tends to suggest that the shock wave diffracted at three points; the downstream edge, the upstream edge and the offset edge length.

A number of conclusions were reached regarding an increase in the offset edge length:

- The distance between the various points of the diffracted shock wave, as can be seen in figure 1.3, increased.
- The free vortex weakens quicker.
- The direction of free vortex core shifts towards the right.

1.1 Motivation

As previously mentioned, there has been extensive research into the field of two dimensional vortices. In contrast the study of three dimensional vortices has been fairly limited. This is due to a number of reasons, primarily; the complexity of the flow field and the lack of computer power too accurately and efficiency model three dimensional flows.

The study completed at undergraduate level highlighted a number of areas which can be investigated further. In the first case, the vortex shed over a discontinuous edge, the shape of the shock profile suggests that the shock wave diffracted at three different edges. The test piece used in the study was such that one of the vortices was blocked from sight. The expected outcome, since there are two 90° edges, is that there are two free vortices which interact with one another. In order to gain a better understanding of the flow field, one of the aims of the current study will be to design test pieces which will enable both vortices to be seen. Numeric simulations will have to be set up and be validated by the findings in the experimental images. These simulations will have to be accurate and detailed analysis will have to be performed.

Vortices affect aircraft design which has significantly improved throughout the years. The role vortices play varies depending on the type of aircraft and its uses. In supersonic aircraft, vortices are used to generate lift [Elsayed et al. (2011)]. In other aircraft, wingtip vortices can potentially be a major component of wake turbulence [Gerz et al. (1997)]. Flapping wings generate lift through the Kramer effect [Daya (2009)]. The Kramer effect is brought about by the rotation of a ring vortex about the spanwise axis. The net result is that the vortex ring increases, which in turn produces additional circulation, and ultimately leads to an increase in lift.

The understanding of vortices, particularly in three dimensions, will aid a number of fields. However in many if not all of these cases, vortices do not exit as singular entities. There will be to some extent an interaction between the vortices. This idea is a key emphasis of this study.

1.2 Objectives

- Investigate vortex shedding as a result of:
  - A discontinuous edge
- Investigation for the discontinuous edge case is comprised of two parts; computational and experimental.
- Design test pieces to study the effect of a discontinuous edge on vortex shedding. The discontinuous edge is to be varied geometrically; starting at 5 mm and ending at 20 mm.
- Create accurate and detailed computational models. Models must be created for:
  - A discontinuous edge of 5 mm, 10 mm, and 20 mm.
- Evaluate the experimental and computational solutions via a pictorial comparison, as well as a comparison to previous work done; including 4th year research projects and the work done by Reeves (2010).

2 Literature Review

Chapter 1 outlines the specifics that the current study deals with. The purpose of this literature review is to give the reader an overview of vortices, vortex dynamics and discuss other topics which contribute to this study.

Vortices appear in numerous fields; from hurricanes to water draining. As such there are multiple definitions of what vortices are, without one clear standard definition. One of the simpler explanations is that vortices are flows in which streamlines form closed loops. Alternatively, Green (1995) describes a vortex as a region of concentrated vorticity, where vorticity is a measure of how rapidly fluid rotates about itself.

Vortex flows have the potential to become complex, such that it can no longer be mathematically described. Despite this, vortices are still governed by physical laws; namely Helmholtz's laws for inviscid compressible flows:

- Circulation remains constant within a fluid along its length
- A potential region within an inviscid fluid will remain as a potential
- If a fluid does not initially contain vorticity, it will remain free of vorticity

The first law states that the circulation around a vortex is constant. This statement remains true even if the original vortex were split into smaller vortices. The sum of the circulations of the individual components will be equal to the original circulation. As the cross-sectional area of the vortex approaches zero, the vorticity about the given area will approach infinity. It can therefore be observed that a vortex cannot terminate in a fluid; otherwise circulation cannot be achieved. Vortices can either form loops entirely within a fluid or terminate at a solid boundary or a fluid-fluid interface.

2.1 Vortex Cores

Vortex cores have the potential to provide detail about the entire vortex flow. It is therefore an important analytical tool.

The work that has been done on vortex cores is specific with regards to how the vortex has been formed. Lee & Bershader (1994) investigated the vortex core of vortices formed from the trailing edge of aircraft. Vortices behind an aircraft has been broken up into stages:

- Roll-up
- Equilibrium
- Decay

The equilibrium stage is split into four stages:

- Core
- Logarithmic
- Transition
- Irrotational

The core undergoes solid body rotation, where the circulation is proportional to the square of the distance from the centre. In the logarithmic region, as the name suggests, the circulation is proportional to the logarithm of the distance from the centre. This region is where the tangential velocity reaches a maximum. The transition region has no correlation to circulation. The irrotational section has constant circulation.

These results take into account viscous effects. Therefore a variation in circulation across the vortex is present; whereas Helmholtz's Laws states that the circulation is constant.

The work done by Hall (1965) provides a more general description of vortex cores. Hall (1965) states that three-dimensional vortex cores are vigorous and highly responsive. Responsiveness is a measure of how much the vortex core changes as a

result of outside influences. These features allow for the interaction between different components of the core as a result of the surrounding flow. A combination of these factors could result in large circumferential and axial velocities.

The change in axial velocity is a measure of how responsive the vortex core is i.e. there will be a change in the vortex structure along the axis.

The effects of compressibility are interesting. Firstly there is a marked change in responsiveness. The second effect is a drop in the density at the core. The density approaches zero.

2.2 Computational Modelling of Shock Wave Diffraction

Shock wave diffraction has been modelled numerically on a number of occasions. The model geometry, boundary conditions, and the set-up of the computational model can be altered. The prime challenge with computational modelling is refining the solution so that a number of flow features can be identified.

Many have used structured quadrilateral (quads) meshes, since quads provide higher resolution then triangular meshes. This is due to the fact that quads have an additional node in comparison to triangles, in two dimensions. In three dimensions the quad takes the form of a cube and the triangle takes the form of a pyramid. As such the cube has twice as many nodes as the pyramid. These are important factors in order to get a high resolution for the solution. The type of mesh chosen is influenced by the geometry. More complex geometry is difficult to model with quads, since the mesh becomes distorted and the cells become skew. This can be compensated for by using a small cell size. However this requires more time and more computational power. Therefore a compromise needs to be reached between the time taken and the level of resolution of the solution.

The current study involves a three dimensional moving shock. In computational terms, this set-up is the most expensive; with regards to the time taken and power needed.

Ripley et al. (2006) analysed strong and weak shocks diffracting over a 90° edge; Mach 2.4 and 1.3. The mesh which was used was unstructured triangular and it had the ability to capture the macroscopic flow features. However the fine details could only be seen with a mesh refinement scheme.

Sun & Takayama (2003) found that the shear layer, formed as a result of shock wave diffraction over a 90° edge, broke down into many small vortices for a fine mesh. These results have been proven for both Euler and Navier-Stokes solutions. A similar type of phenomena has been seen in simulations of Mach reflection over a wedge that contains a shear layer. The suggested cause is the instability in the shear layer causing the Kelvin-Helmholtz's instability to develop resulting in small vortices. The work done by Ripley et al. (2006) and Sun & Takayama (2003) is on two dimensional flows.

The work done on three dimensional modelling by Reeves (2010) suggests that meshes are coarse in comparison to two dimensional modelling. At the present moment three dimensional models are unlikely to match the accuracy of two dimensional models. However a good correlation can be obtained with regards to experimental images (Reeves (2010)). The nature of computer modelling is such that no two people can produce the exact same solution.

2.3 Research Gap

At the end of chapter 1, a list of objectives was outlined. The current section will provide insight into how the current study contributes to the field of flow research.

1. The field of vortices is large. The current study is specifically focused on vortices produced as a result of shock wave diffraction. Within this field there have been a number of studies. The studies concerned with shock wave diffraction over a 90° edge are a smaller field. Extensive experimental data was found by Skews (1966), whereas many computational cases have been ran as shown in the poster presentation at ISSW 18 [Takayama & Inoue (1991)]. These findings were on two dimensional flows. Reeves (2010) investigated three dimensional vortices as a result of different shapes, as mentioned in chapter 1. The current study involves three dimensional vortices formed as a result of new set of geometries;
    - A discontinuous edge
2. The investigation of vortex formation from a discontinuous edge is an extension of the two dimensional problem. The interest here lies in the interaction of the vortices and the respective topology.
3. It follows from the first point that there have been few studies done with regards to three dimensional modelling of vortices produced from shock wave

diffraction. For the above mentioned investigations; the corresponding computational models will be set-up. These models will contribute to a field which has relatively little data.

3 Experimental Method

3.1 Introduction

The Seitz tube, located in the North West Engineering Laboratory at the University of the Witwatersrand, is used to generate a shock wave in order to investigate the flow over a discontinuous edge. Shock waves of three different strengths were generated; Mach 1.32, 1.42 and 1.6. The only data that can be captured were images of the shock diffracting over the test piece. Therefore certain criteria had to be met in order to insure that the images produced are of good quality:

- A consistent Mach number was produced
- Have the correct optics set-up
- The test piece is designed such that the flow can be visualised and that the force of the shock can be withstood
- The surface of the model must be smooth

3.2 Test Piece Design

An initial design was undertaken at undergraduate level. However not all the flow features could be seen, as outlined in Chapter 1.

A generic mount is a piece of equipment used in the Seitz tube in order to cut the incident shock wave. This is done to insure that the shock wave is as uniform as possible as it passes over the test piece, and diffracts. The generic mount has been used in previous studies, where the test piece is bolted onto the generic mount from underneath. This factor as well as the dimensions had to be taken into account. In addition to blocking the vortex shed of the upstream edge, the initial design was long

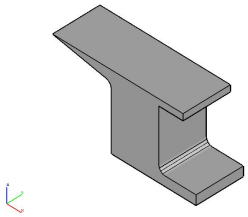

Figure 3.1: Generic Mount

and heavy. The material used was steel which contributes to the weight, making the model (combination of test piece and generic mount) difficult to install in the Seitz tube.

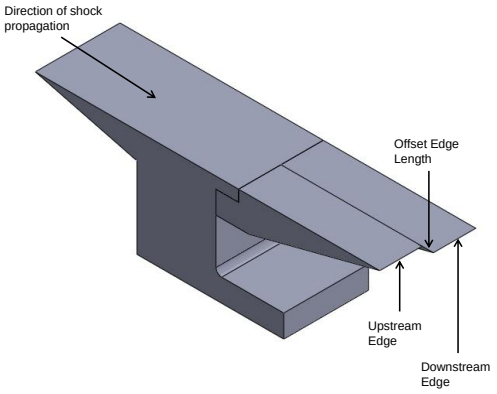

Figure 3.2: New test piece design

The new design is comprised of two pieces. The longer piece contains holes on the sides; whereas the shorter piece contains threaded holes to allow the pieces to be bolted to one another. Additionally plugs were used to insure the surface was uniform. The material used was aluminium, which made the model significantly lighter. Finally the angle between the surface of the model and the incident shock, as viewed from the side, was reduced from 90° to 14.5°. Skews (1966) states that as the angle is reduced from 90° to effectively zero, there is little effect on the flow features.

The different offset edge lengths were created by varying the length of the shorter piece. The end result being that three lengths were created; 5mm, 10mm, and 20mm. These ranges of values were chosen to firstly show the strong interaction between the vortices shed of the upstream and downstream edges. Thereafter to see the diminishing interaction; up until the vortices behaved independently.

In order to produce a flush surface, any portion of the threaded holes (the points at which the test piece was bolted to the generic mount) that was exposed needed to be covered. Candle wax was the chosen medium since it could be easily moulded in a liquid state and hardened quickly. The sides of the test pieces were covered with layers of masking tape. This was done to prevent:

- Leakage along the sides
- The models from scratching the glass

The models withstood the force generated by Mach 1.32 and 1.42. However the force generated at Mach 1.6 loosened the test piece from the generic mount. In additional some of the tapes on the sides of the test piece shifted. After having a closer look; the threads on the generic mount were damaged. To overcome this problem, the sizes of the bolts were changed from M5 to M6.

3.3 Seitz tube

The Seitz tube has the potential to produce a Mach number of up to 1.8 into atmospheric air. However it shows particular consistency with certain Mach numbers; in terms of the Mach number produced and the desired Mach number. Reeves (2010) used Mach numbers 1.32, 1.42, and 1.65. These range of values cover the weak shock diffraction spectrum (Ripley et al. (2006)). The current study was repeated at the same lower Mach numbers, but a Mach number of 1.6 was found to be more consistent.

The Seitz tube has its own specialized software and is therefore an automated system. However it can be manually operated in the cases of emergency and for troubleshooting.

The Seitz tube is comprised of a compression, intermediate and expansion chambers as well as an optical flow visualization system. The compression and intermediate chambers are referred to as the driver sections. A double-diaphragm design is utilized.

A detailed description of the automated process is given below. Once the Seitz tube is in operation; the hydraulic motor automatically closes the driver sections and clamps the diaphragm. The diaphragm is made from polyester films. The thickness is dependent on the Mach number.

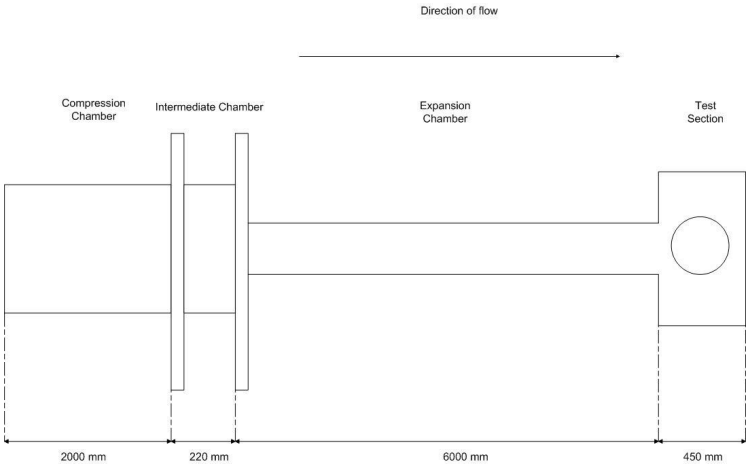

Figure 3.3: Dimensions of the Seitz tube

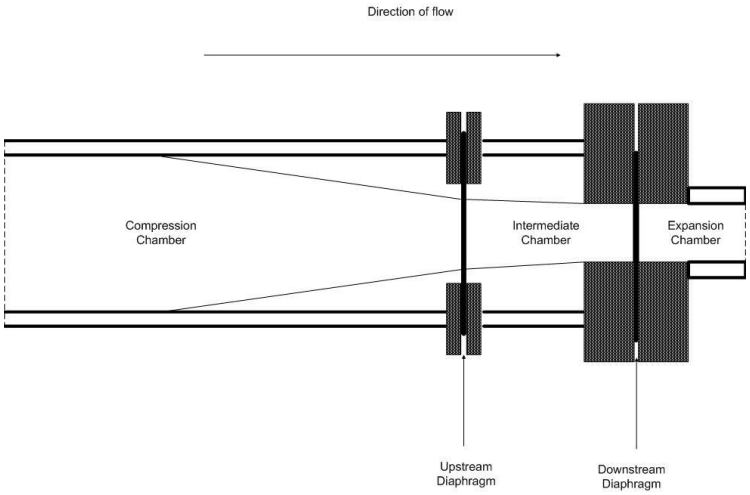

Figure 3.4: Seitz tube diaphragm section

Table 3.1: Diaphragm pieces used (measured in μm)

Mach Number	**Downstream Diaphragm**	**Upstream Diaphragm**
1.32	23	56
1.42	2x23	56
1.6	23,56	2x100

Once the air pressure in the driver sections has reached its required value, corresponding to the Mach number specified by the user, the chambers are closed. Both chambers are pressurized simultaneously. When the intermediate chamber has reached its required value, a solenoid valve separates it from the compression chamber. In the meanwhile, the compression chamber continues to be pressurized until there is a significant pressure difference.

The diaphragm closest to the compression chamber bursts first. This is due to the

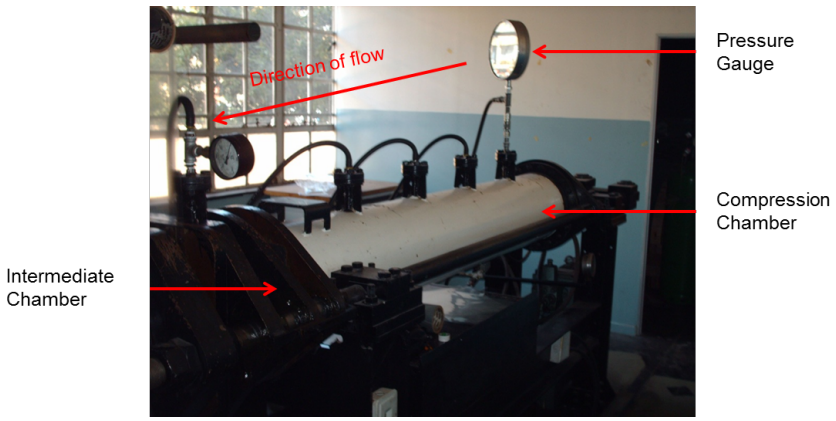

Figure 3.5: Seitz tube

fact that the intermediate chamber vents air into the atmosphere. The pressure decreases causing the upstream diaphragm to burst, then the downstream diaphragm. The net result is the production of a shock wave.

The pressure in the compression chamber decreases rapidly as the air is vented into the atmosphere from the Seitz tube. At this point the driver sections maybe opened. As a safety requirement, once the pressure gauges have reached zero, the compression chamber can then be opened.

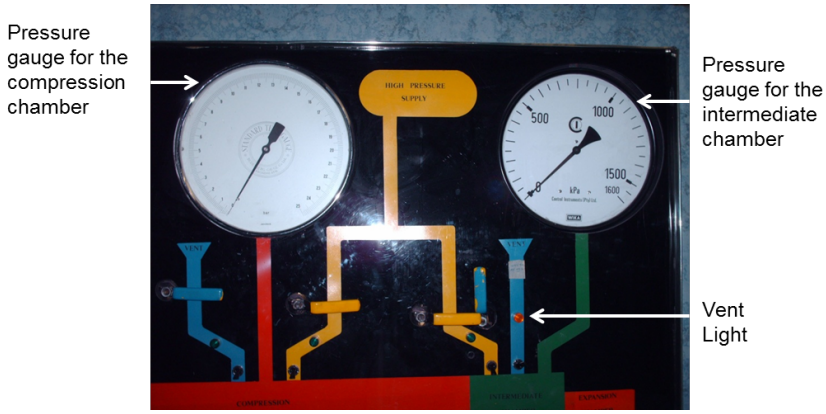

Figure 3.6: Control Console

Manual operation is controlled by electric toggle switches. These switches control the solenoid valves. The compression chamber can be opened or closed by using the hydraulic motor starter switch in the case of an emergency.

3.3.1 Data Acquisition System

The software used to operate the Seitz tube is controlled with data acquisition cards. The temperature and pressure values are obtained using eight 12-bit analogue input ports with a sample rate of five million per second for each channel. The digital triggering capabilities are controlled by a PCI-6224 data acquisition card with forty eight inputs/outputs. It triggers various operations of the Seitz tube, and is largely responsible for the automated process.

3.3.2 Pressure and Temperature Sensors

The temperature and pressure sensors have resolutions of 0.25°C and 0.4mbar respectively. The high pressure transducers measure the pressure in the driver sections, and can withstand rapid changes in pressure, from 0 to 20bar. The maximum operating pressure within the Seitz tube is 15bar.

However, inside the shock tube, the pressures are measured using fast response piezoelectric pressure transducers (PCB). The PCBs pass signals which are processed by the data acquisition software. This allows the speed of the shockwave and the timing of the light source to be determined.

3.4 Methodology

The operation of the Seitz tube needs to be shown to the user by either a technician or a postgraduate, who is familiar with the Seitz tube. Thereafter the user needs to operate the Seitz tube while under supervision. This includes the operation of the compressor (mentioned below). The user can then operate the Seitz tube, once the supervisor is happy with the performance.

The pressure used in the Seitz tube is drawn from a storage vessel. The Seitz tube can be operated if the pressure in the storage vessel is between 0.8 and 1.5MPa. Mach numbers of 1.42 and 1.6 require a minimum of 1.0MPa. That needs to be taken into account while testing. Before a day of testing begins the compressor (used to build up pressure in the storage vessel) needs to be switched on and off as appropriate.

To ensure testing is done correctly, forms are filled out. One at the start of the day

(MSAST-04) and an alternate one after each test (MSAST-03). The latter records information such as temperature and the actual Mach number produced, which are important parameters when it comes to analysis.

The testing procedure is outlined below:

- Before testing can officially begin all the equipment has to be switched on, including the pressure supply, electrical supply, and computer. The coverings need to be carefully removed from the optics. Fill out the MSAST-04 form.
- The test section needs to be open and the model needs to be connected. Thereafter remove the used diaphragms (if there are any) and clean out the venting tube, compression and intermediate chambers using the high pressure hose. Wear hearing protection while doing this.
- Attach the required upstream and downstream diaphragms. As added precautions make sure the model is correctly fitted and secure. Close and secure the test section, the last two points are the most important in operating the Seitz tube, since there is a serious risk of injury.
- Close the door and initialise the computer sequence. Ensure that the correct Mach number and trigger delay are set. Wear hearing protection.
- Switch on the camera, and continue the computer sequence until it is finished. Switch off all the lights, including the computer screen. Once this is done, open the shutter of the camera. The computer sequence initialises the closing off the compression chamber and what pressure it is required to be filled to. Once these pressures have been reached, there is a period of calm before the bursting of the diaphragms and the resulting propagation of the shock. The light source is triggered by a transducer, where the trigger delay has to be input into the computer sequence. The shutter of the camera must be closed once the shock has passed.
- Switch on the lights and make sure the compression pressure gauge drops to zero before giving the command to open. Finally complete the MSAST-03 form.

To perform a new test, repeat the above procedure.

The single-shot camera as the name suggests takes one image of a high resolution. Therefore a number of tests are performed in order to evaluate the flow over time.

The trigger delay plays an important part as it corresponds to a particular instant in time. Incremental trigger delays of 10μs were used.

Table 3.2: Summation of trigger delays used

Mach Number	Starting Trigger Delay(μs)	Ending Trigger Delay(μs)
1.32	1835	1955
1.42	1715	1835
1.6	1530	1630

The initial trigger delay is found by performing preliminary tests until a satisfactory starting point is reached. A similar approach is taken for the other two Mach numbers.

3.5 Uncertainty in Results

Table 3.3 shows an example of the experimental data obtained. During testing the temperature varied. Considering testing was done over a span of two months, there was a wide range of temperatures. However the effect of temperature on the operation of the Seitz tube was minimal. The Seitz tube has been in operation since 1990, and problems occur particularly with air leakage and the light source not triggering. Table 3.3 highlights the point made earlier that a number of tests were performed to find an appropriate starting trigger delay.

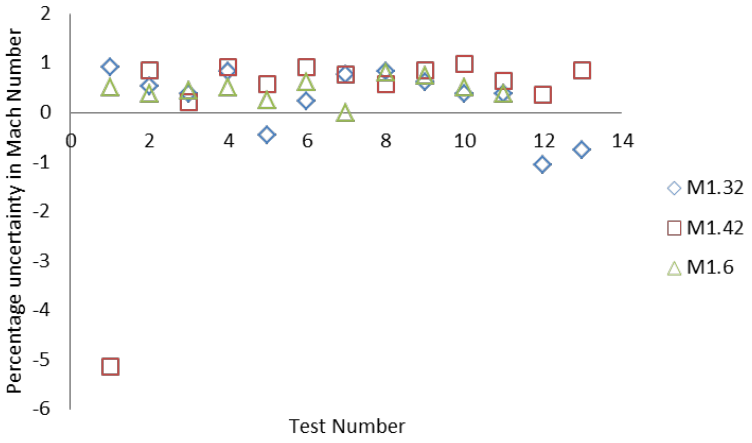

Figure 3.7: Percentage uncertainty in Mach number

The percentage uncertainty is calculated as the difference between the desired and actual Mach number, over the desired Mach number. From figure 3.7 all the Mach numbers show a low uncertainty; in the range between -1% and 1%. The largest

variation occurs for the lowest Mach number, 1.32. Apart from one relatively large uncertainty, M1.42 has the smallest spread of data. It can be concluded that there is a high level of consistency for the Mach numbers chosen.

A number of images are obtained for each offset edge length as well as the various Mach numbers. In order to evaluate the effect of the offset edge length, the different lengths need to be compared to each other. Therefore the time after the shock has diffracted over the longer part of the test piece (chosen as an arbitrary point) was calculated:

- The distance between the diffraction edge and the straight portion of the diffracted shock wave was measured. It was measured on the experimental images.
- A ratio was formed between the offset edge length on the image and the actual offset edge length. This ratio was applied to the distance measured above, in order to get the actual distance between the diffraction edge and diffracted shock wave.
- The velocity was calculated using the measured temperature and actual Mach number, according to: $V = M\sqrt{(\gamma - 1)(C_p)(T)}$
- Finally the time was calculated using the definition of velocity, the distance covered over a period of time.

The calculation of time is also used as a parameter to compare the experimental results to the CFD models.

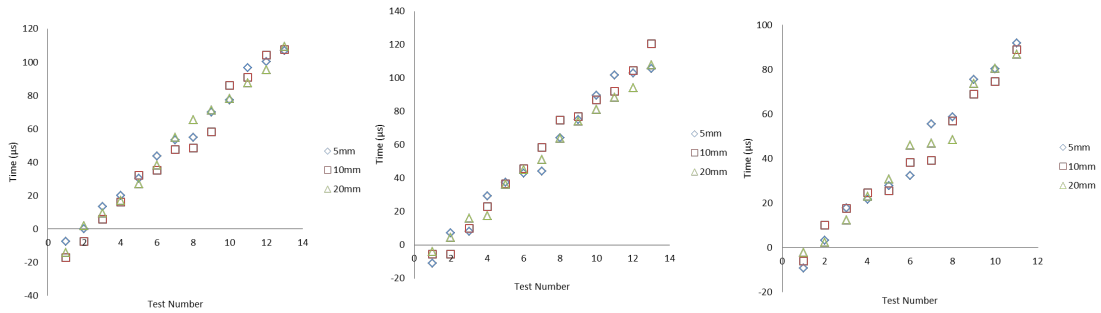

Figure 3.8: Time of shock diffraction over the diffraction edge for Mach 1.32 (left), 1.42 (centre), and 1.6 (left)

Table 3.3: Experimentation data for the 20mm offset edge length at Mach 1.6

Test Number	**Time**	**Required Mach Number**	**Trigger Delay (μs)**	**Camera Image Number**	**Temperature (°C)**	**Actual Mach Number**	**Success**	**Comment**
1	09:43	1.6	1440	9554	12.45	1.607	Yes	
2	09:59	1.6	1470	9555	12.26	-0.003	No	Light source failed
3	10:07	1.6	1470	9556	12.44	1.607	No	Camera was full
4	10:22	1.6	1470	9556	13.01	4	No	Test Failed
5	10:32	1.6	1470	9557	13.19	1.609	Yes	
6	10:42	1.6	1490	9558	12.98	1.61	Yes	
7	10:51	1.6	1540	9559	13.17	-	No	Leakage is System
8	11:00	1.6	1540	9559	12.91	1.606	Yes	
9	11:10	1.6	1550	9560	12.96	1.607	Yes	
10	11:21	1.6	1560	9561	13.07	1.608	Yes	
11	11:31	1.6	1570	9562	13.15	1.604	Yes	
12	11:41	1.6	1580	9563	13.51	1.605	No	Did not take photo
13	11:49	1.6	1580	9563	13.68	1.61	Yes	
14	12:02	1.6	1590	9564	13.33	1.6	Yes	
15	14:10	1.6	1600	9565	13.57	1.613	Yes	
16	14:20	1.6	1610	9566	13.6	-0.003	No	Same as test 2
17	14:28	1.6	1610	9567	13.46	1.612	Yes	
18	14:36	1.6	1620	9568	14.03	1.608	Yes	

Table 3.4: Processed experimental data for the 20mm offset edge length at Mach 1.6

Test Number	**Distance from most forward diffraction edge (mm)**	**Actual Distance (mm)**	**Temperature (K)**	**Actual Mach Number**	**Velocity (m/s)**	**Time (μs)**
1	-1.5	-1.25	285.63	1.608	545.15	-2.29
2	1.5	1.25	286.06	1.606	542.85	2.30
3	8.0	6.67	286.11	1.607	542.90	12.28
4	15.0	12.50	286.22	1.608	543.00	23.02
5	20.0	16.67	286.30	1.604	543.08	30.69
6	30.0	25.00	286.83	1.610	543.58	45.99
7	30.5	25.42	286.48	1.600	543.25	46.79
8	31.5	26.25	286.72	1.613	543.47	48.30
9	48.0	40.00	286.61	1.612	543.37	73.61
10	52.5	43.75	287.16	1.608	543.89	80.44
11	56.5	47.08	285.80	1.606	542.60	86.77

Ideally the comparison of the different offset edge lengths would all be at as similar time intervals as possible. Figure 3.8 shows all three Mach numbers have a linear progression. The lower Mach numbers show a good correlation between the offset edge lengths. The data at Mach 1.6 is more spread. There were some difficulties with regards to the test pieces at this Mach number. It is worth noting that the largest spread of data occurs in the middle portion.

The changing of the bolts from M5 to M6 occurred halfway through the testing of the 10mm length. At this point the testing of the 20mm length had already been completed. During the testing of the 5mm length, there was slipping and tearing of the masking tape. Therefore there was leakage in the system, not enough to distort the flow, but enough to be an inconvenience. These factors could have contributed to in the discrepancy between the times.

3.6 Calibration

In order for the Seitz tube to produce the requested Mach number, the Mach number needs to be calibrated. In this sense calibration is the procedure of matching the diaphragm thickness to the Mach number. Therefore the correct combination between upstream and downstream diaphragms needs to be found. The procedure for calibration:

- The upstream and downstream diaphragms need to be attached.
- A similar procedure to testing is followed. The test section needs to be secured (No model needs to be connected). The computer sequence is started and the calibration option is chosen.
- This procedure differs from testing in that the pressure fills the compression and intermediate chambers until the diaphragms burst naturally.
- Calibration needs to be done at least five times. For a given combination, there will be a range of pressures and hence Mach numbers.

Table 3.1 shows which combinations of diaphragms were used for the corresponding Mach number.

3.7 Flow Visualization

The optics set-up used is a typical Z-arrangement, since it is the most common practice and used to investigate a variety of phenomena.

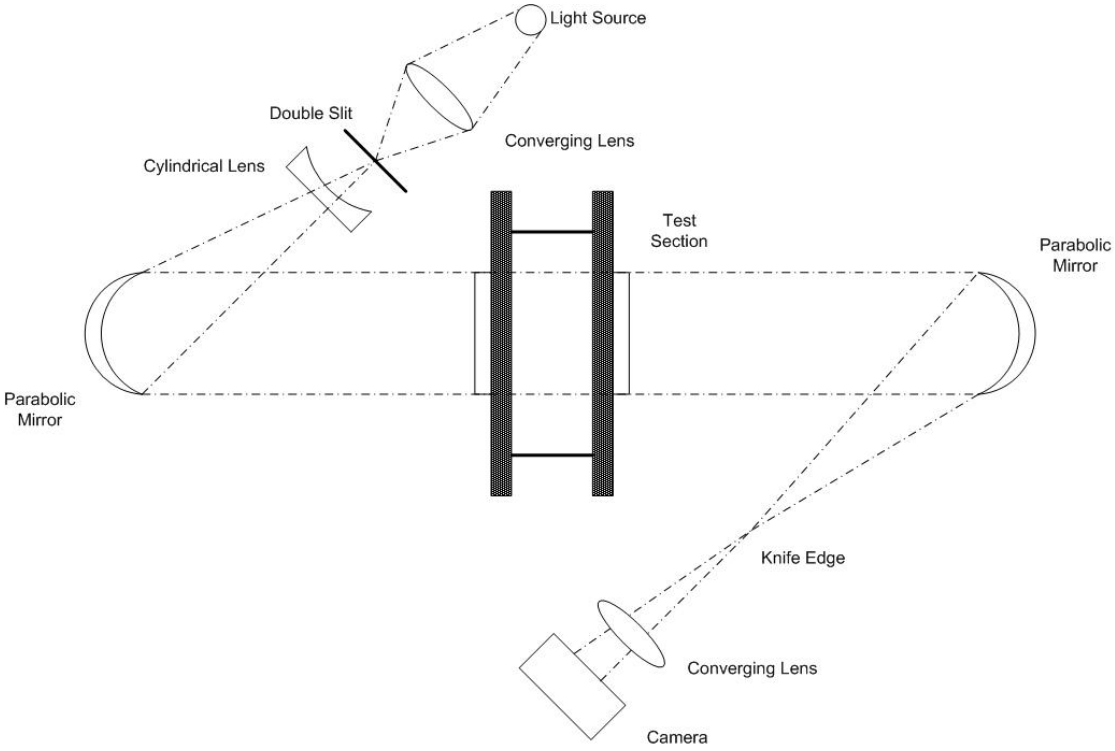

Figure 3.9: Z-arrangement for the optics set-up

The experimental images need to be of high resolution. For this purpose, two set-ups were used; shadowgraph and schlieren. These set-ups are built on the foundation of the Z-arrangement.

The difference in these systems is that on the camera side, the knife edge is removed for the shadowgraph system. Therefore the schlieren system is more sensitive since it shows density gradients; however the vortices appear as a haze. The schlieren system was used at Mach 1.32 since it gave an idea of the positioning and structure of vortices. At the higher Mach numbers, 1.42 and 1.6, the shadowgraph system was employed as it enabled the finer details of the vortex structure to be seen due to the fact the images displayed a shadow of the vortices.

To further enhance the images, some fine tuning was done. The light source shone through the double slit was reduced to a point. Additionally the knife edge on the camera side was closed to allow just enough light to pass through. After fine tuning, a better resolution was achieved for the images at M1.6.

3.8 Conclusions

The Mach numbers chosen were consistent, such that the outputted Mach number varied from the desired Mach number, in most cases, by less than 1%.

The design of the test piece was such that the surface of the model was flush, and could withstand the force of the shock. It enabled the vortices shed of the upstream and downstream edges to be seen.

A standard Z-arrangement was used for the optics set-up. Schlieren imaging was used at the lowest Mach number, whereas shadowgraph imaging was used for the higher Mach numbers. Fine tuning of the optics was done to ensure high resolution images were produced.

4 Computational Modelling of Vortex Shedding for Impulsive flow over a Discontinuous Edge

4.1 Introduction

CFD is an integral part of this study. Therefore accurate solutions in terms of modelling and resolution must be produced.

In order to produce an accurate model the solutions will have to be mesh independent. This is the process of having three different sized meshes and showing similar solutions are reached. Other methods of verification include using different modellers as well as different shaped meshes.

The resolution of the solution is limited by the processing power of the computers. However the resolution of the solution can be and is measured against the high quality experimental images.

4.2 Geometry

The entire model that was used during experimentation was not replicated computationally. The main section that was drawn was the diffraction edge.

The generic mount was not needed since the CFD program, Fluent, can generate a planar shock through the boundary conditions specified. The most difficult task was generating the discontinuous edge. This was achieved by drawing one section of the edge and extruding 38mm. A three-dimensional model was created, and the second edge was drawn on the face of the first edge and extruded in the opposite

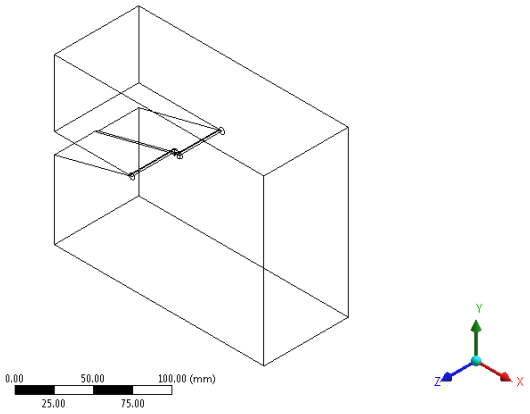

Figure 4.1: The fluid domain

direction. The length of the second edge was changed to produce the offset edge length required.

The dimensions of the flow domain were constrained by the test section: 76mm x 189mm x 148mm. The value of 148mm does not correspond to the height of the test section; 220mm. If the domain was drawn to that particular dimension a large mesh would have been produced, meaning computation would have taken a longer time. The additional 72mm would have increased the height of the shock but would have provided no additional insight into the flow features.

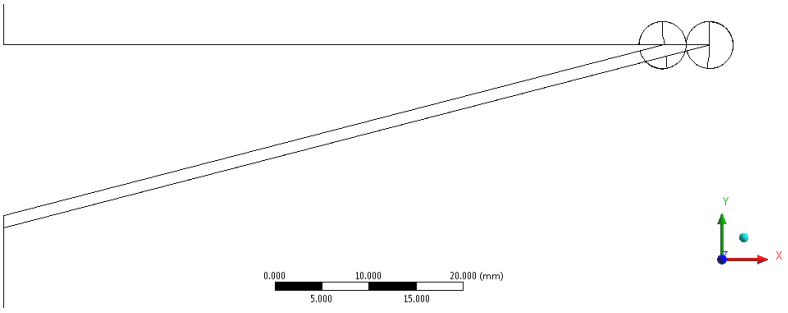

Figure 4.2: Sideview of the discontinuous edge

4.3 Mesh

The key area of investigation was the flow around the diffraction edge. Given that the geometry was not simple to mesh, the area around the diffraction edge had to be meshed independently. In order for this to be achieved, the area around the diffraction edge had to be a separate body as shown in figure 4.2. The Boolean operators were used to accomplish this.

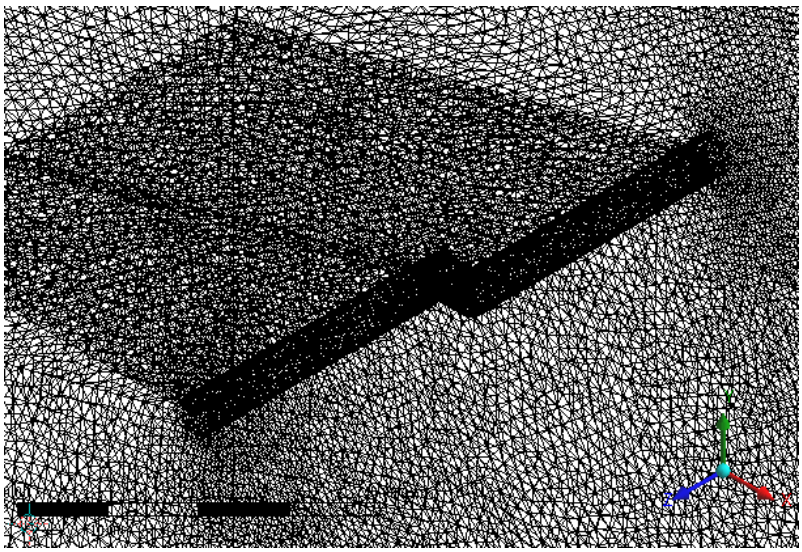

Figure 4.3: Meshing of the discontinuous edge

A combination of the domain being split into two bodies and the shape of the geometry meant Fluent was unable to convert the unstructured mesh into a quadrilateral mesh with the computational power available.

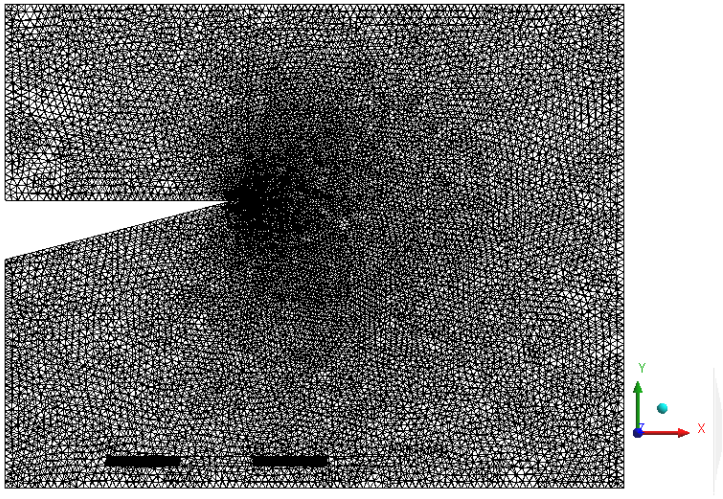

Figure 4.4: Side view of the mesh

An element size of 5mm was used. Each offset edge had the same size elements for the different boundary conditions.

In order for the flow to travel in the right direction and with the correct velocity; the surfaces of the flow domain had to be properly named. Figure 4.5 illustrates how the domain was named.

Table 4.1: The number of elements used for the different offset edge lengths

Offset edge length (mm)	**Number of elements**
5	908 623
10	850 370
20	1 206 545

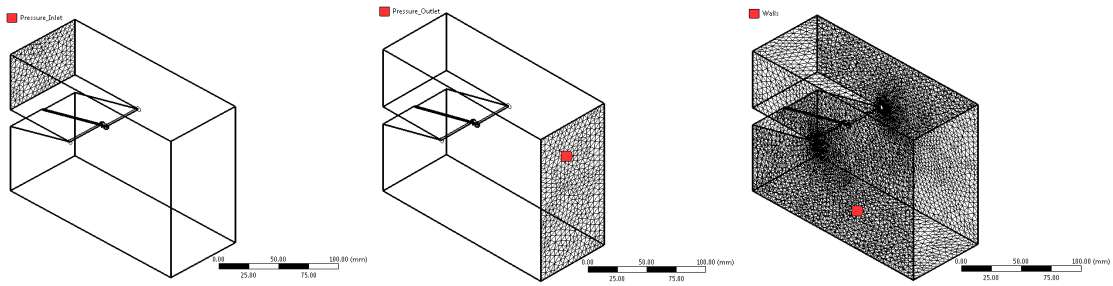

Figure 4.5: Naming of the faces of the fluid domain; Pressure Inlet (left), Pressure Outlet (centre) and Walls (right)

4.4 Boundary Conditions

In order to calculate the pressure inlet conditions, the standard gas dynamics equations were used. The standard atmospheric pressure was used instead of the pressure in Johannesburg to ensure the repeatability of the simulation.

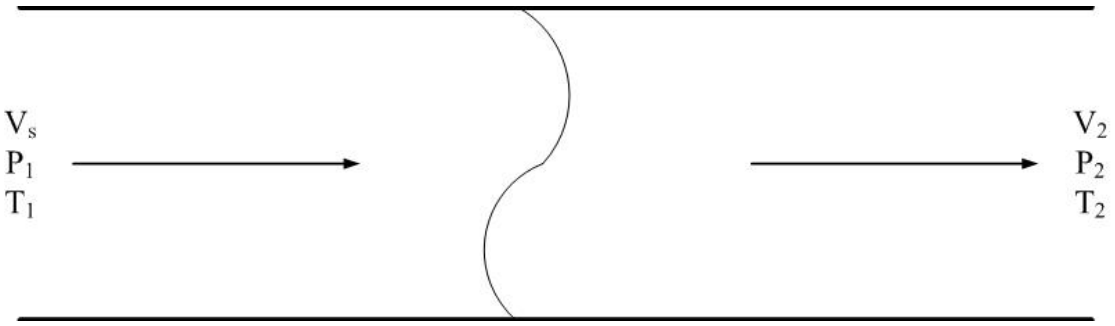

Figure 4.6: Stationary Shock

A sample calculation using of shock strength of M1.32 is given below. The initial conditions are as follows:

- $M_s = 1.32$
- $P_1 = 101\ 325$Pa
- $T_1 = 300$K

The upstream velocity is initially calculated:

$$\begin{aligned} V_1 &= M_1\sqrt{(\gamma-1)C_P T_1} \\ &= 1.32\sqrt{(1.4-1)(1006)(300)} \\ &= 458.63 m/s \end{aligned} \tag{4.1}$$

Calculate the downstream static pressure and temperature, Mach number and velocity:

$$\begin{aligned} T_2 &= T_1\frac{(1+\frac{\gamma-1}{2}M_1^2)(\frac{2\gamma}{\gamma-1}M_1^2-1)}{\frac{(\gamma+1)^2}{2(\gamma-1)}M_1^2} \\ &= 300\frac{(1+\frac{1.4-1}{2}1.32^2)(\frac{2(1.4)}{1.4-1}1.32^2-1)}{\frac{(1.4+1)^2}{2(1.4-1)}1.32^2} \\ &= 361.06K \end{aligned} \tag{4.2}$$

$$\begin{aligned} P_2 &= P_1\left(\left(\frac{2\gamma}{\gamma+1}\right)M_1^2-\left(\frac{\gamma-1}{\gamma+1}\right)\right) \\ &= 101325\left(\left(\frac{2(1.4)}{1.4+1}\right)1.32^2-\left(\frac{1.4-1}{1.4+1}\right)\right) \\ &= 189086 Pa \end{aligned} \tag{4.3}$$

$$\begin{aligned} M_2 &= \sqrt{\frac{\left(M_1^2+\frac{2}{\gamma-1}\right)}{\left(\left(\frac{2\gamma}{\gamma-1}\right)M_1^2-1\right)}} \\ &= \sqrt{\frac{\left(1.32^2+\frac{2}{1.4-1}\right)}{\left(\left(\frac{2(1.4)}{1.4-1}\right)1.32^2-1\right)}} \\ &= 0.78 \end{aligned} \tag{4.4}$$

$$
\begin{aligned}
V_2 &= M_2\sqrt{(\gamma-1)C_P T_2} \\
&= 0.78\sqrt{(1.4-1)(1006)(361.06)} \\
&= 295.79 m/s
\end{aligned} \tag{4.5}
$$

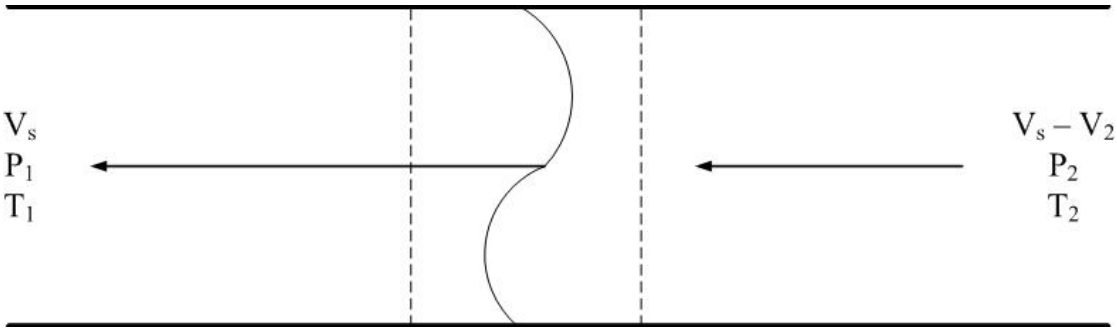

Figure 4.7: Moving reference frame as attached to the shock

A moving shock as is the case in the current study, can be analysed as a stationary shock if the correct reference frame is taken. A reference frame must be taken such that the observer is attached to the shock and the shock is stationary (Figure 4.7).

Static conditions such as pressure and temperature are unaffected. Stagnation conditions on the other hand change since it is velocity dependent.

Downstream stagnation pressure and temperature are the same as the downstream static pressure and temperature. There are changes to the upstream conditions are follows:

$$
\begin{aligned}
V_{abs} &= V_s - V_2 \\
&= 458.63 - 295.79 \\
&= 162.84 m/s
\end{aligned} \tag{4.6}
$$

$$
\begin{aligned}
M_{abs} &= \frac{V_{abs}}{\sqrt{(\gamma-1)C_P T_2}} \\
&= \frac{162.84}{\sqrt{(1.4-1)(1006)(361.06)}} \\
&= 0.43
\end{aligned} \tag{4.7}
$$

$$
\begin{aligned}
P_{01} &= P_1 \\
T_{01} &= T_1
\end{aligned}
\tag{4.8}
$$

$$
\begin{aligned}
P_{02} &= P_2\left(1 + \frac{(\gamma-1)}{2}M_{abs}^2\right)^{\frac{\gamma}{\gamma-1}} \\
&= 189086\left(1 + \frac{(1.4-1)}{2}1.32^2\right)^{\frac{1.4}{1.4-1}} \\
&= 214366.7Pa
\end{aligned}
\tag{4.9}
$$

$$
\begin{aligned}
T_{02} &= T_2\left(1 + \frac{(\gamma-1)}{2}M_{abs}^2\right) \\
&= 300\left(1 + \frac{(1.4-1)}{2}1.32^2\right) \\
&= 374.24K
\end{aligned}
\tag{4.10}
$$

The same parameters were calculated for M1.42 and M1.6. The results are displayed in table 4.2.

Table 4.2: Boundary conditions for the higher Mach numbers

	Mach 1.42	**Mach 1.6**
V_s	493.38	555.92
T_2	380.29	416.39
P_2	221 476.2	285 736.5
M_2	0.73	0.67
V_2	286.13	273.62
V_{abs}	207.25	282.30
M_{abs}	0.53	0.69
P_{02}	268 128.6	392 725.7
T_{02}	401.64	456

The remaining Fluent settings are illustrated in table 4.3. A few settings were investigated as shown in later section, namely turbulence models and solution methods.

Table 4.3: Fluent Settings

Solver	Density-Based
	Transient
Models	Energy-Equation
	Inviscid
	(Changed for investigation purposes)
Materials	Air - Ideal Gas
Boundary Conditions	Mentioned Above
Reference Values	Computed from
	Pressure Outlet
Solution Methods	Formulation - Explicit
	(Changed for investigation)
	Flux Type - AUSM
	Gradient - Green
	-Cell Based
	Flow - Third-Order
	MUSCL
	Transient Formulation -
	Explicit
Solution Controls	Courant Number - 0.5
Monitors	Residuals - Increase all residuals
	by a factor of 10
	The energy residual is increased
	by a factor of 1000
Solution Initialization	Initialize from
	Pressure Outlet
Calculation Activities	Autosave every 500
	iterations
	Mesh adpation commands.
	Allows the mesh to be adpated
	with temperature, pressure,
	velocity, and density.
	Adpation occurs every 10
	timesteps.
Run Calculation	70 000 iterations

4.5 Verification

Verification is the process of looking for errors in the implementation of CFD models. Therefore certain parameters were changed, whilst the rest remained constant, including:

- Refinement of the mesh (Mesh Independence)
- Shape of the mesh
- Explicit vs. Implicit solvers
- Euler vs. Navier-Stokes models

The time taken after the shock was diffracted over the longer part of the test piece (experimentally) was taken as the reference point. The procedure is given in section 3.5. The various time instances in the CFD model are saved in timesteps. The challenge for the four mentioned cases is finding timesteps where position of the shock, with regards to time, is similar to the experimental data or as the case may be other CFD models.

4.5.1 Mesh Independence

In an attempt to prove mesh independence, meshes of three different sizes were produced; with the element cell size changing from 2.5mm to 3.5mm to 5mm. The corresponding numbers of cells were calculated as well as the percentage difference with respect to the cell size of 5mm.

Table 4.4: Number of cells per model

Cell Size(mm)	**Number of cells**	**Percentage Difference**
5	908 623	0
3.5	988 358	8.78
2.5	1 406 394	54.78

The process for determining the timesteps for the different models was time consuming as the time as was calculated for the computational case and thereafter compared to the experimental case. Once the times matched, as closely as possible, the corresponding timestep was selected. The 5mm offset edge length at Mach 1.32 was used as the reference criteria.

Table 4.5: Timesteps for the different mesh sizes

Time(μs)	**5mm**	**3.5mm**	**2.5mm**
-7.62	17 000	17 000	17 000
0	18 000	18 000	18 000
13.30	20 000	20 000	20 000
19.97	21 000	21 000	21 000
30.28	23 000	23 000	23 000
43.67	24 500	25 000	25 000
53.15	26 000	26 500	26 000
54.94	26 500	26 500	26 500
69.98	29 000	28 500	28 500
77.27	31 000	30 000	30 000
96.53	33 000	32 500	32 000
100.07	33 500	33 000	32 500
106.98	34 000	33 500	33 000

The size of the mesh varies. Table 4.5 highlights the fact that the timesteps for the three solutions are similar, implying that the flow progresses at similar speeds throughout the three models. On the other hand, the computational time increases as the cell size is dropped.

An alternate factor, which was mentioned previously, is that the timestep does not exactly match the time from the experimental images. If the computational model was saved more frequently, the difference in times would decrease.

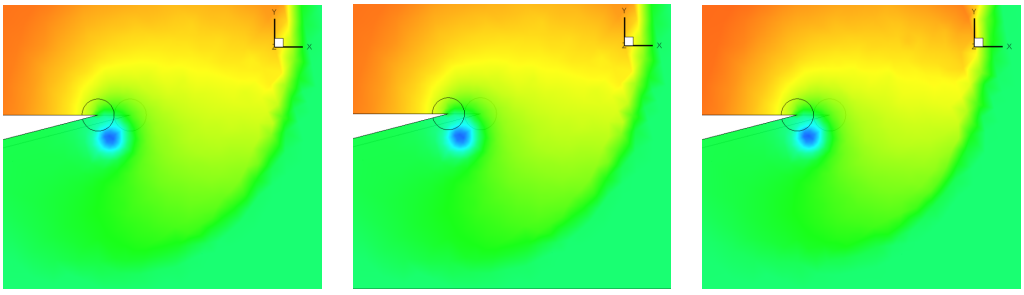

Figure 4.8: Density contours in the Z plane at the wall adjacent to the upstream edge for coarse (left), medium (middle), and fine (right) meshes at a time of $\pm$ 54μs after the shock has diffracted over the downstream edge for the 5mm model

Contours of density and Y-velocity were plotted, on the Z-plane. Figures 4.8 and 4.9 demonstrate that there are very few if any differences between the solutions. The shapes of the diffracted shock are clearly defined in the density contours across all three models. The density variation across the diffraction edge is another similar

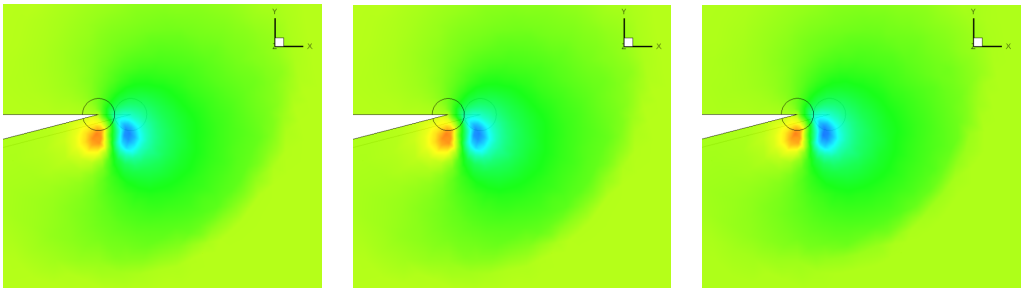

Figure 4.9: Y-velocity contours in the Z plane at the wall adjacent to the upstream edge for coarse (left), medium (middle), and fine (right) meshes at a time of $\pm$ 54μs after the shock has diffracted over the downstream edge for the 5mm model

feature.

The Y-velocity, as the name suggests, is the magnitude of the velocity in the Y-direction. It is a useful parameter in analysing the flow across the diffraction edge. The vortices and the vortex cores are easy to identify. As with the density contours, the Y-velocity contours show little to no variation across the different mesh sizes.

The solution is therefore mesh independent for the cell size available. The number of cells in the fluid domain are significantly less then the work done by Sun & Takayama (2002). The cell size of 5mm was used for the remainder of the simulations since it produced similarly accurate solutions as the 3.5mm and 2.5mm cell size models, but required less computational time.

4.5.2 Shape of Mesh

A quadrilateral mesh is a degree of order higher than the unstructured mesh. Naturally a quadrilateral mesh has a higher resolution for the same number of cells. The unstructured mesh allowed for a more refined mesh along the diffraction edge and offset edge length. This concept is clearly demonstrated in figure 4.10.

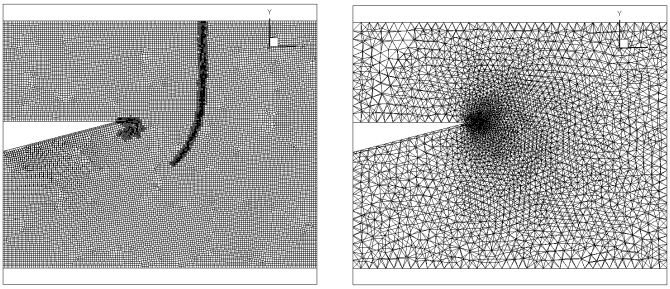

Figure 4.10: Quadrilateral (left) and Unstructured (right) meshes

A mesh adaption scheme was used. It operates by identifying regions where the temperature, pressure, velocity and density vary. In those regions the mesh is adapted by a refinement of 2, as shown by the quadrilateral mesh in figure 4.10. This process occurs every 10 timesteps.

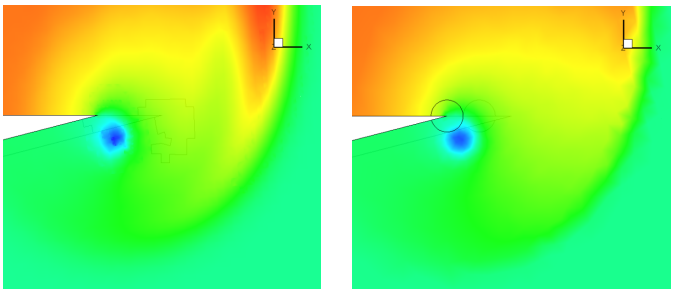

Figure 4.11: Density contours in the Z plane at the wall adjacent to the upstream edge of quadrilateral (left) and unstructured (right) meshes at a time of $\pm$ 45μs for the 10mm model

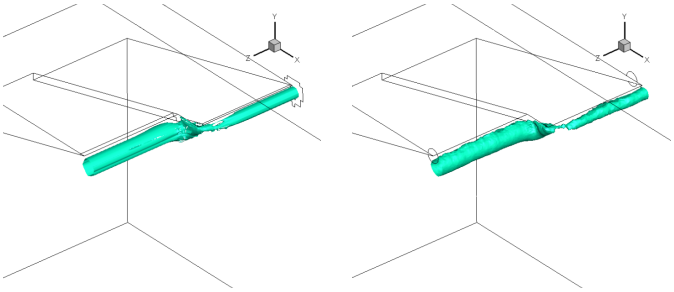

Figure 4.12: Density iso-surfaces of 1.1kg/m^3 for quadrilateral (left) and unstructured (right) meshes for the 10mm model at a time of $\pm$ 45μs

The density contours show expected results in that the shock is better resolved with the quadrilateral mesh. On the other hand, the scale indicates the unstructured mesh picks up finer density changes across the vortex. The unstructured mesh picks up densities of 0.5 kg/m^3 whereas the lower limit for the quadrilateral mesh is 0.9 kg/m^3. The unstructured mesh loses resolution of the shock but gains a higher resolution of the free vortices. This is evident in the plots of iso-surfaces of density. The plots are well defined and pick up subtle changes in comparison to the quadrilateral mesh.

The unstructured mesh was used since it allows for a more detailed analysis of the topology of the free vortices.

4.5.3 Type of Solver

The major difference between the choices of using explicit or implicit solvers was the timestep. For an implicit solution; the timestep has to be specified. Since the mesh around the diffraction edge is fine, the corresponding timestep would have to be small. Given that the timestep is constant for an implicit solution, many more iterations would have to be run for the flow to travel the appropriate distance.

In the explicit solver the solution was set to be saved every 500 timesteps. The more timesteps that were run the more developed the flow was.

The fine details of the mesh structure cannot be controlled, the mesh varies from model to model. Ideally the solution methods should be the same for all the models. With the 10mm offset edge length, simulations were crashing despite having the same conditions as the 20mm offset edge length. The problem was the Courant number, it needed to be decreased. The Courant number is the value by which the outputted numbers can vary from cell to cell. The larger the Courant number the bigger the difference from cell to cell, a quicker and more unstable solution will be formed.

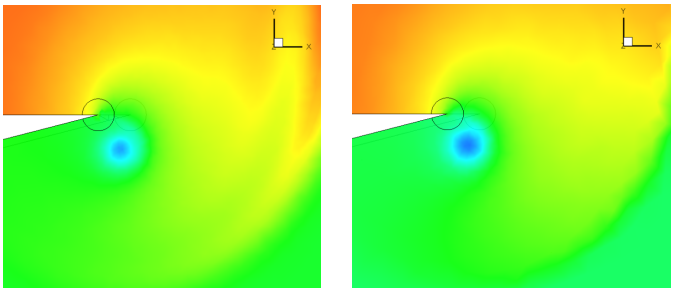

Figure 4.13: Density contours at M1.42 for an offset edge length of 5mm of implicit (left), and explicit (right) solutions at $\pm$ 65μs

The colour schemes between the two plots of density contours are different. There is a wider colour range for the implicit solution. The implicit solution shows a large density gradient; particularly at the vortex core (point of lowest density) of the upstream edge. The diffracted shock has a clearer definition in the implicit solution but the shape is not as clear in the explicit solution. The position of the shock and the vortex are similar for both solutions. However, the vortex is seen more distinctly with the explicit solution. The understanding of these vortices, the behaviour and topology are the crux of this investigation. The explicit solver was therefore used for the remaining solutions.

4.5.4 Turbulence Models

Since three dimensional vortex interactions are being investigated; inviscid solutions were run. This is true for the studies on vortex shedding from a discontinuous edge and vortex interaction from impulsive flow over edges. By using an inviscid model certain features can not be seen, i.e. the viscous vortex.

There are different turbulence models that can be used. The model used in the current study it the standard k-ϵ function. One would expect the results to be similar to the inviscid model.

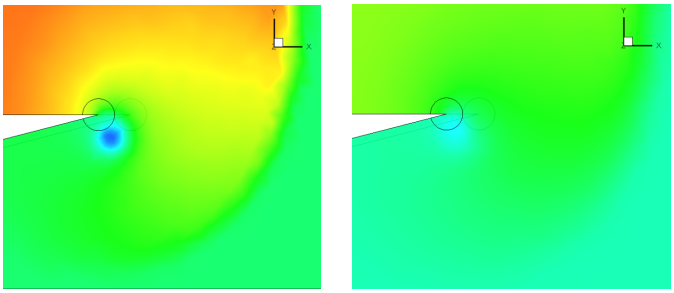

Figure 4.14: Density contours at M1.32 for an offset edge length of 5mm of Euler (left), and Navier-Stokes (right) solutions at $\pm$ 54μs

The solutions are similar with respect to the positioning, size and shape of the shock and the vortex. Although the expansion wave of the Navier-Stokes solution is smaller. Despite the colour range being different, the density variations are alike in terms of values. The models differ in the pattern of the density variations. In the Euler model, the shock and the pattern of the density variation has a clear resolution.

The Navier-Stokes solution shows no sign of the viscous vortex. Considering the diffracted shock is poorly resolved, one can assume that the resolution of the solution is of poor quality. A computer with a higher processing power is needed so a more refined mesh can be produced and the simulation itself can be run.

4.6 Validation

Validation is the procedure of checking whether the CFD adequately models the real life flow. The chances of matching the experimental images with CFD in terms of time are unlikely at best. Naturally there is a discrepancy with time, so there are differences between the two images; size and positioning of the vortices and

diffracted shock are two key differences.

The CFD images are made up of slices taken through the Z-plane. The density contours in colour are at the nearest face of the fluid domain (looking into the page), whereas the density contours in black are furthest away. Finally iso-surfaces of density are plotted.

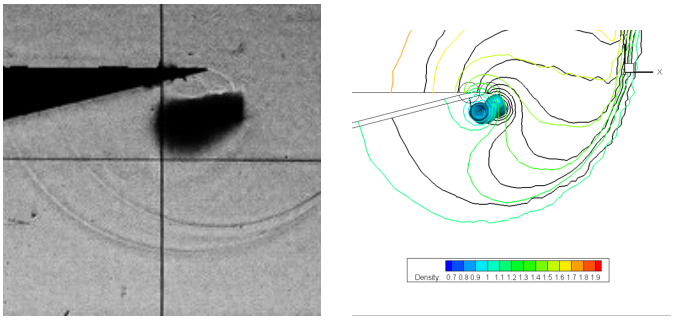

Figure 4.15: Comparison of experimental image (left) and CFD-density contours (right) at M1.32 of the 5mm offset edge length at time 70μs

Figure 4.15 shows similarities between the images. The vortices shed of the upstream and downstream edges are in similar positions in each of the images. It is challenging to locate the position of the vortices from the experimental image, since the schlieren system was used.

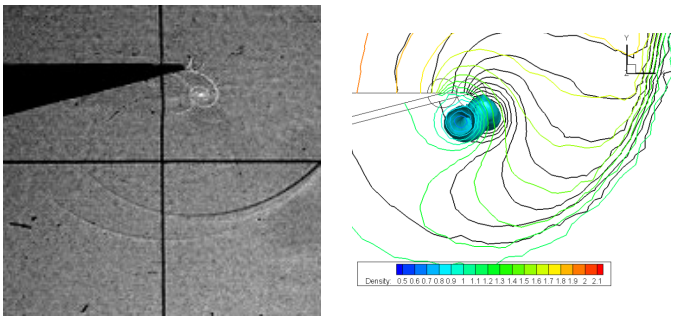

Figure 4.16: Comparison of experimental image (left) and CFD-density contours (right) at M1.42 of the 5mm offset edge length at time 75μs

As the shock passes over the model, diffraction initially occurs at the upstream edge and thereafter the downstream edge. There is a gap between portions of the shock diffracted of the upstream and downstream edges; clearly shown in both images.

Similar features are seen at higher Mach numbers. The key difference is that features such as shocklets at Mach 1.42 and lambda shock configurations at Mach 1.6 cannot be seen in the CFD. Reeves (2010) found similar results in his work on three-dimensional compressible vortices.

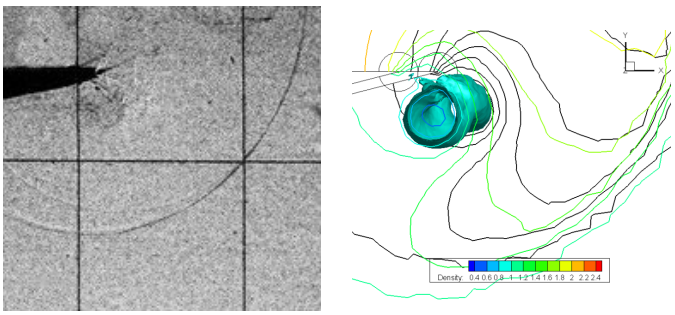

Figure 4.17: Comparison of experimental image (left) and CFD-density contours (right) at M1.6 of the 5mm offset edge length at time 58μs

Table 4.6: Time after the shock has diffracted (μs) for each Mach Number

Mach Number	**Time after shock has diffracted (μs)**
1.32	70
1.42	75
1.6	58

Table 4.6 shows the flow is the most developed for Mach 1.42. The images illustrate, specifically the CFD images, the vortex increasing in size with Mach number. A combination of the size of the vortex and the time after the shock has diffracted results in the flow developing at a quicker rate with an increase in Mach number.

The CFD matches the experimental results well and as well as in previous studies (Reeves (2010)). One can conclude that accurate CFD solutions have been run and can be used to understand the behaviour and topology of the vortices.

4.7 Conclusions

The CFD simulations accurately match the experimental data. For the simulations itself, it was found that a set number of conditions aided in analysing the flow; an explicit solver, an Euler model, and an unstructured triangular mesh.

It was determined, for a range of total number of cells; there were minimal changes with contours of density and Y velocity in the Z plane. The solution is therefore mesh independent.

5 Vortex Shedding from Impulsive flow over a Discontinuous Edge

5.1 Introduction

In this chapter analysis will be done on the experimental and computational results for vortex shedding over a discontinuous edge. The key focus of this chapter is the topology of the free vortices; namely what effect does Mach number and offset edge length have on vortex shape and structure.

The results obtained are presented in accordance with the Mach number, starting at Mach 1.32 and ending at Mach 1.6. The experimental images taken are displayed whereby the different test pieces are next to each other with the 5mm model on the left, 10mm model in the centre and 20mm model on the right. The time quoted in the images refers to the time taken after the shock has diffracted over the downstream edge. The same method for displaying the images is done for the CFD images (contour plots and plots of isosurfaces), unless stated otherwise.

It is highly unlikely for all the experimental and corresponding CFD images to be at exactly the same time. Therefore the time mentioned is an approximation.

5.2 Mach 1.32

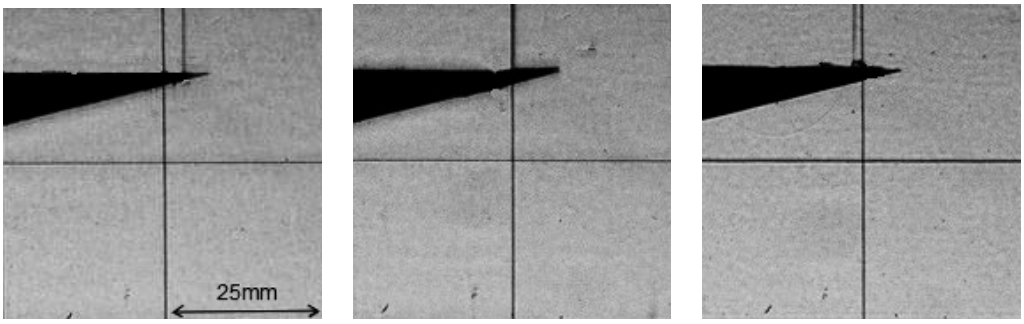

Figure 5.1: Experimental image of shock diffraction for Mach 1.32 at a time of ± -13μs

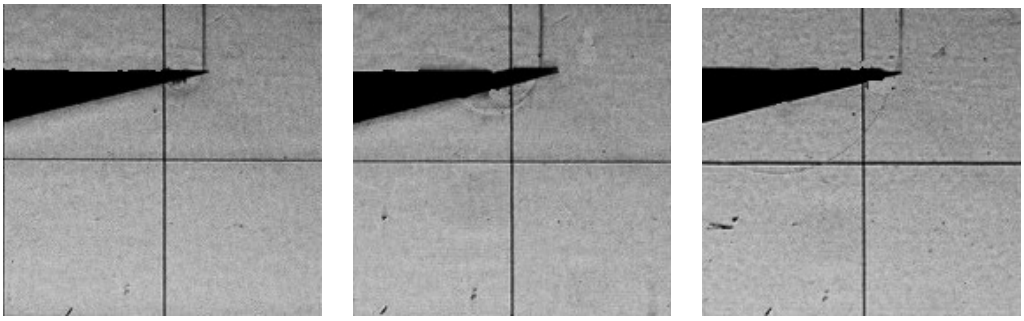

Figure 5.2: Experimental image of shock diffraction for Mach 1.32 at a time of ± -3μs

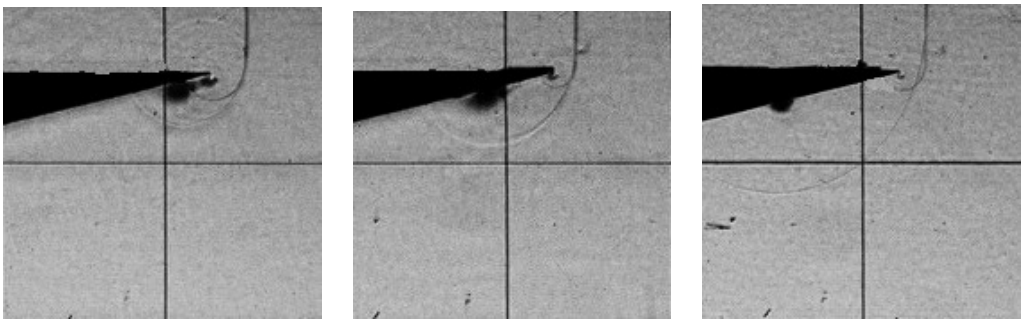

Figure 5.3: Experimental image of shock diffraction for Mach 1.32 at a time of ± 10μs

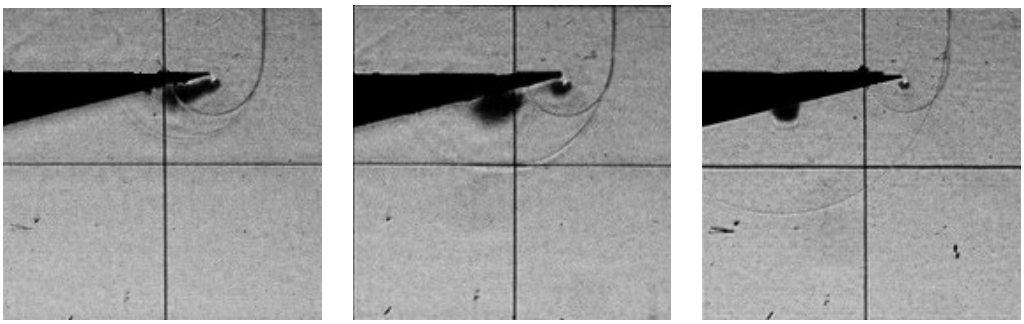

Figure 5.4: Experimental image of shock diffraction for Mach 1.32 at a time of ± 18μs

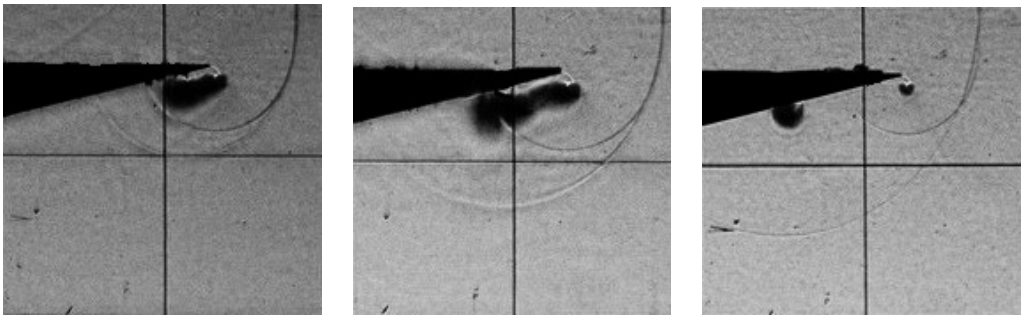

Figure 5.5: Experimental image of shock diffraction for Mach 1.32 at a time of ± 30μs

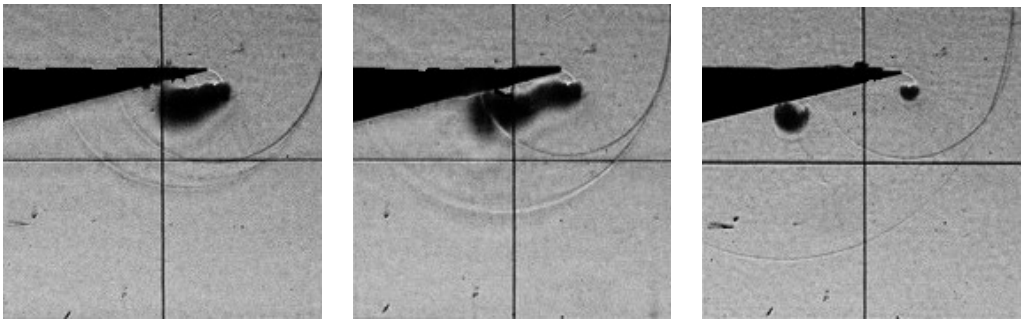

Figure 5.6: Experimental image of shock diffraction for Mach 1.32 at a time of ± 39μs

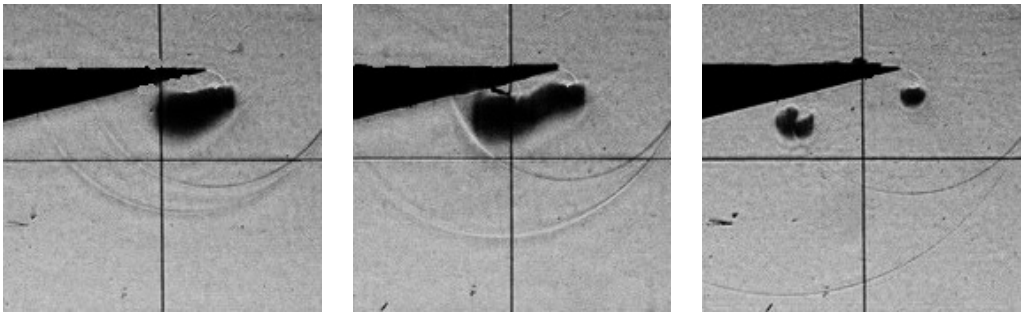

Figure 5.7: Experimental image of shock diffraction for Mach 1.32 at a time of ± 52μs

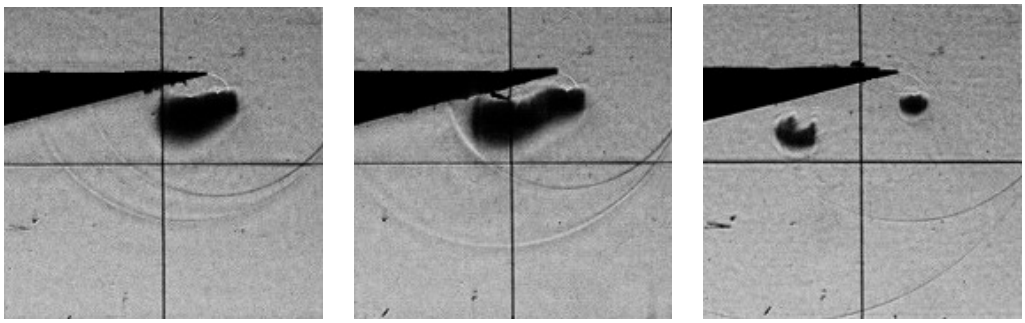

Figure 5.8: Experimental image of shock diffraction for Mach 1.32 at a time of ± 56μs

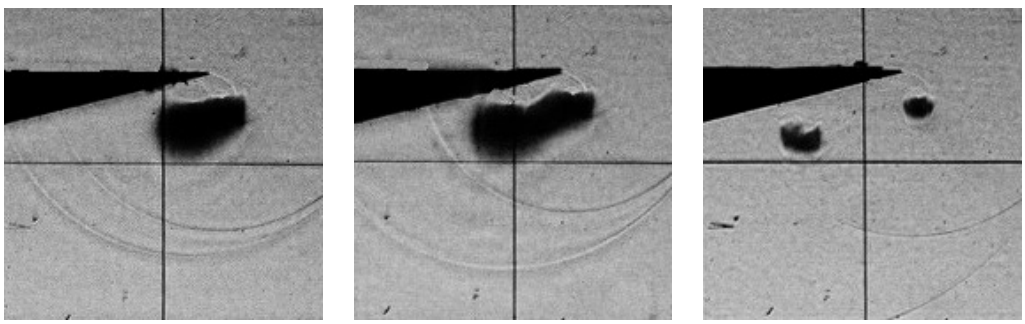

Figure 5.9: Experimental image of shock diffraction for Mach 1.32 at a time of ± 66μs

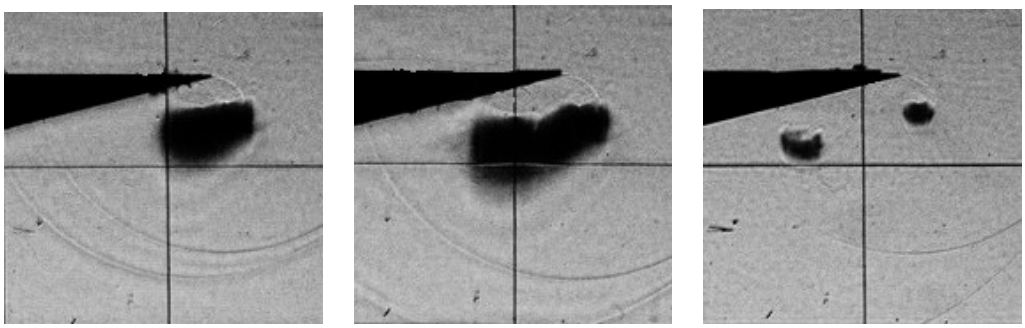

Figure 5.10: Experimental image of shock diffraction for Mach 1.32 at a time of ± 80μs

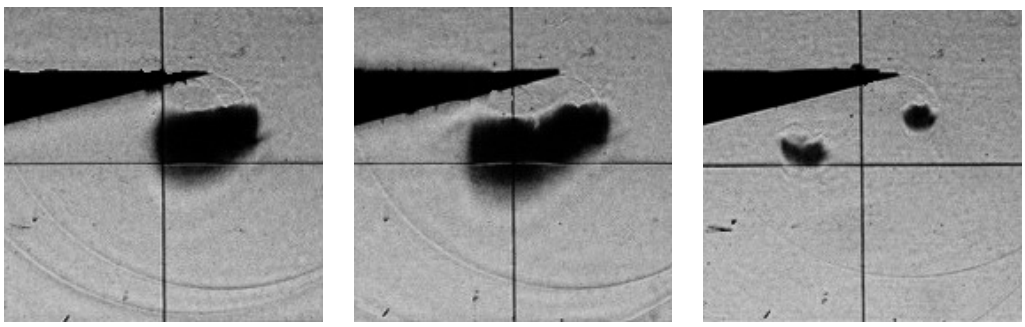

Figure 5.11: Experimental image of shock diffraction for Mach 1.32 at a time of ± 92μs

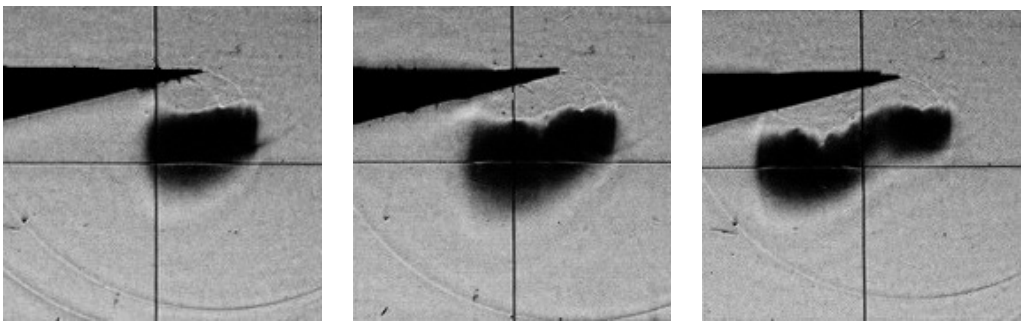

Figure 5.12: Experimental image of shock diffraction for Mach 1.32 at a time of ± 100μs

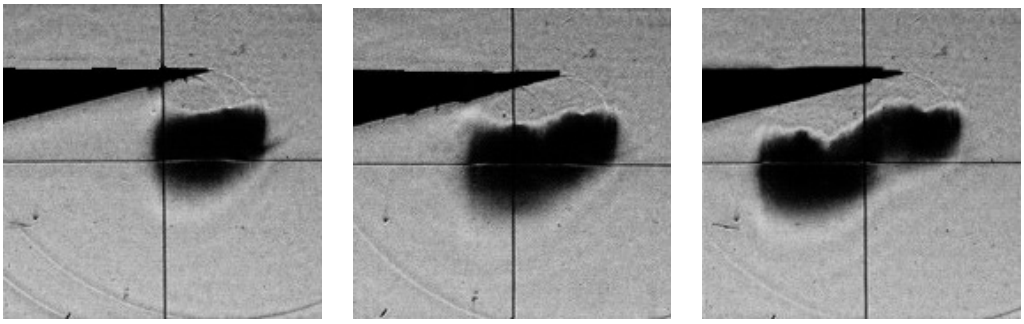

Figure 5.13: Experimental image of shock diffraction for Mach 1.32 at a time of ± 108μs

The features displayed throughout the experimental images are similar to those in the two-dimensional shock diffraction case (figure 1.1). The fundamental differences are the vortex shed of the downstream edge and the shape of the diffracted shock wave.

One feature that cannot be accounted for is the viscous vortex. The sensitivity of the images is a possible explanation, since the images taken for Mach numbers 1.32, 1.42, and 1.6 do not have as high resolution in comparison to figure 1.3. An additional reason may be the shape of the models:

- The viscous vortex formed from the upstream edge may be hidden by the geometry of the downstream edge.
- The viscous vortex formed as a result of the downstream edge could be blocked by the free vortex from the upstream edge.

A common feature in the two and three dimensional cases is the shear layer. The shear layer is formed with the high velocity air interacting with the effectively stationary air around the diffraction edges. The shear layer becomes larger and more

curved with time. The free vortex forms at the point at which the shear layer is most curved.

The timing between the images is not completely accurate; due to the trigger delay which is controlled by a transducer. With such high speeds it is impossible to get the shock wave to be in the same position on a consistent basis. Therefore a variation of a $\pm$ 15μs is experienced within some images. This is a significant difference between images, but it provides insight into the effect of time on the flow.

5.2.1 Free Vortices

The free vortices are time and space dependant. The effect of time is seen from the experimental images; which spans a period of $\pm$ 120μs.

Early on in the flow domain the vortices appear to behave independently. There is a clear distinction with the vortices shed of the downstream and upstream edges. According to Helmholtz's laws, vortices cannot end in space. There is a possibility of the vortices attaching to the underside of the model or ending at the viewing window.

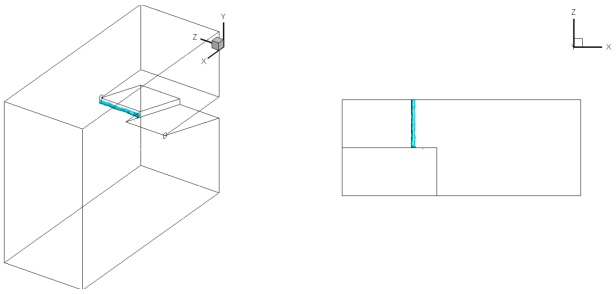

Figure 5.14: Plots of iso-surfaces of density for a time delay of $\pm$ 10μs

The corresponding CFD image (figure 5.14) to the experimental image with an offset edge length of 20mm (figure 5.3) shows that the vortex produced of the upstream edge.

As the flow progresses, there is an interaction between the vortices shed off the upstream and downstream edges. For the different offset edge lengths, amalgamation occurs at different times. Amalgamation is defined as the joining of the vortices.

The vortex strength is a function of vorticity, in other words how quickly the fluid rotates about itself. In the initial stages of shock diffraction, the vortices are condensed in terms of the shape (figures 5.5 to 5.13). The positioning of the vortices, relative to the diffraction edge, shifts down and to the right with the development

of the flow. These observations have been confirmed by the vorticity magnitude plots in figures 5.15 and 5.16. With an increase in offset edge length, the shock has a further distance to travel from the upstream to downstream edge. There is therefore a lag as to when the vortices merge for the different offset edge lengths.

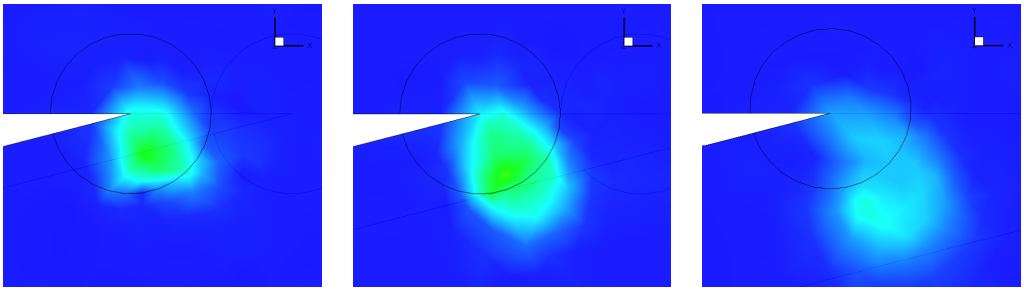

Figure 5.15: Plots of vorticity magnitude at a time delay of $\pm$ 10μs in the Z plane at the wall adjacent to the upstream edge

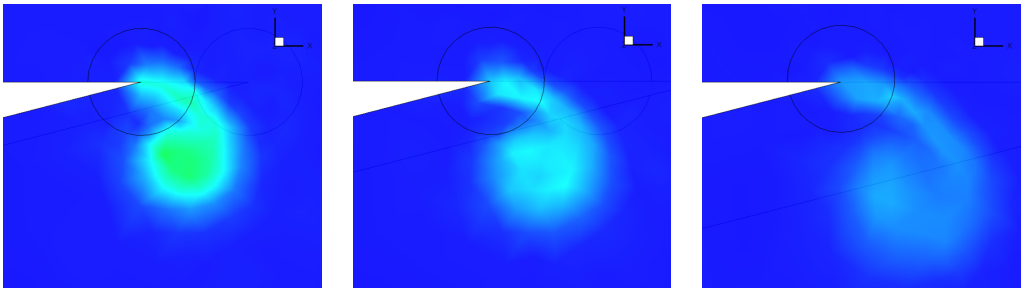

Figure 5.16: Plots of vorticity magnitude at a time delay of $\pm$ 55μs in the Z plane at the wall adjacent to the upstream edge

Table 5.1: Time Delays

Offset Edge Length(mm)	**Approximate time delay for when vortices have amalgamated(μs)**
5	13
10	32
20	95

Table 5.1 and figures 5.7 to 5.13 show the vortices shed off the 20mm model amalgamate after a longer period of time then either the 5mm or 10mm models. This suggests that the offset edge length has a significant impact on the structure of the vortices.

The times in table 5.1 are based on the schlieren images, where the up and downstream vortices can be seen to be merged for the first time. If one uses smaller time increments, the point at which the vortices amalgamated would be at a higher resolution. However the key point of the analysis is to determine whether the offset edge length has an effect on the rate of amalgamation. This is best achieved by

non-dimensionalising time for amalgamation with the time the shock takes to move from the upstream to the downstream edge. This value is calculated from simple mechanics, since the distance and Mach number are known.

Table 5.2: Non-dimensionalised time

	5mm	**10mm**	**20mm**
Time for amalgamation (μs)	13	32	95
Time to cover distance of offset edge length (μs)	11	22	44
Non-dimensionalised time	1.18	1.45	2.15

The fact that the non-dimensional times increase (table 5.2) shows that the rate of amalgamation increases with the size of the offset edge length.

When the Mach number is increased; there is a change in optics systems. The shadowgraph system does not allow for the points of amalgamation to be defined in the same manner as the schlieren system. Therefore the approach used at Mach 1.32 cannot be used at higher Mach numbers. However, given that all the other factors are kept constant, one would expect the rate of amalgamation to decrease at higher Mach numbers.

As has been stated; the vortices merge the quickest for the 5mm model. Considering the value of the offset edge length is small; the schlieren system cannot distinguish between the individual vortices. The structure (figures 5.5 to 5.13) of the merged vortex (defined as the amalgamation of the upstream and downstream vortices along the discontinuity) is elongated and has the shape similar to that of a quadrilateral. As time passes the merged vortex expands in the horizontal and vertical direction.

In the case of the 10mm model; the merged vortex has a different shape in the sense the individual vortices can be seen for a longer period of time, which adds to the curvature of the structure. The individual vortices can still be identified up to a time delay of $\pm$ 16μs. The merged vortex is more stretched in the horizontal direction in comparison to the 5mm model. Similarly the merged vortex from the 20mm model is more stretched then the 10mm model. This suggests that this phenomenon occurs with increasing offset edge length until the vortices shed of the upstream and downstream edges behave completely independently of one another.

In the case of the 20mm model; the vortices behave independently for 90μs out of the total 120μs. In the images in which the vortices are merged (figures 5.12 and 5.13), the individual vortices can easily be identified by the shape of the merged vortex.

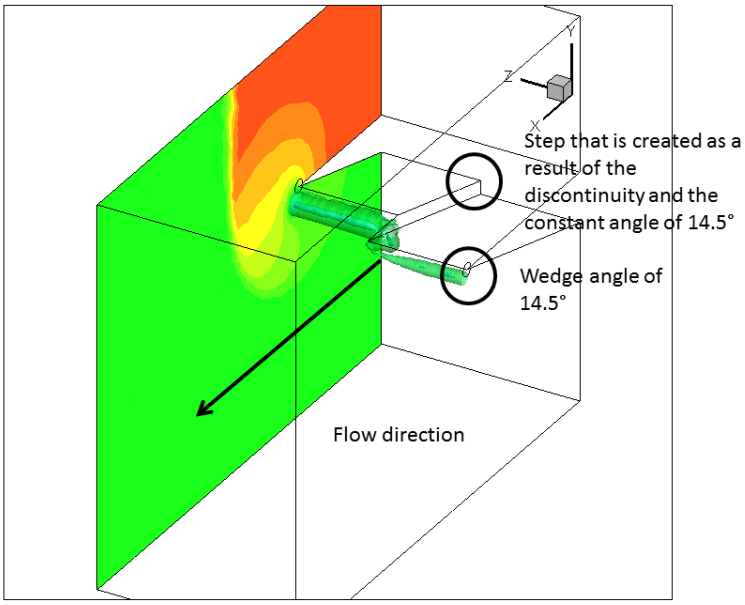

Figure 5.17: An indication of the direction of flow and the isosurfaces are taken with regards to the entire flow domain

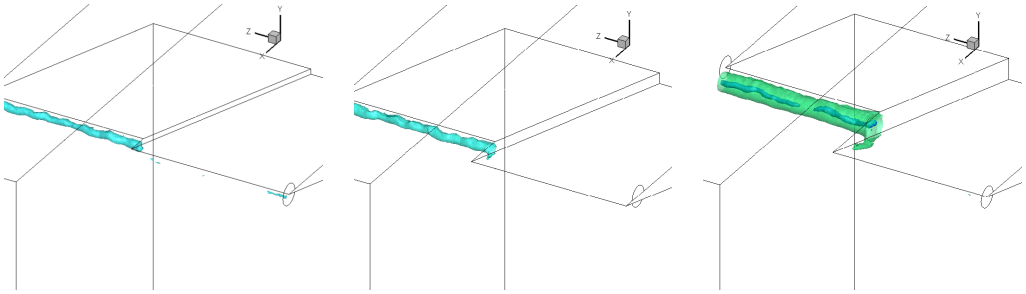

Figure 5.18: Isosurfaces of density of a value of 0.8 kg/m^3 on the inner surface and 1.1kg/m^3 on the outer surface at a time delay of $\pm$ 10μs

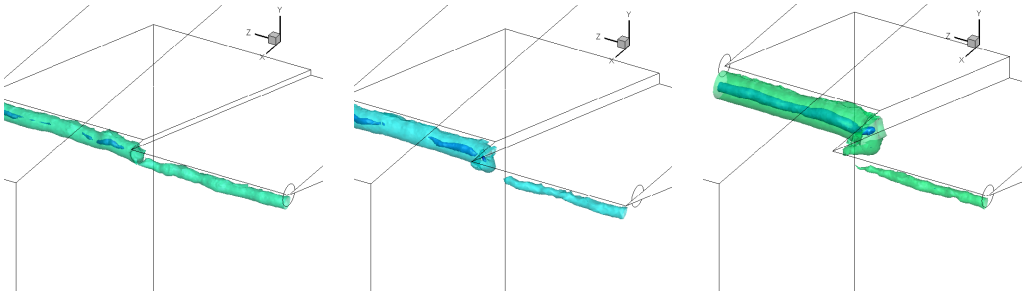

Figure 5.19: Isosurfaces of density of a value of 0.8 kg/m^3 on the inner surface and 1.1kg/m^3 on the outer surface at a time delay of $\pm$ 30μs

Images of the flow are taken in increments of time which are common across the various models. Figure 5.20 shows that the smaller the offset edge length the stronger

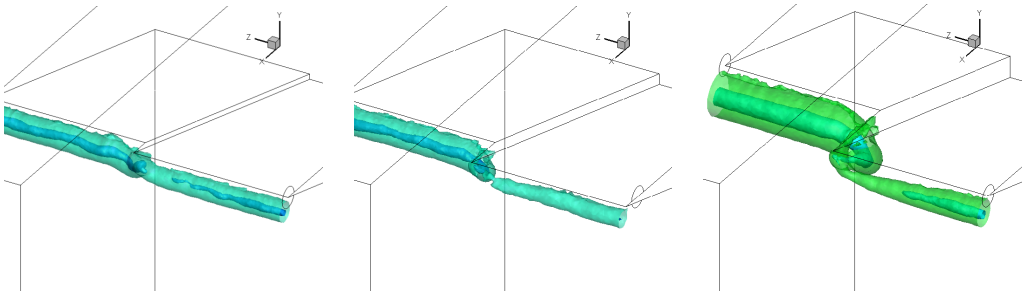

Figure 5.20: Isosurfaces of density of a value of 0.8 kg/m^3 on the inner surface and 1.1kg/m^3 on the outer surface at a time delay of $\pm$ 56μs

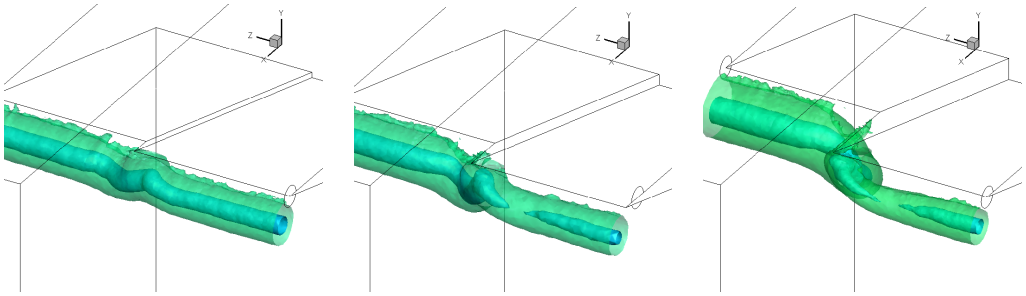

Figure 5.21: Isosurfaces of density of a value of 0.8 kg/m^3 on the inner surface and 1.1kg/m^3 on the outer surface at a time delay of $\pm$ 108μs

the interaction between the vortices. The vortex shed off the downstream edge ends at the viewing window and the discontinuity; where there is interaction with the vortex from the upstream edge. The variation of the isosurfaces of density with regards to shape and structure along the Z axis are demonstrated by figures 5.18 to 5.21. The value of isosurfaces displayed are 0.8 kg/m^3 on the inner surface and 1.1 kg/m^3 on the outer. When other isosurfaces of density are presented; the format is the same.

There are rapid changes in shape of the isosurfaces along the Z axis, in some cases to the point of nothing. This predominantly occurs for the 20mm model, which suggests that there is a change in density in these regions. The vortex has different densities at different points. The fact that it cannot be picked up by a small value of isosurface is an indication that it's density value is higher than the indicated isosurface of 0.8 kg/m^3.

Figure 5.21 shows the impact the offset edge length has on the vortices shed of the upstream and downstream edges. There is however, a more significant effect on the downstream edge. The size of the portion of the vortex adjacent to the discontinuity is significantly reduced in size. There is an inverse relationship between the size of this part of the vortex and the size of the offset edge length, the larger the

discontinuity the smaller (in terms off cross-sectional diameter) the corresponding portion of the vortex is. There is a more significant change in density for a larger offset edge length.

The experimental images provide some indication of the interaction of the vortices. Features such as stretching, twisting and curvature of the merged vortex around the discontinuity can be seen in both set of images (computational and experimental). In the case of the experimental images, only a brief overview is given in terms of these features, since the optics were setup normal to the flow. As a result the images taken experimentally are of a particular plane in a three dimensional field. In terms of the computational simulations; images can be obtained from any number of angles, therefore further insight is gained of the mechanics of the flow.

In the computational models as with the experimental models, the vortices get larger and shift further away from the diffraction edges with time (figures 5.18 to 5.21).

The schlieren system is sensitive; as shown for the experimental images for the 5mm and 10mm models. There is no indication of an interaction between the vortices from the 20mm model until a time of 95μs, which is a long time period with including the fact that the interaction between these vortices drop as the size of the discontinuity increases. At a time of 95μs there is a strong interaction.

To analyse the isosurfaces, slices of density contours will be taken in the Z plane, along the Z axis (figure 5.22). Nine evenly spaced slices are taken along the Z axis, the distance between each slice is $\pm$ 9.5mm at a time of $\pm$ 109μs.

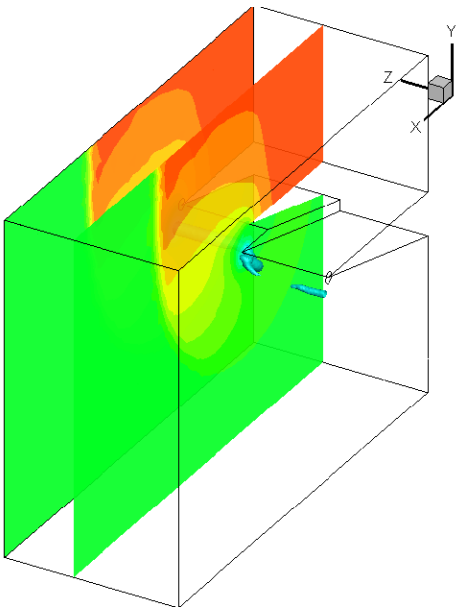

Figure 5.22: Density contours of the 20mm model in the XY plane at 109μs

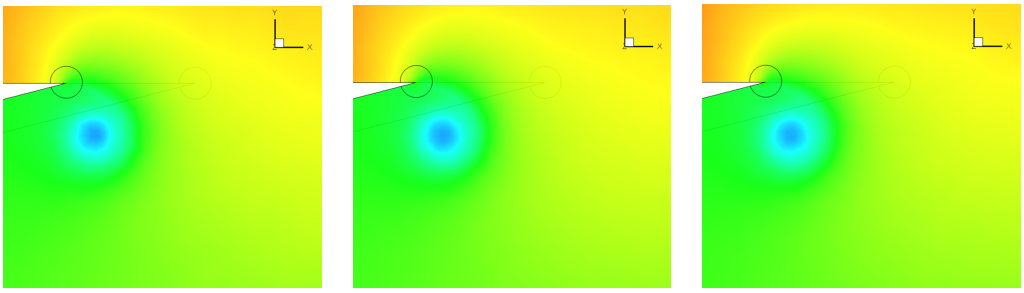

Figure 5.23: Slices of density contours at positions 1(left), 2(centre), and 3(right)

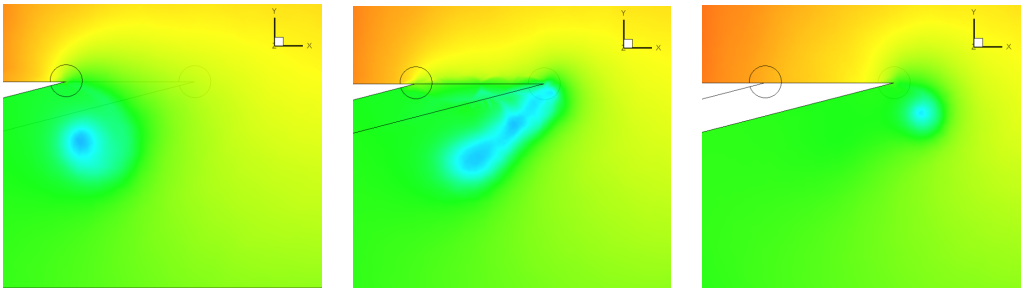

Figure 5.24: Slices of density contours at positions 4(left), 5(centre), and 6(right)

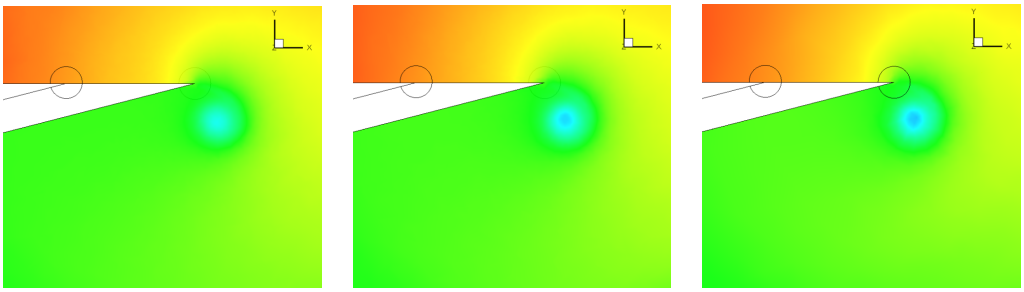

Figure 5.25: Slices of density contours at positions 7(left), 8(center), and 9(right)

The slices of density contours show that the topology along the downstream and upstream edges is consistent. However in close proximity to the offset edge length, there is a significant change in topology. This is clearly evident in figure 5.24. The vortex close to the discontinuity (figure 5.24 - position 4) on the upstream edge is at a lower density value than the vortices in figure 5.23. A similar case is reached with the vortex at the beginning of the downstream edge (figure 5.24 - position 6), it is at a lower density value near the vortex core then the vortices in figure 5.25, which is an indication that the flow is more developed around the upstream edge then the downstream edge. The term vortices used in this paragraph is not used to refer to multiple vortices in the flow but to one vortex cut at multiple sections. These changes in shape reflect what was being viewed on the plots of isosurfaces. At the discontinuity the vortex is stretched (figure 5.24 - position 5), showing the link between the vortices shed of the upstream and downstream edges.

5.2.2 Effect of Discontinuity

It has been established that the flow around and at the offset edge length is complex. Figure 5.24 - position 5 shows there is a major change in the values of density (particularly from the isosurfaces of density) as well as in the shape of the density contours about the discontinuous edge. This feature will be looked at in detail.

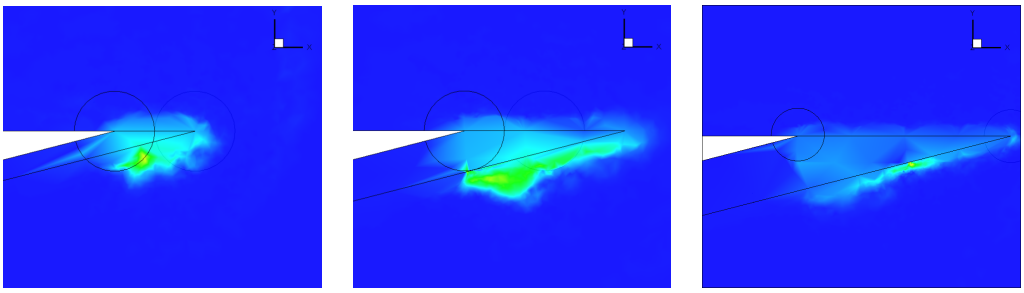

Figure 5.26: Vorticity magnitude plots at the discontinuity at 10μs

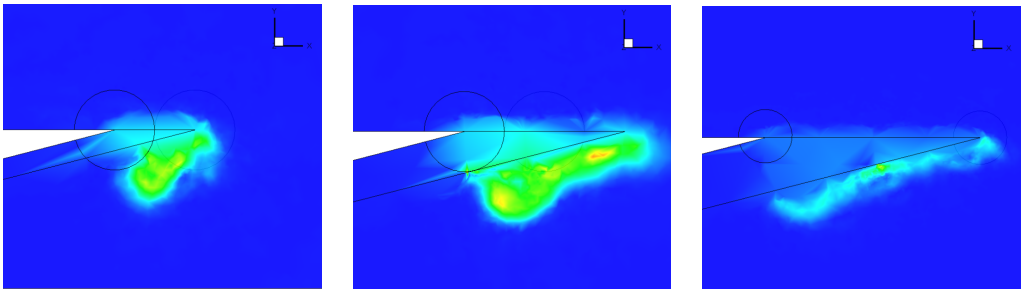

Figure 5.27: Vorticity magnitude plots at the discontinuity at 27μs

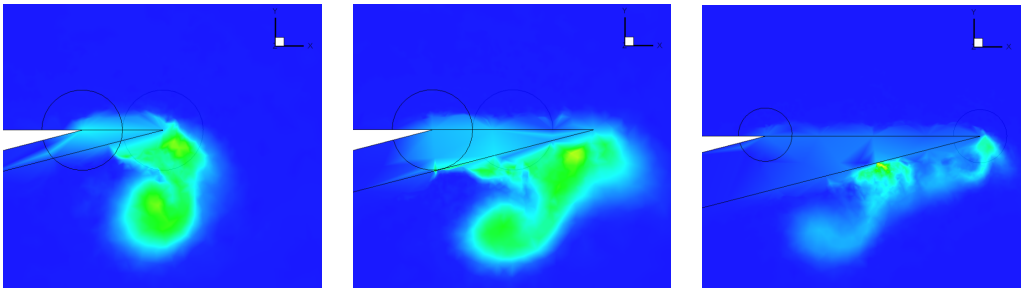

Figure 5.28: Vorticity magnitude plots at the discontinuity at 65μs

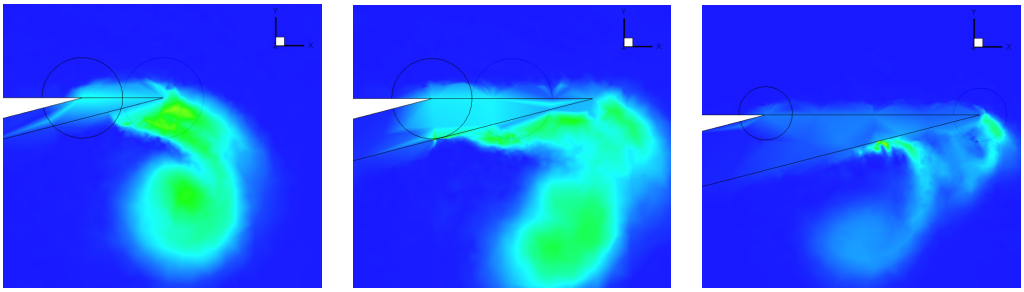

Figure 5.29: Vorticity magnitude plots at the discontinuity at 109μs

Throughout the flow regime there is some vorticity along the offset edge length. This result is expected as the vortex shed off the upstream edge ends at the viewing window and the offset edge length. This is clearly demonstrated in figure 5.26 since at this time the shock is yet to diffract over the downstream edge.

The peak vorticity seems to occur at a time of 27μs. Distinguishing at what point the maximum vorticity occurs is challenging, since the colour schemes are similar across all the models. For the 10mm model, figure 5.27 shows dots of yellow which are not present in any other image. A similar argument can be made for the 5mm edge, although there does not seem to be any yellow in figure 5.27. That being said, the vorticity magnitude reaches a peak at some point in time and afterwards begins to drop. The vorticity magnitude is lower at the same time for a larger offset edge length; which combined with the dropping of vorticity magnitude with time is an indication of the vortices expanding at a quicker rate for a larger discontinuity.

The shape and spread of the vorticity plots changes with time. In the initial stages the vorticity plots are close to the diffraction edge. With time the vortices shift down and to the right; similar to the experimental images. Early on in the flow; the vorticity is stretched along the offset edge length. Naturally for a larger offset edge length the more stretched the vorticity plots are. At time 109μs the vorticity plots resemble shapes which have some similarity to uniform vortices.

The 5mm model shows a smooth shape. The vortex formed of the upstream edge can be seen clearly. Given that the offset edge length is small, the vortex from the downstream edge follows the curvature of the vortex shed of the upstream edge. As the size of the discontinuity increases; the shape of the vorticity becomes more distorted, as can be seen from the 10mm model. In the case of the 20mm; the discontinuity is so large that the vortex shed of the upstream edge is attached to the offset edge length and/or the underside of the downstream edge. There is a distinction between the flow of the upstream and downstream edges. The vorticity is the highest for the flow immediately around the diffraction edges. The shape is close to resembling two independent vortices. In a manner of speaking the vorticity plots for the 5mm and 20mm models form recognizable shapes.

Further insights about the behaviour of the flow about the offset edge lengths are obtained from analysing slices along the X and Y planes.

In order to take slices along the flow, the time frame has to be kept constant. A time of 53μs (5mm), 47μs (10mm) and 55μs (20mm) were used. This portion of the flow was interesting as the vortices are significantly developed; the upstream

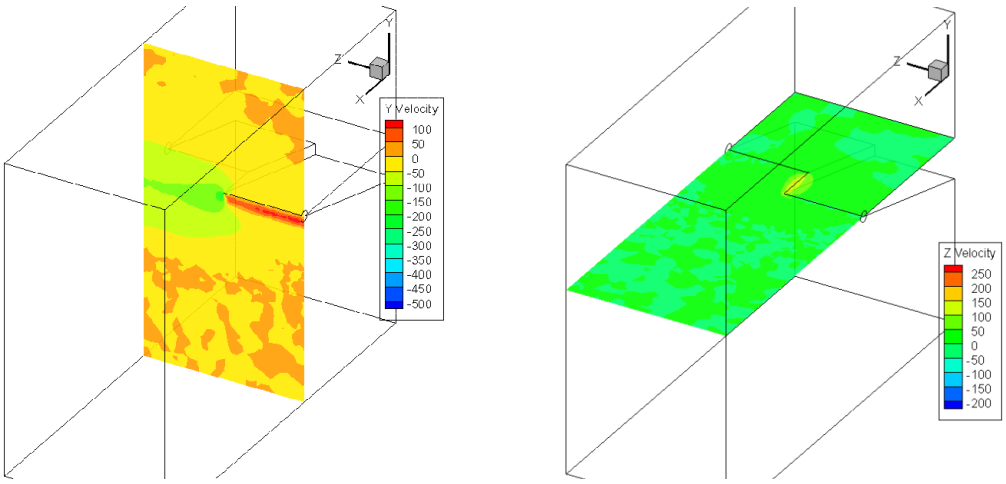

Figure 5.30: Slices of Y velocity along the X plane (left) and slices of Z velocity along the Y plane (right)

and downstream vortices have amalgamated for the 5mm and 10 mm models, while independent vortices are apparent for the 20mm model (figure 5.7).

Slices were taken along the X plane; the starting position was at the downstream edge and the ending position was the upstream edge. The positions are numbered numerically, i.e. one at the downstream edge and five at the upstream edge. Given the sizes of the various offsets; the difference in sizes between the positions of the slices increased as the offset increased. The slices taken, cover the length of the offset. The distance between each slice is evenly spaced; 5mm for the 20mm model, 2.5mm for the 10mm model and 1.25mm for the 5mm model.

In figure 5.31, the up and downstream edges are on the left and right respectively. The generalized colour backgrounds changes amongst the different models. The velocity is the highest for the 5 mm model. As the discontinuity increases in size, the velocity of the vortex shed of the upstream edge drops. In the case of the 20mm model, the direction changes (based on the colour scheme and the corresponding scale).

Positions 1 and 5 correspond to the X plane being located at the down and upstream edges respectively, as a result only these two positions can be compared directly across all three models. Position 5 only shows flow from the upstream edge. Position 1 highlights the interaction of the vortices shed of the up and downstream edges. The interaction is the strongest for the 5mm model and significantly weakens by the 20mm model.

In terms of position along the X axis, different sections from the vortices shed of

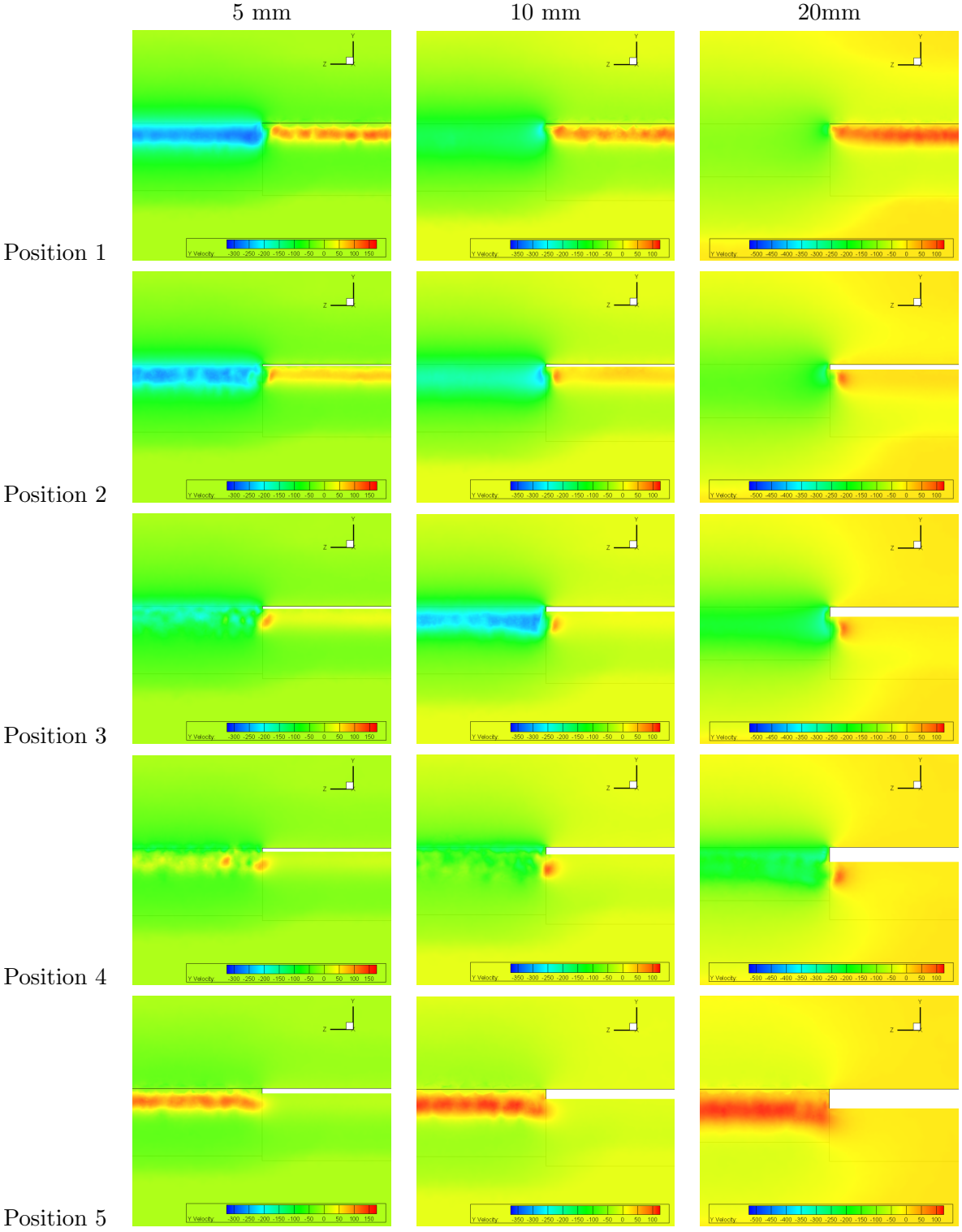

Figure 5.31: Y velocity contours in the X plane taken along the offset edge length at a time of $\pm$ 53μs

the up and downstream edges can be seen. The general trend amongst all three models is at position 1, the vortex shed of the downstream edge can be seen, but it diminishes as one goes through the various positions. Naturally the inverse occurs

for the upstream vortex. The shock diffracts of the upstream edge before the downstream edge, as a result the upstream vortex is larger and more developed then the downstream vortex, which is confirmed by the experimental images (figure 5.3).

A vortex has a circular structure, therefore at opposite ends of a diameter; the direction of velocity will be in opposite directions. This feature is demonstrated by the 5 mm model in positions 1 and 5, and positions 3 and 5 for the 10mm model. There are more positions between the velocities travelling in different directions for the 5mm model in comparison to the 10mm model, simply because the gaps between the positions are larger for the 10mm model then the 5mm model. Similarly for the 20mm model, where the gaps are so large a concentrated (region where the velocity contours are focused) portion of the velocity is not seen except at position 5.

An interesting feature is when the discontinuity increases in size, a larger portion of the upstream vortex is attached to the underside of the model. At a time of $\pm$ 53μs the downstream vortex has formed (figure 5.7). The downstream vortex is situated away from the downstream edge due to the shear layer. What is viewed from positions 1 to 5, on the downstream edge, is a portion of the downstream vortex. The downstream vortex is the largest in terms of magnitude and concentration for the 20mm model (position 1). The implication is that as the offset edge length increases in size, firstly the vortices behave more independently and secondly, the offset edge length has less effect on the structure of the up and downstream vortices, away from the discontinuity. Adjacent to the offset edge length, there is a change in shape of the structure (figure 5.18 to 5.21).

Contours of Z velocity are analysed and presented in the same manner as the Y velocity contours. Position 1 in figure 5.32 is where the upstream and downstream edges are flush; as in the plane of visualisation. Whereas position 5 is beneath (has a lower value of the y coordinate) position 1 and is judged based on the Z velocity contours that can be seen and whether any insight can be gained from the images. The distance between the slices for the 20mm, 10mm, and 5mm models are $\pm$ 25mm, 25mm, and 12.5mm respectively. In figure 5.32 the downstream edge is on the left and the upstream edge is on the right.

Position 1 demonstrates what has already been established and that which can intuitively be implied; the larger the discontinuity, the more stretched the Z velocity contours. The size and shape of the contours are larger for a larger offset, as can be seen from positions 1 to 5. The 5mm model has the most contours of an orange/red colour, whereas the 20mm model has the most contours which are blue. Given the scale and colour scheme, this stipulates the colour change of the contours from a

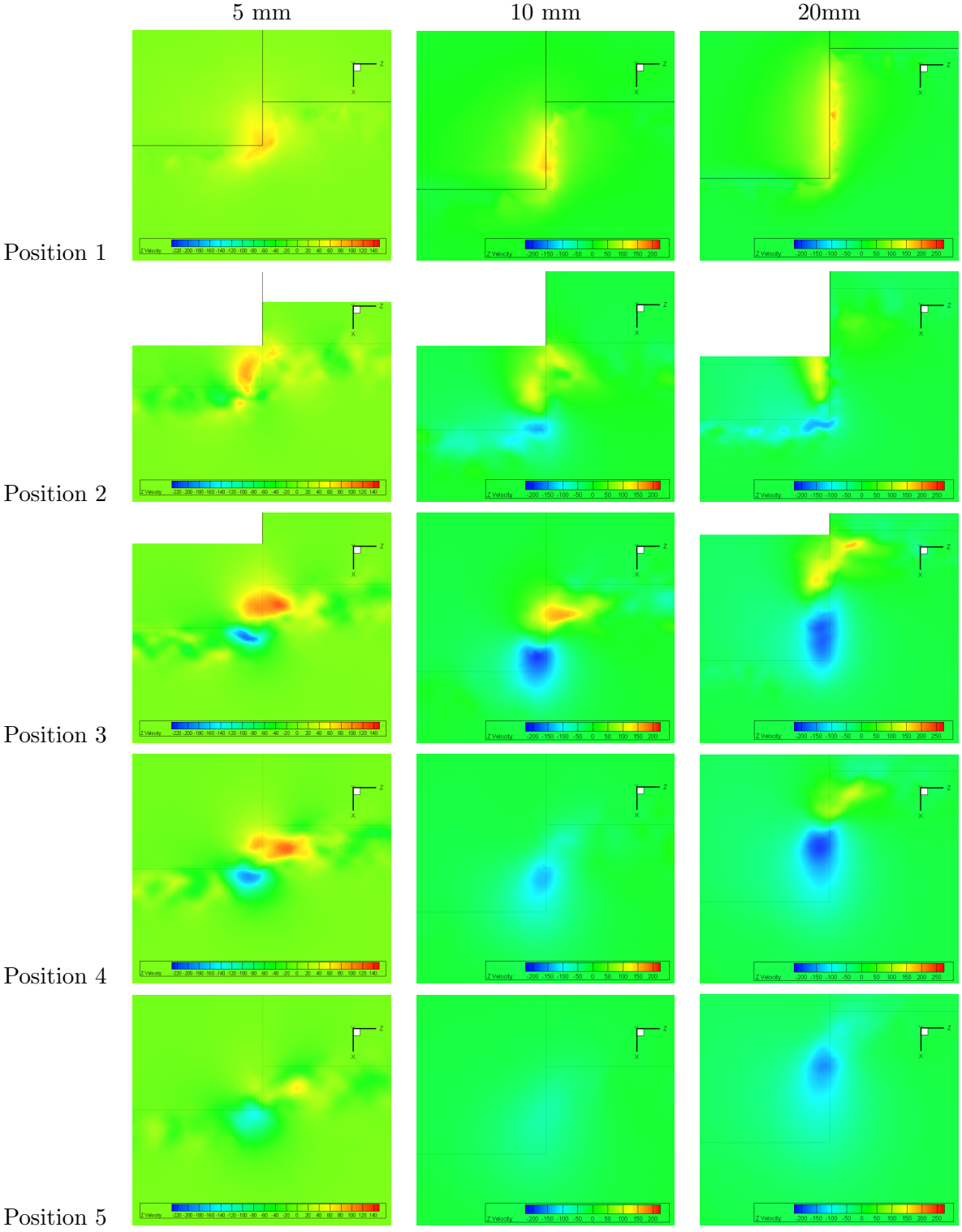

Figure 5.32: Z velocity contours in the Y plane taken along the offset edge length at a time of $\pm$ 53μs

small to a large offset is an indication of the change in direction along the Z axis of the Z velocity for different sized offset edge lengths.

The slices taken; effectively span the size of the model in the y direction. From the contours on these slices; the majority of the flow is focused around the discontinuity. This observation provides further evidence that the discontinuity affects the flow about itself and along the up and downstream edges, but only adjacent to the offset edge length.

Between all three models, the largest contours occur at either position 3 or 4. These positions are in close proximity to the underside of the model. Figures 5.18 to 5.21 show that the isosurfaces of density of the upstream edge curve downwards at the discontinuity before joining with the isosurfaces from the downstream edge. A combination of the above two characteristics show that a major change to the flow features occurs near the underside of the model. In addition the isosurfaces of density also show a more complex shape about the discontinuity as the offset edge length increases in size. This is complimented by the increasing size of the Z velocity contours for larger offsets, as it is an indication of changes in direction and magnitude of velocity at a given position.

5.2.3 Diffracted Shock Wave

The experimental images provide a good visual interpretation of the shape of the diffracted shock wave in a two dimensional sense. From the experimental images (figures 5.2 to 5.13) it can be seen that there is one shock wave that has diffracted at different points in time as a result of the offset edge length. Half of the shock wave (half the width of the shock wave) has diffracted over the upstream edge, while the remaining half has diffracted over the downstream edge.

The offset edge length has an impact on the portions of the shock wave diffracted of the up and downstream edges. The shock initially diffracts of the upstream edge and thereafter the downstream edge, therefore there is a distance between those two portions of the diffracted shock wave. When the size of the discontinuity increases, so does the distance between the portions of the shock wave diffracted over the up and downstream edges. On the other hand, as the flow progresses with time the distance between the various parts of the diffracted shock wave remain more or less constant, for each specific model.

Given that it is one shock wave that has diffracted, there is a connection between the two portions of the diffracted shock wave. Figure 5.5 show that the portions of diffracted shock wave are connected seamlessly for the 5mm and 10mm models. With the 20mm model the point of connection is further along the diffracted shock

wave, in terms of height. As a result the portion of the shock wave diffracted over the downstream edge curves beyond the portion of the diffracted shock wave of the upstream edge, indicating a second point of connection and hence a complex shape of the diffracted shock wave.

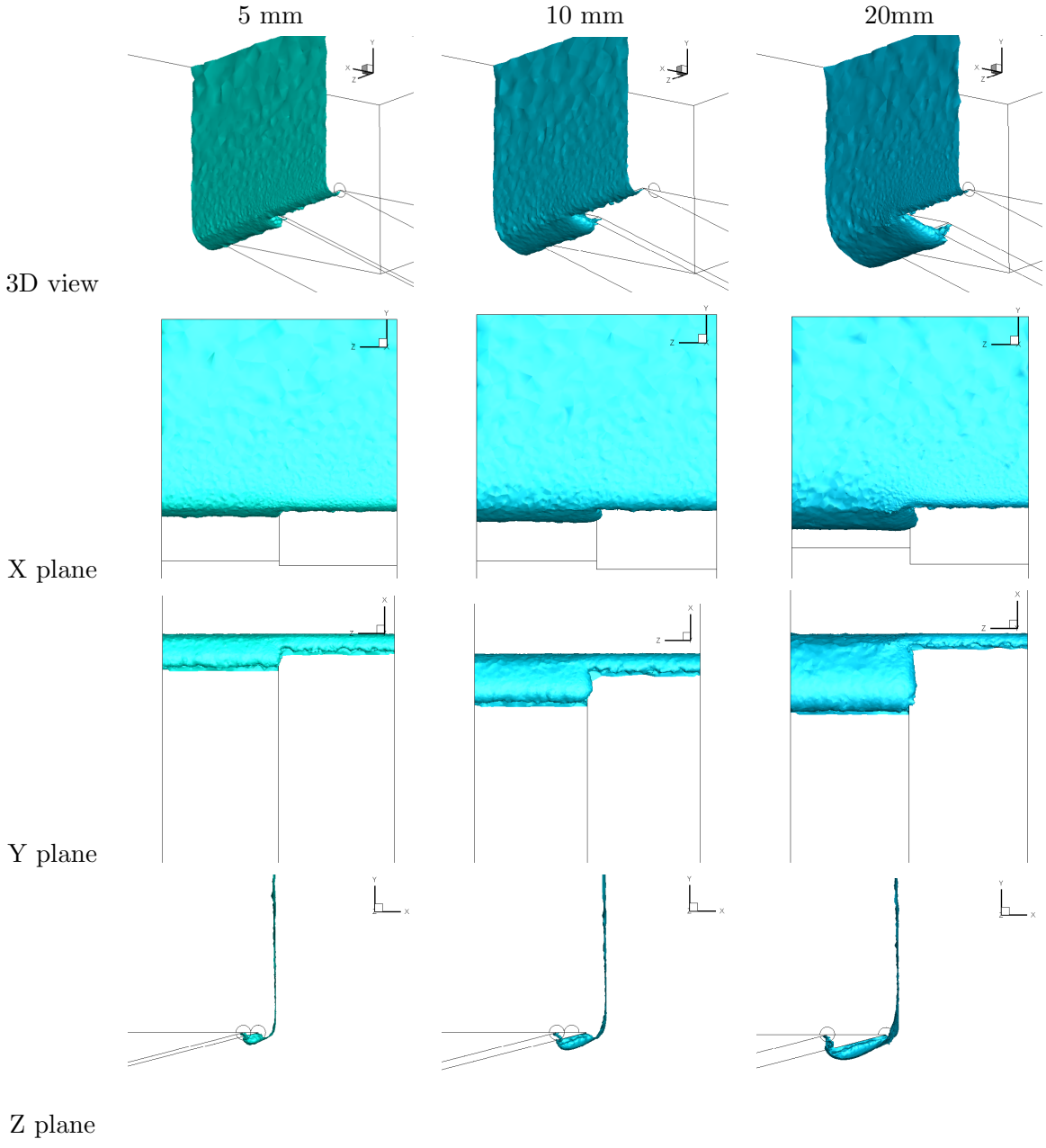

Figure 5.33: Velocity magnitude isosurfaces at a time of ± 10μs at Mach 1.32

The isosurfaces of velocity magnitude (figure 5.33 - 3D View) demonstrate the complexity of the diffracted shock wave as hinted at in the experimental images. As the offset edge length increases in size, the diffracted shock wave becomes increasingly distorted about the discontinuity. Relative to the size of the discontinuity, there is a small change in the diffracted shock wave from 5mm to 10mm; except for the

larger size of the portion of the shock wave diffracted of the upstream edge. This observation is backed up by the consistency shown between the models in the X and Y planes. The major change, as has been the case throughout this chapter occurs with the 20mm offset edge length.

The X plane shows that the discontinuity is so large with the 20mm offset, that the portion of the diffracted shock from the upstream edge curves underneath the discontinuity. The same feature is seen once again in the Y plane, but with more clarity. The above discussion is an indication that the free vortices as well as the diffracted shock wave are affected by the offset edge length.

The Z plane shows that the diffracted shock of the 10mm and 20mm models are similar in terms of shape, but not size. The 5mm model has more depth on the curved portion of the diffracted shock, in comparison to the remaining models. A possible explanation is that the up and downstream edges are so close together that there is a strong interaction between the two portions of the diffracted shock wave, as in the case with the free vortices.

5.3 Quantitative Results

The plots of isosurfaces have provided detailed insight into the behaviour and topology of the vortex structure. In order to gain more in depth knowledge, the data will be quantified. Quantifying results enables values to be associated to the images (isosurfaces and contours).

In figure 5.35 there are a series of points taken along the y axis (black line in figure 5.34) on the Z plane; exactly at the offset edge length. The time is common, 54μs, unless states otherwise. The data for the 5 and 10mm models is along the y line (a line upon which data is extracted from in the y axis); however the data for the 20mm model is obtained from a different y line (shifted along the x axis). The distance to which the y line is shifted is small, but the value itself arbitrary. The plot of tangential velocity (figure 5.36) shows that even a slight shift of the line which is used to extract data caused the spread of the data to be inverted. Therefore one has to be careful when making inferences or drawing conclusions from these plots.

The contours of density as well as the isosurfaces show that the vortex is not circular at the offset edge length, as it was for the up and downstream edges (in close proximity to the walls of the fluid domain). Despite the difference in shape the tangential velocity changes direction within the vortex structure. This could be the

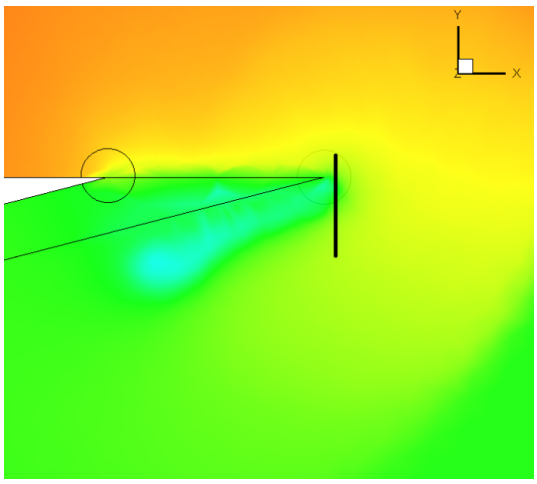

Figure 5.34: Contour of density for the 20mm model at a time of 54μs indicating where the y line was taken in order to extract the data

reason as to why the tangential velocity profile is inverted for the 20mm model. The profile for the 5 and 10mm models show that there is a change in direction along the y line. The tangential velocity is negative up to ± 0.072m for the 10mm model and ± 0.074m for the 5mm model. From the respective values to a distance of 0.08m, the values are positive and are thereafter negative. The tangential velocity is zero at two distances along the y line for the 5 and 10mm offsets. With the work done by Reeves (2010), he found that the vortex core occurred where there was a trough in the tangential velocity profile and at zero tangential velocity. The trough being the position of the vortex core was originally mentioned by Lee & Bershader (1994), but it is not necessarily at zero tangential velocity. Following the same criteria; the cores for the 5 and 10mm models occur at ± 0.082m and at 0.085m for the 20mm model. The corresponding axial velocities (figure 5.38) pass through zero and thereafter sharply increase. This holds true for all models. A similar pattern is observed with radial velocity (figure 5.37); however in the case of the 20mm model the velocity does not pass through zero. The trend for the 20mm offset for the radial and axial velocities are different in comparison to the remaining models. The negative axial velocity of -150m/s is significantly more (as the negative is an indication of direction) than 100m/s (largest axial velocity for the 5 and 10mm offsets). This is a clear indication of the variation of the different parameters at different sections of the flow.

The behaviour of the vortex about the discontinuity is complex. According to Hall (1965) on his work on three dimensional vortices, there would be large axial and tangential velocities. However this is not the case with the current study, as the maximum magnitudes are of 150m/s and 240m/s respectively; which are smaller

than the values seen in Reeves (2010) work; 400m/s.

The plot of vorticity magnitude (figure 5.35) indicates that the maximum vorticity occurs at or about the vortex core. There is unusual spike in the vorticity of the 10mm offset; it is unusual in the sense that it is exponentially larger than any of the values from either the 5 or 20mm models. That particular spike could be as a result of the distribution of data along the 10mm offset as a function of geometry, in comparison to the 5 and 20mm offsets.

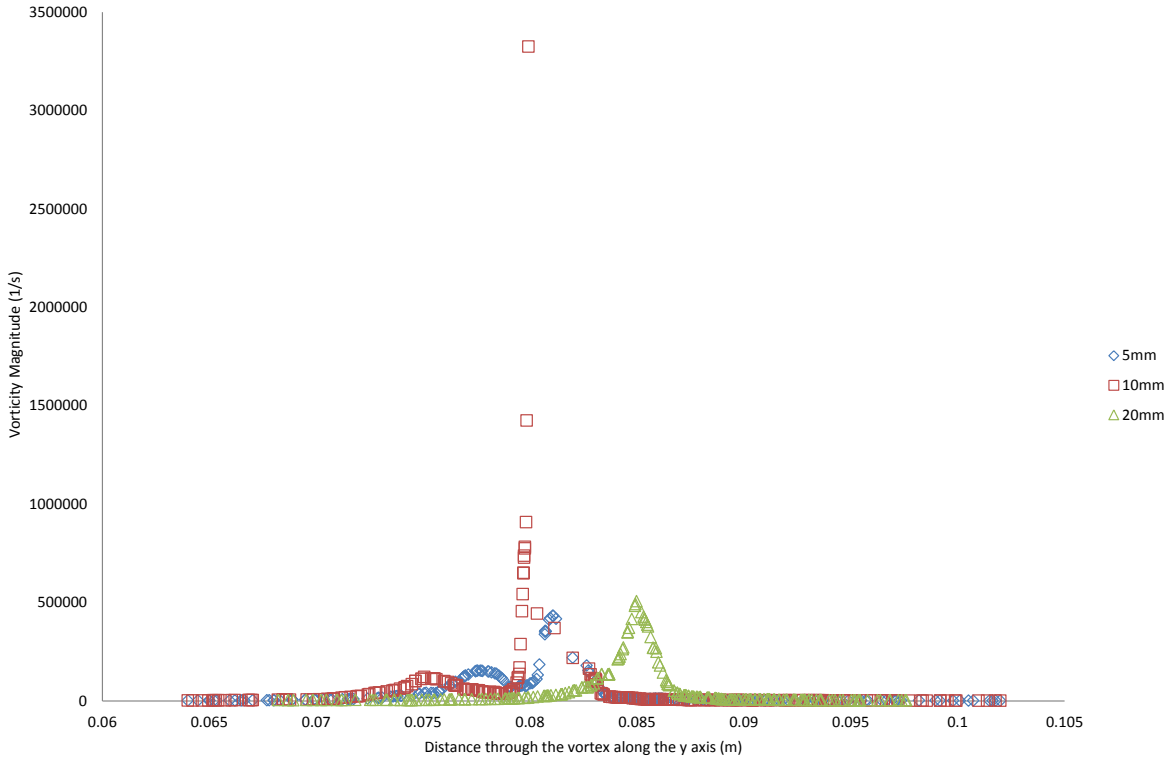

Figure 5.35: Variation of vorticity magnitude at the offset edge length along the y axis in the Z plane

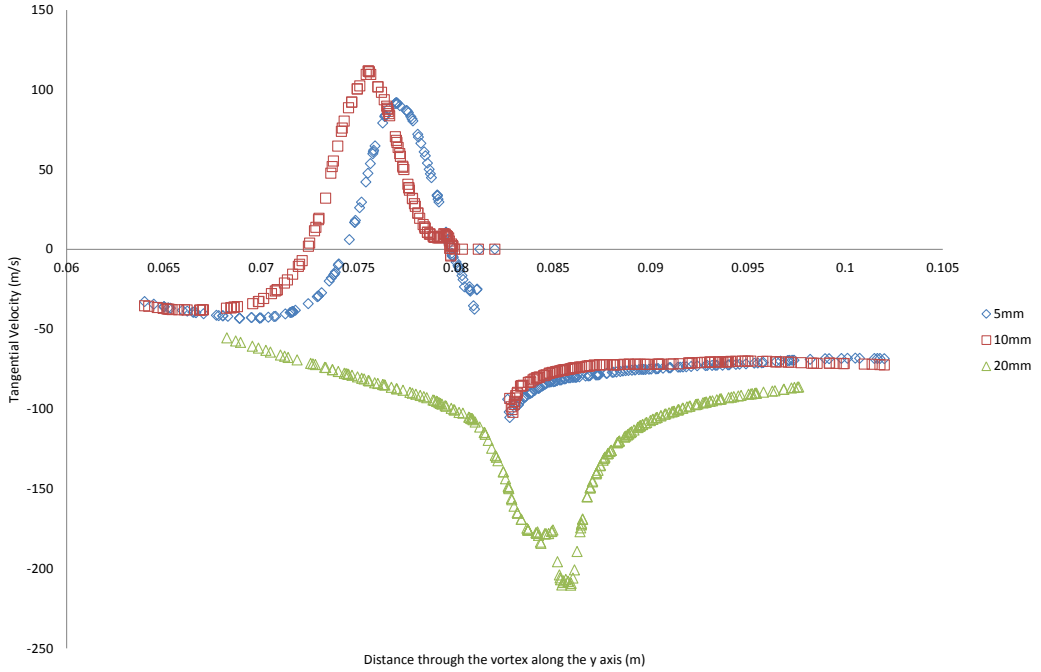

Figure 5.36: Variation of tangential velocity at the offset edge length along the y axis in the Z plane

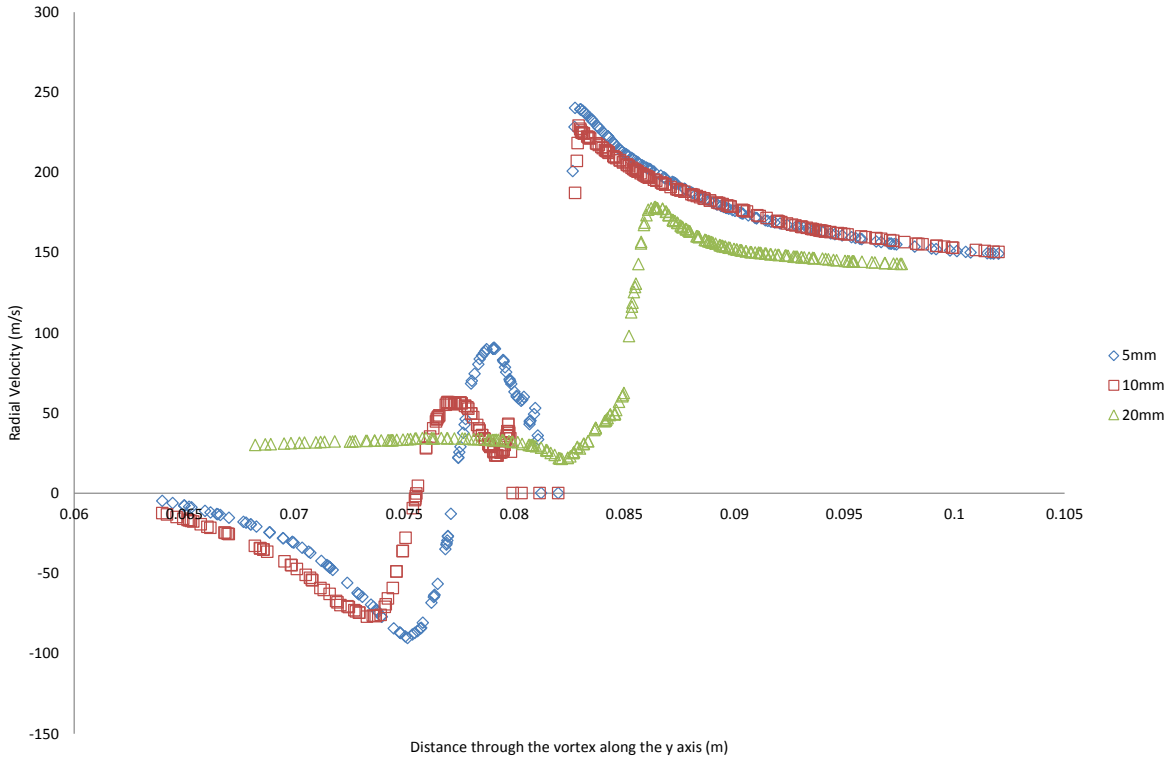

Figure 5.37: Variation of radial velocity at the offset edge length along the y axis in the Z plane

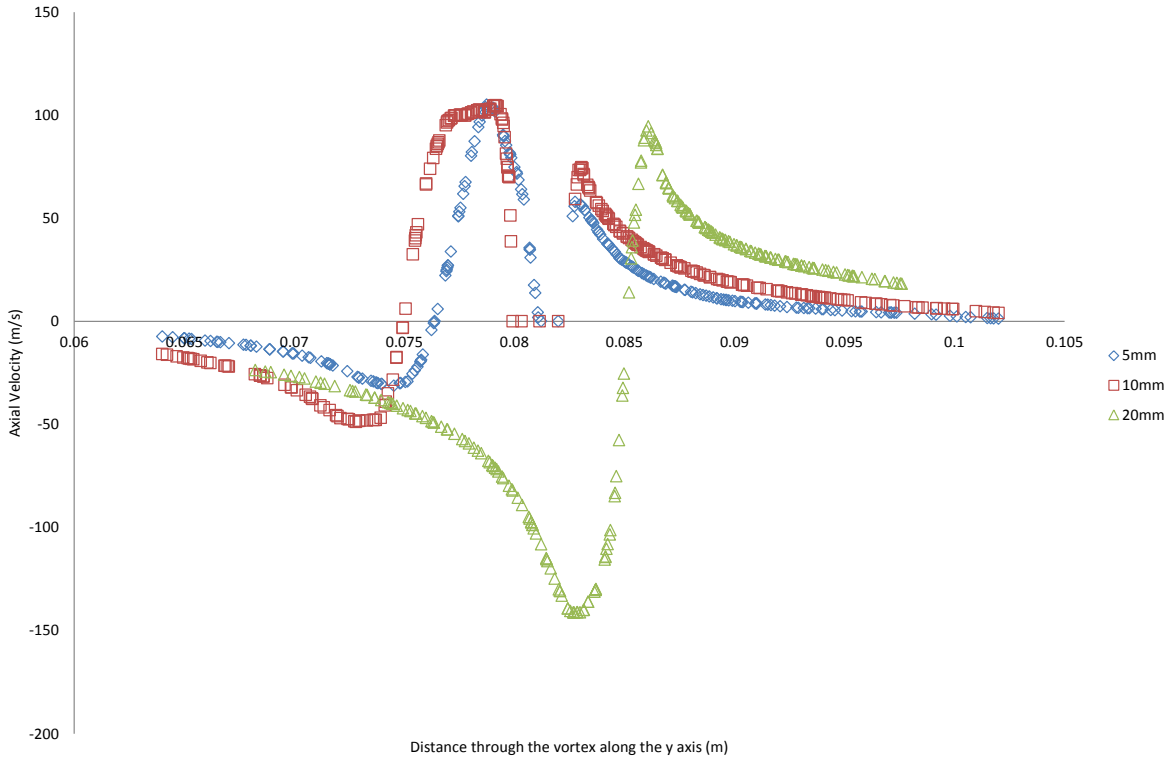

Figure 5.38: Variation of axial velocity at the offset edge length along the y axis in the Z plane

The flow was analysed in the X plane; with a z line taken through the X plane (figure 5.39). The contours in figures in figures 5.34 and 5.39 are of density and illustrate where the data line has been taken.

The plot of vorticity magnitude (figure 5.40) shows that there is a spike in the vorticity magnitude, for the 5 and 10mm models around ± 0.007m. The negative distance values along the z line refer to the upstream edge and positive values to the downstream edge. Therefore the peak vorticity does not occur exactly at the discontinuity, but adjacent to it on the downstream edge. Observing the isosurfaces of density; the flow pattern around the density is complex. There is a lot of twisting and bending occurring, however the same basic pattern and shape is followed for all three models. The fundamental difference is the change in size. Something similar is observed with the vorticity plot (figure 5.40). Accounting for the complexity of the flow, particularly around the offset edge; it is not surprising that the peak vorticity occurs adjacent to the offset.

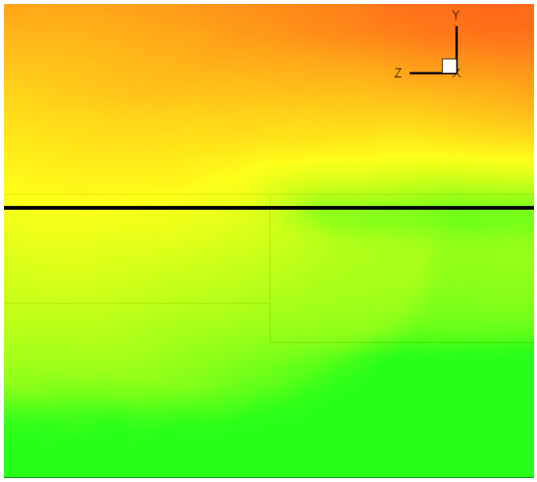

Figure 5.39: Contour of density in the X plane for the 20mm model at a time of 54μs indicating where the z line was taken in order to extract the data

When comparing the 5mm model to the 10mm one, the vorticity magnitudes on the upstream edge are comparable in terms of the peak values. The major discrepancy occurs on the downstream edge, where the values for the 10mm model are significantly lower. It may be the case that at that particular slice in the fluid domain, the flow over the 5mm model is more developed than the 10mm model.

A far more extreme case is observed with the 20mm model. There is little vorticity across the entire z line for this model. It is likely that at this space and time the flow is not developed. The gap between the up and downstream edges might be large enough for the flow over the upstream edge to have been developed but not to be picked up by this slice.

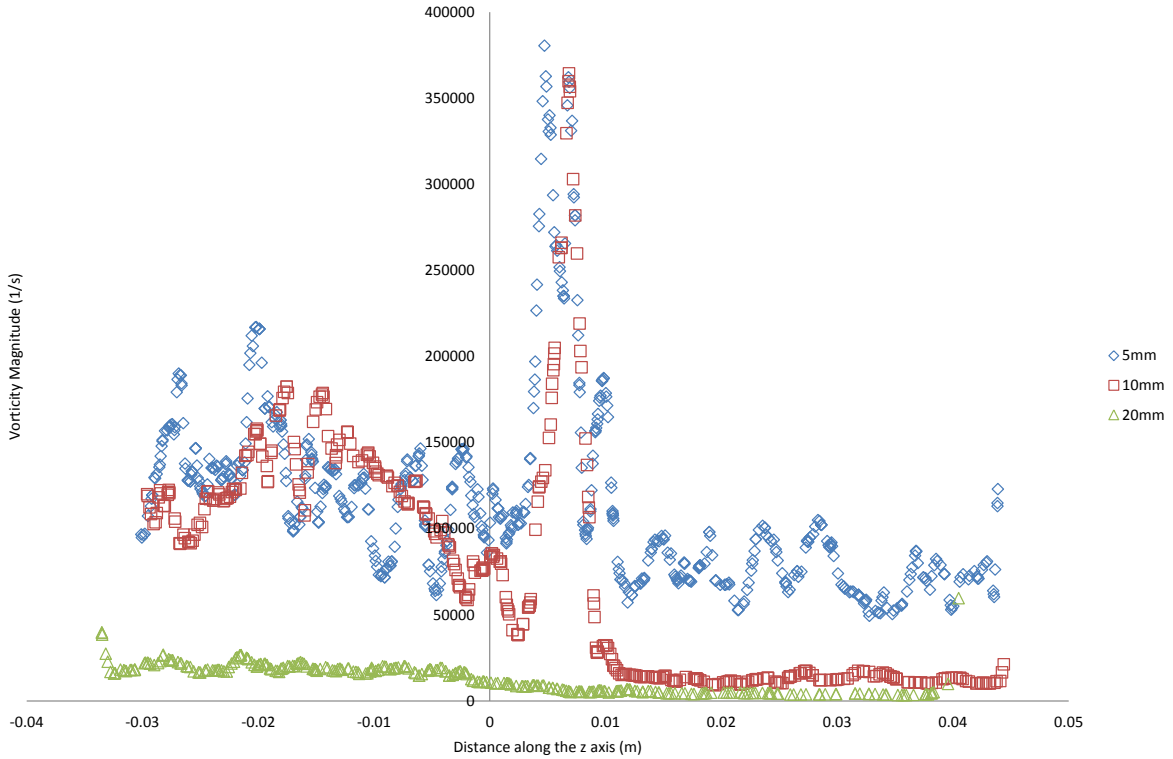

Figure 5.40: Variation of vorticity magnitude at the offset edge length along the z axis in the X plane

In order to investigate this phenomenon further; a slice was taken of the 20mm model in the same space but at a different time. Figure 5.41 shows that at a later time instant; the distribution of vorticity magnitude along the z line is analogous to the 5 and 10mm models (figure 5.40). The peak values of vorticity are higher for the 20mm offset at a later time (71μs). This suggests one of two things, firstly that if a different slice was picked, then the distribution for the 20mm model at 54μs would be similar to the 5 and 10mm models. The second inference is that as time progresses the vortex develops, in the sense that more in-depth data is obtained from the same slice but at a later time.

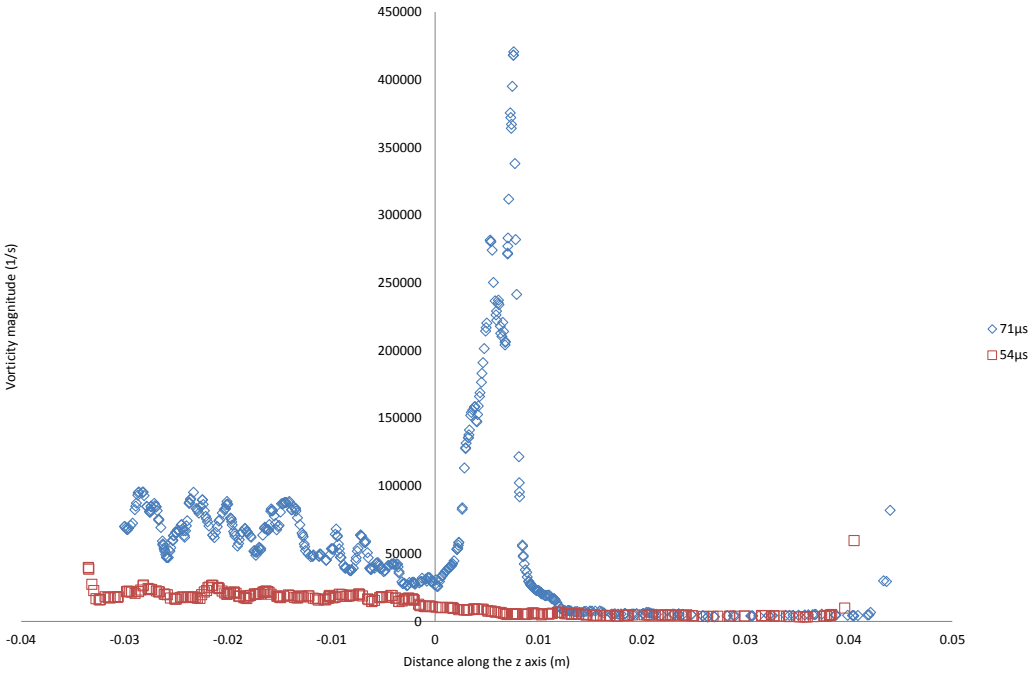

Figure 5.41: Variation of vorticity magnitude at the offset edge length along the z axis in the X plane at different time instances

The density distribution shows a similar trend with regards to a change in the shape of distribution over time. In the case with vortex flows; the minimum density values occur at the vortex core. Comparing figures 5.40 and 5.42, the minimum density and maximum vorticity occur in a similar place, which is a strong indication that for this specific model, time, slice and line from which the data was extracted that the vortex core is located adjacent to the offset along the downstream edge.

In the density plot, at a time of 71μs, the density decreases along the upstream edge

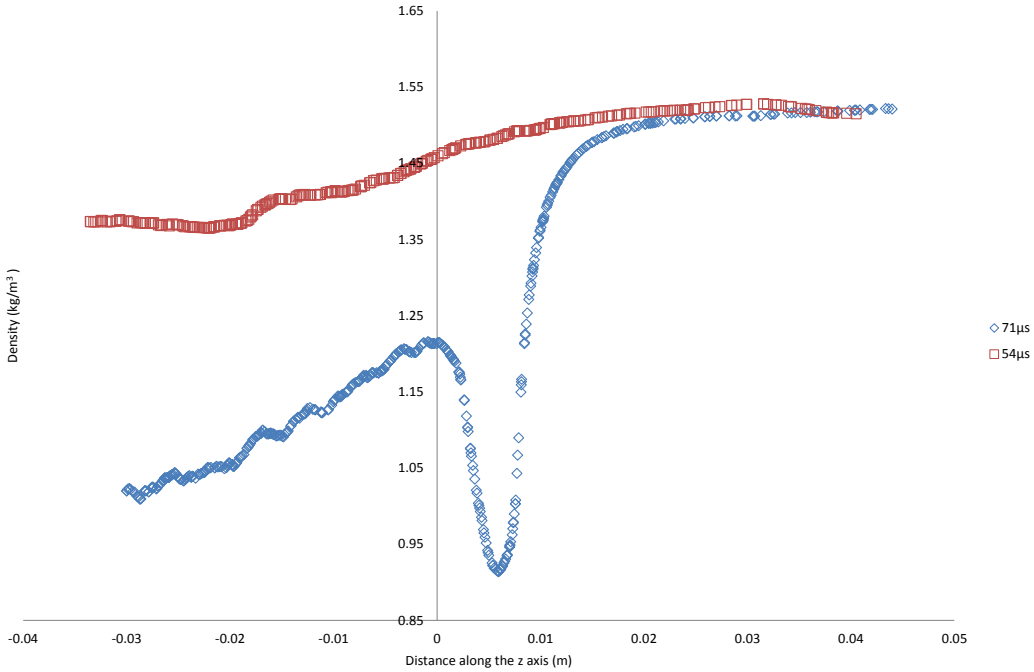

Figure 5.42: Variation of density at the offset edge length along the z axis in the X plane at different time instances

as one heads towards a wall of the fluid domain (the values start at 0 and head towards -0.03m). The decrease is a general linear trend from the discontinuity, with the odd kinks (i.e. it is not a perfect linear trend, as expected). This points to what has already been established; a complex flow field with strong three dimensional effects. Therefore it is difficult to describe in words and next to impossible to model with mathematical equations.

Analysing density in the Z plane, along a y line; as was the case with vorticity magnitude, axial, tangential and radial velocities (figures 5.35, 5.36, 5.37 and 5.38), shows that there is a density drop at a given space, however the value of density at that those points is large (figures 5.42 and 5.44). From previous discussions on tangential velocities and the work done by both Reeves (2010) and Lee & Bershader (1994), the vortex core occurs where there is a trough in the tangential velocity and is defined as having a constant circulation. Comparing the contours of density (figures 5.34 and 5.43) to the density plot (figure 5.44), the value of density at the trough ($\pm$ 1.05kg/m^3) is not equivalent to the minimum density of the contour; which is approximately 0.5kg/m^3. This implies that the y line taken does not pass

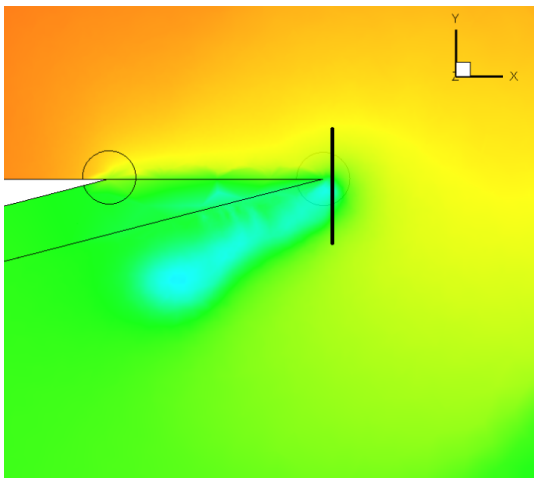

Figure 5.43: Contour of density in the Z plane for the 20mm model at a time of 71μs indicating where the y line was taken in order to extract the data

through any of the dark blue regions of the density contours. The suggestion is that the vortex core does lie on any of the y lines used in analysis to date, even though the plots of tangential velocity may have suggested so. Alternatively it could be the case that the minimum point of density may be the centre of the vortex but not the core of the vortex.

The points where the troughs (for times 54 and 71μs) occur in the density plot correspond to a peak and trough in the tangential velocity plot (figure 5.45). The velocity plots are direction dependant; therefore a peak or a trough could correspond to a maximum or minimum value depending on direction. When comparing the points at which the peak and trough occur (0.057m and 0.083m respectively) to the radial and axial velocities (figures 5.46 and 5.47), the values are zero. It may be an indication of the vortex core or not, but this feature occurs for the same model at different times and y lines and at different models at the same time and different y lines (tangential velocity peak and trough of figure 5.36 and the corresponding zero values of the radial and axial velocities, in most cases [figures 5.37 and 5.38]).

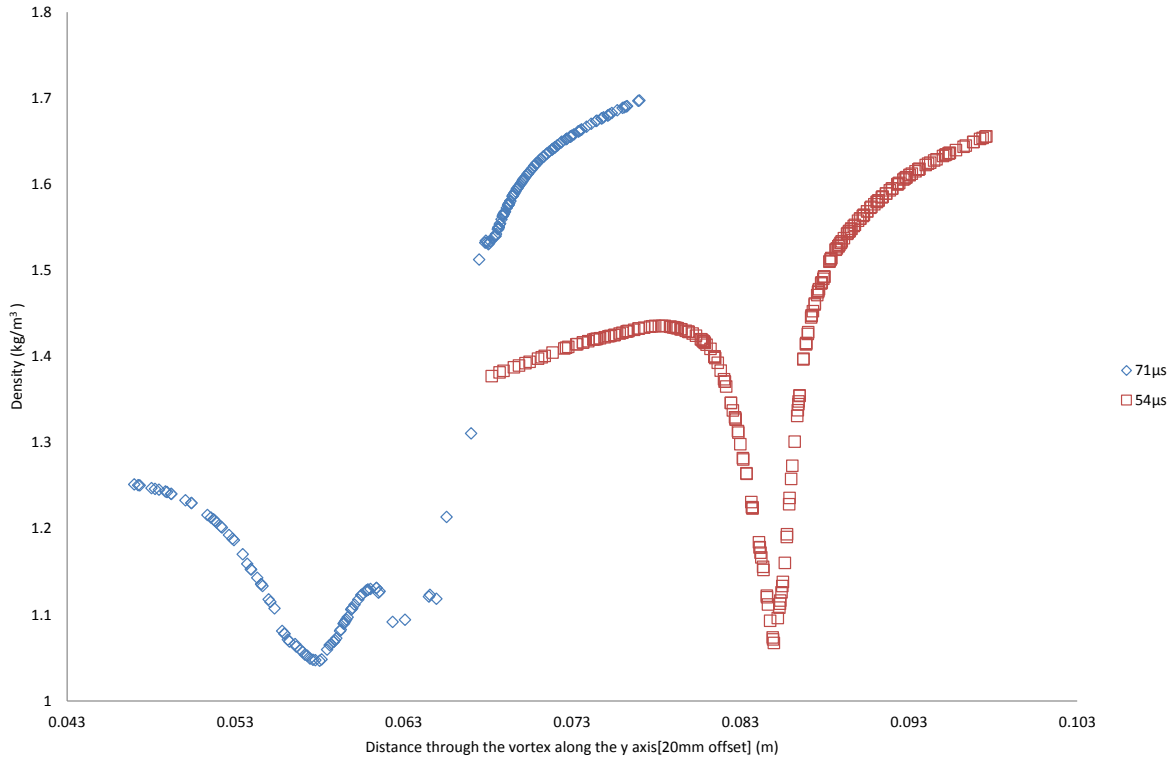

Figure 5.44: Variation of density at the offset edge length along the y axis in the Z plane at different time instances

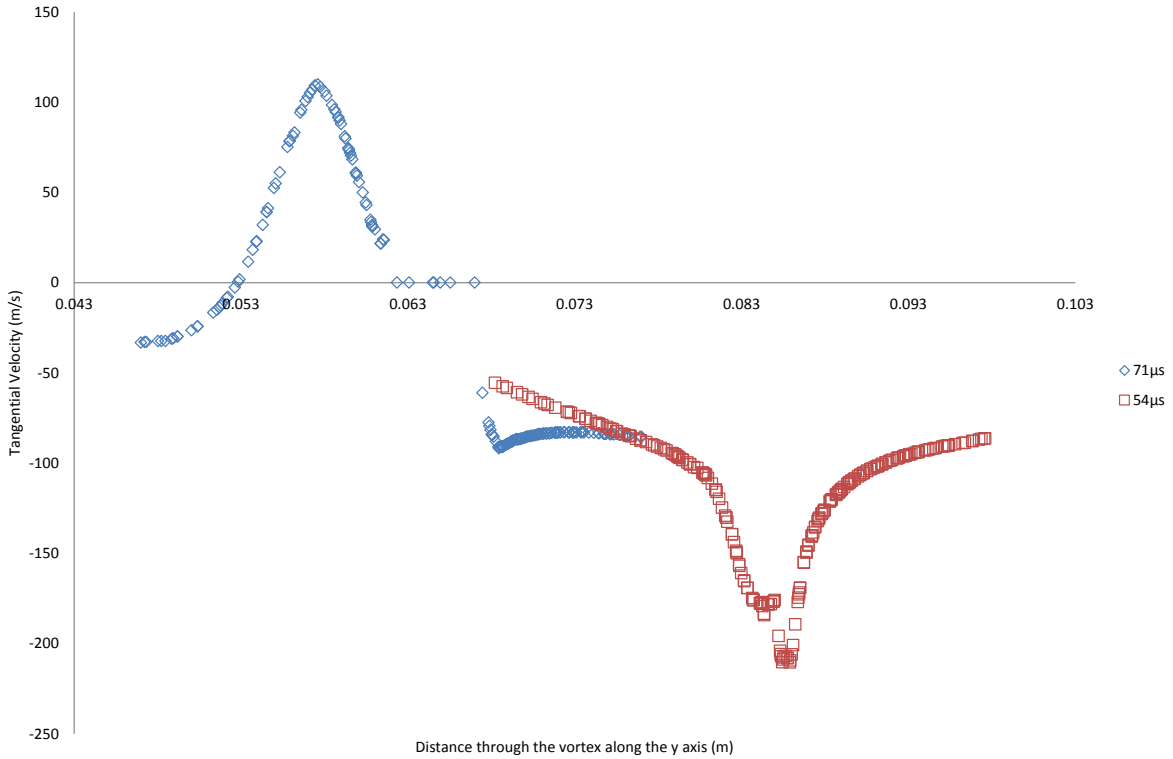

Figure 5.45: Variation of tangential velocity at the offset edge length along the y axis in the Z plane at different time instances

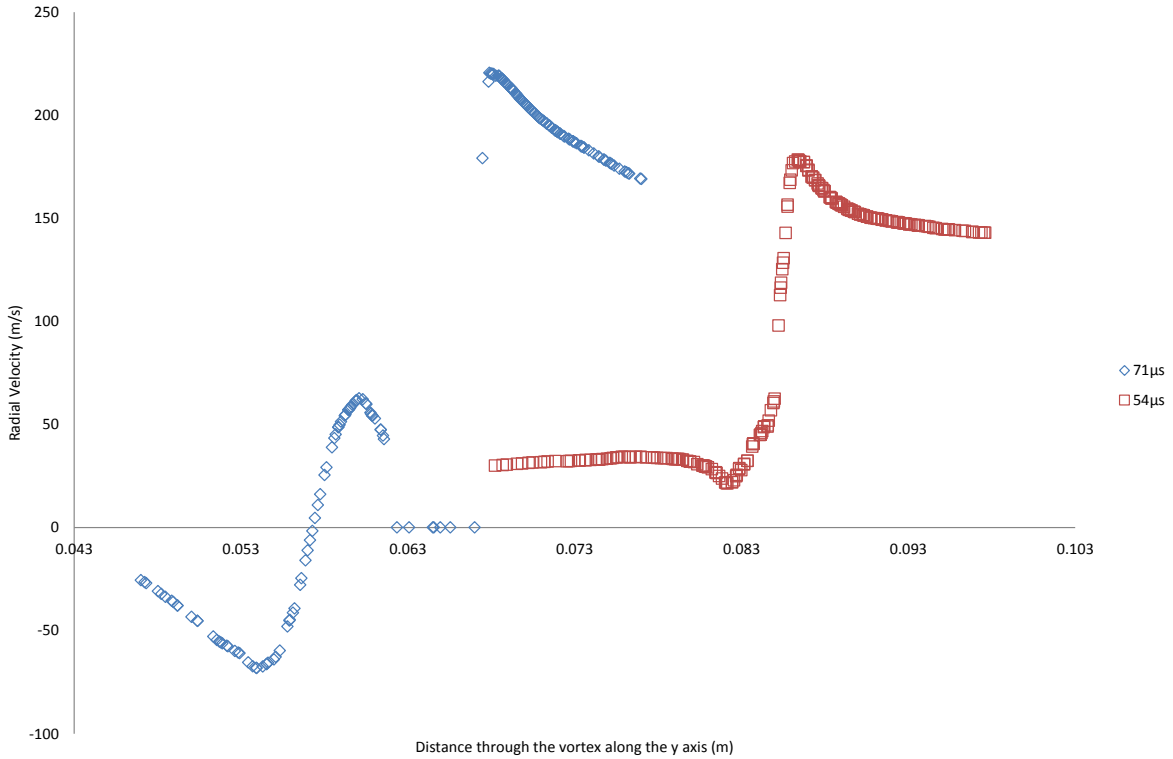

Figure 5.46: Variation of radial velocity at the offset edge length along the y axis in the Z plane at different time instances

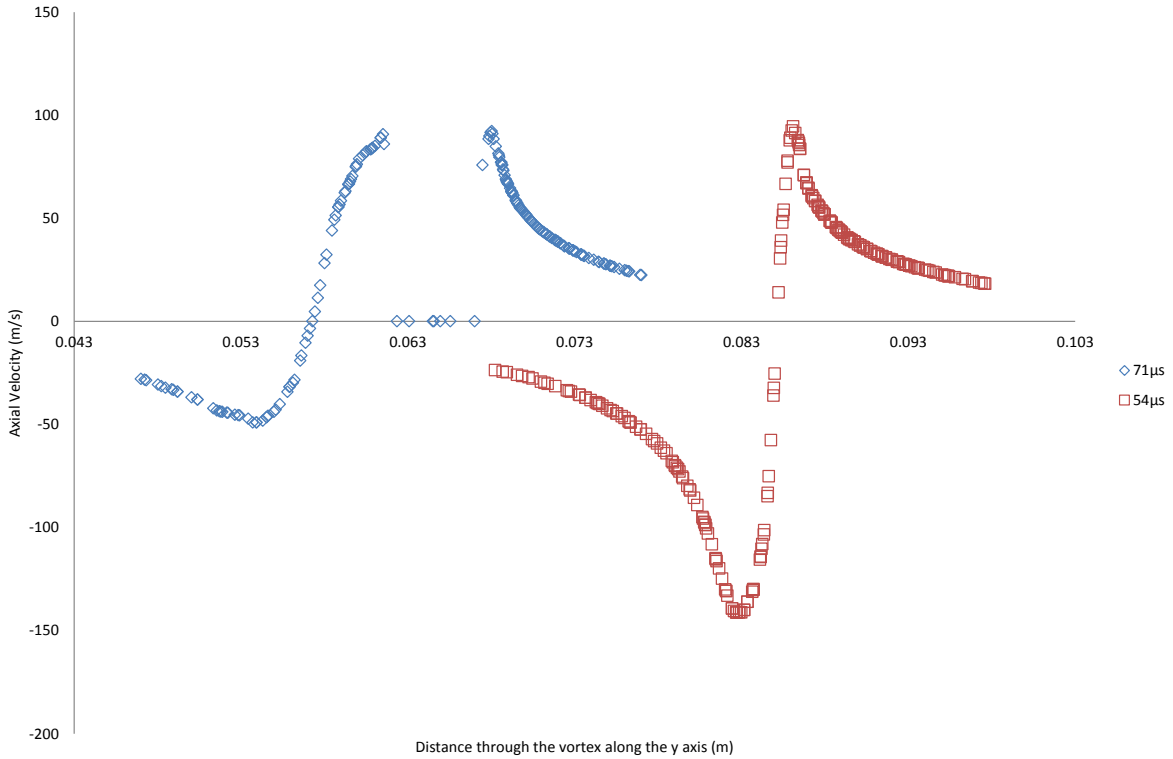

Figure 5.47: Variation of axial velocity at the offset edge length along the y axis in the Z plane at different time instances

An interesting feature that appears around 0.063 and 0.064m is that the velocities drop to zero and the density drops to a value slightly higher than the value of the trough (1.1 kg/m^3) for a time of 71μs. The time difference means the flow is more developed as can be seen from figures 5.34 and 5.43. The density contours along the offset edge length do not have a shape which resembles a free vortex. Instead the shape is a curved structure which follows the underside of the downstream edge. The structure itself, in this case, is defined by the blue contours; as in areas where there are low densities. This structure grows with time and more of it passes through the y line. Since the nature of the structure and the flow itself is difficult to interpret, it is possible that there might be regions where there are density drops in more than one place.

The velocity magnitude contour (figure 5.48) more graphically displays regions where there are likely to drops or low points in comparison to the density contours. That particular feature is demonstrated quite well by the plot of velocity magnitude at 71μs (figure 5.49) in the sense that the behaviour is unpredictable. However it is unusual to see the velocity magnitude pass zero and secondly to have so few data points in the region of 0.063m.

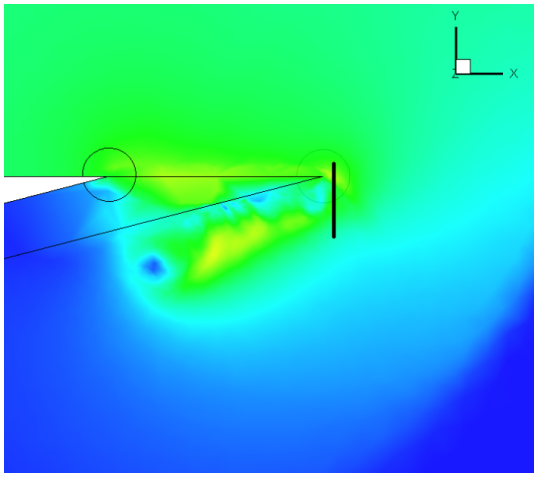

Figure 5.48: Contour of velocity magnitude at the offset edge length along the y axis in the Z plane

These two features; velocity magnitude passing zero and lack of data points are most likely connected. The lack of data points indicates a lack of information and the information is not in keeping with the spread of the data from the y line.

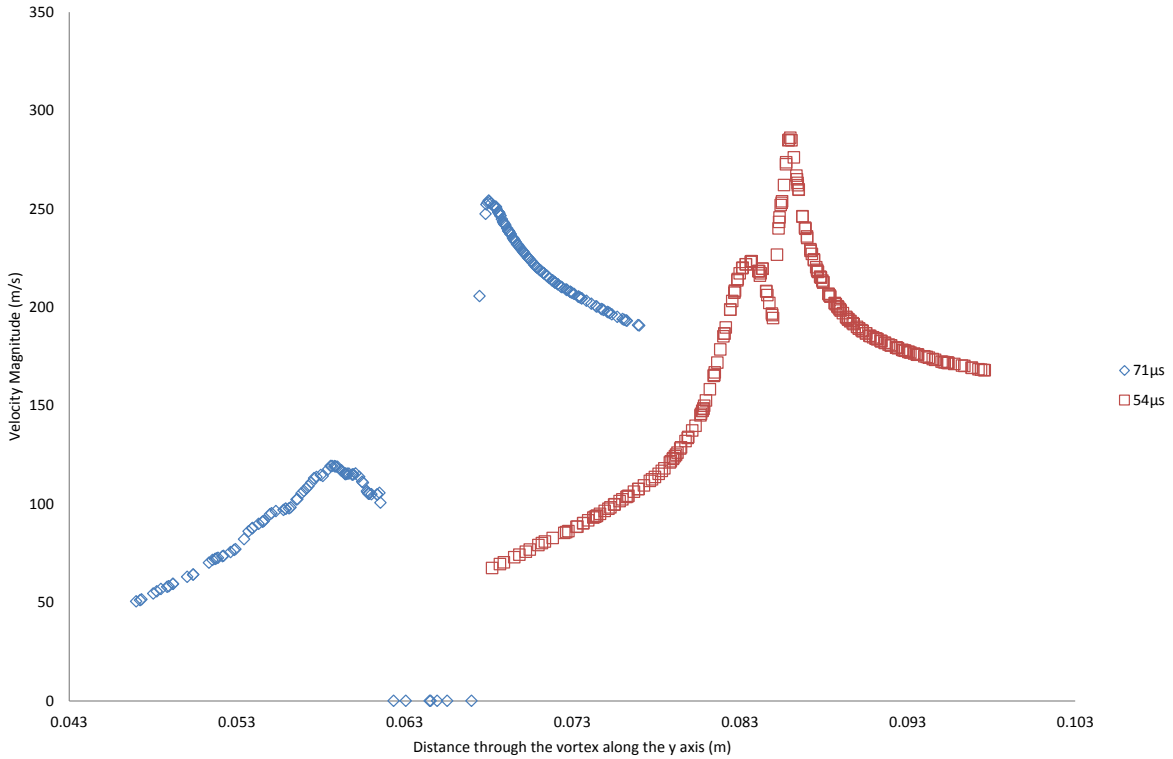

Figure 5.49: Variation of velocity magnitude at the offset edge length along the y axis in the Z plane at different time instances

Comparing the mesh for the different times and along the same slices (figure 5.50), the meshes are similar in a general sense. Therefore the lack of data cannot be attributed to the general coarseness of the mesh. The mesh itself has undergone some heavy distortion that there is no consistency in terms of the shape of the mesh. The mesh may be similar, even on a finer scale (figure 5.51), however what is different is the portions of flow through the y lines. The plots presented indicate that the spread of data is different between time instances. This shows a lack of self-similarity.

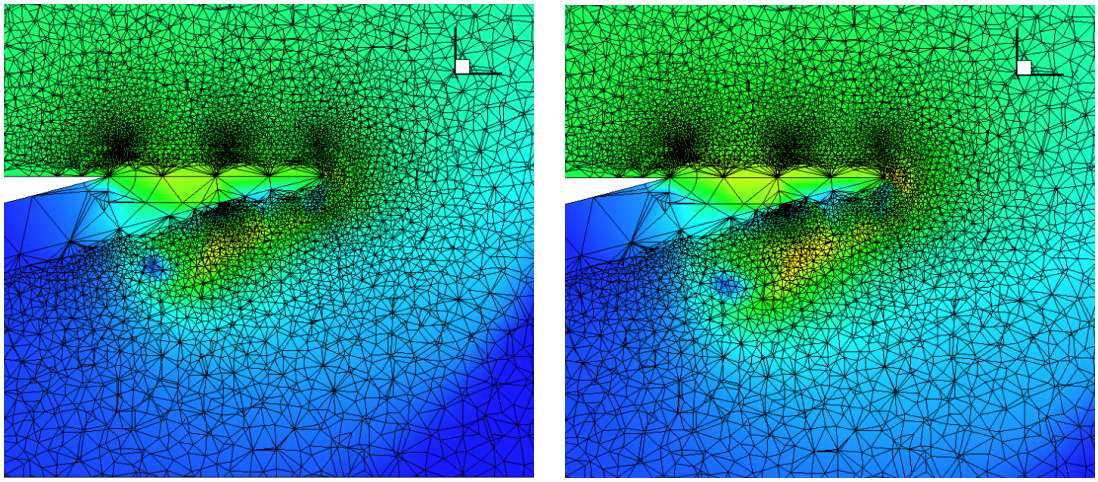

Figure 5.50: Mesh overlaid on contours of velocity magnitude at 54μs (left) and 71μs (right)

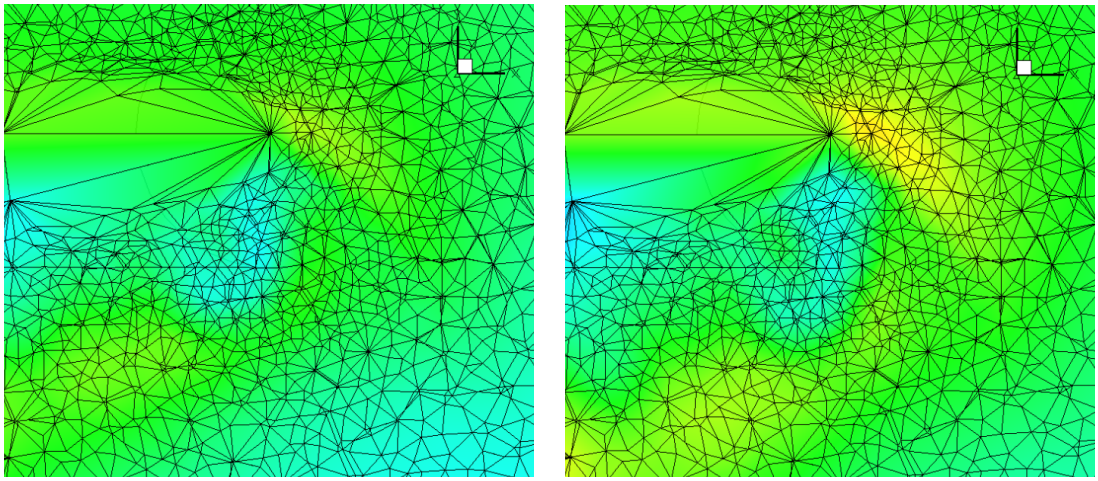

Figure 5.51: Zoomed in view of mesh overlaid on contours of velocity magnitude at 54μs (left) and 71μs (right)

As for the discrepancy in the data, the most likely cause is that for a time of 71μs the y line is closer to the downstream edge. This point is closer to a solid boundary which would explain the zero velocity. Secondly the mesh size is larger nearer the solid boundary (figure 5.51) and could account for the lack of data.

As has already been seen in the analysis so far, the three dimensional nature of the flow has caused a significant variation of a given parameter in the X plane. However, what is going to be investigated at this point is the variation of vorticity magnitude at different slices in the Z plane. The 10mm model has been used and slices were taken at the wall were the upstream edge met (0.037m from offset), the discontinuity (0m from offset) and at the wall of the downstream edge (-0.037m from offset) [figure 5.52]. A y line was taken through the data.

The results over the y line are similar for the different slices, apart from the region between $\pm$ 0.074 and 0.083m. There is an increase in vorticity magnitude in this region, which is in keeping with the contours of vorticity magnitude, in the sense that the maximum vorticity occurs at a specific region. The maximum vorticity across the three slices occurs at the offset edge length; which is not surprising. However what is surprising is the magnitude of how much larger it is. The same phenomena was seen when comparing the different offset edge lengths (figure 5.35). The initial thought was that the spike in vorticity along the discontinuity of the 10mm model was a function of geometry. However from analysing the geometry further, that seems not to be the case.

There is a set of data which are responsible for the spike; roughly about ten data points. There are many data points used in the various plots and given that a small number of data points have caused the peak, could be an indication of a coarse mesh about the y line chosen. The one data point that is exceptionally high is possibly due to the spread of vorticity about the discontinuity and a particular portion of high vorticity passing through the y line.

For a slice that passes through the upstream edge adjacent to the wall, the vorticity plot has a double peak. The rough between the peaks is where the maximum vorticity along the discontinuity occurs. The peak for the wall by the downstream edge is shifted to the right of the peak from the discontinuity. One would expect the peaks to be in different positions simply because the structure of the vortex at each of the slices chosen will be different.

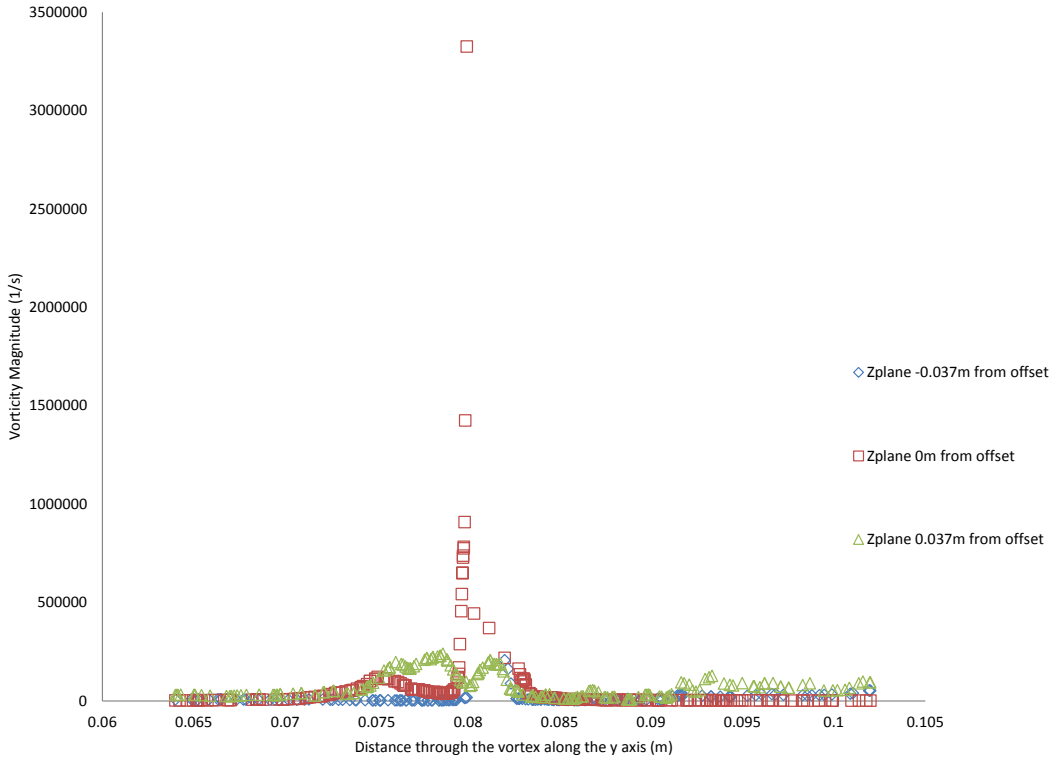

Figure 5.52: Variation of vorticity magnitude at the offset edge length along the y axis at different slices in the Z plane

To gain an understanding of the variation of parameters in three dimensions; surface plots were created. Isosurfaces, such as the ones that have already been presented, are surfaces of a parameter at a given value. Whereas surface plots; as in this case, has data taken along a constant z line and built up over a number of slices in the X plane. The end result is the surface plots for density (figure 5.53) and vorticity magnitude (figure 5.56).

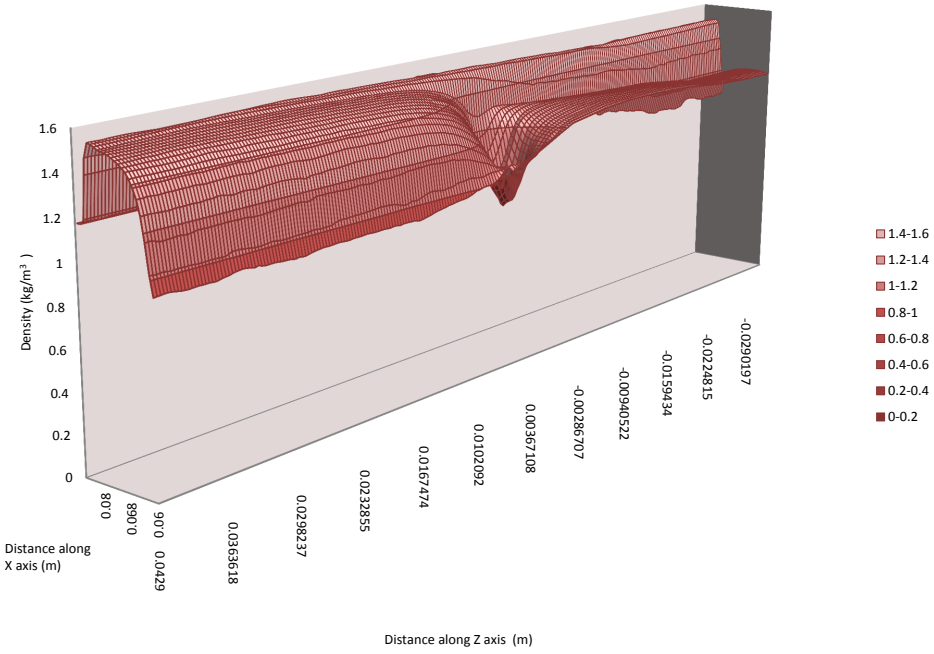

Figure 5.53: Surface plot of density at an angle of 310° for a 20mm model at a time of 54μs

The surface plots produced are for the 20mm model at a time of 54μs. Three views are taken at three different angles; 310° (figures 5.53 and 5.56), 40° (figures 5.54 and 5.56) and 120° (figures 5.55 and 5.56). On the z axis, as with the two dimensional plots, the positive values represent the downstream edge whereas the negative values represent the upstream edge. Where there is a drop in the density, there is a corresponding vorticity maximum. This fact has been already established along with these features being located on the downstream edge, adjacent to the offset edge length (can also be seen in figure 5.42).

There is a distinct density difference between the up and downstream edges (figure 5.54). This is an indication that the diffracted shock wave is at different stages in

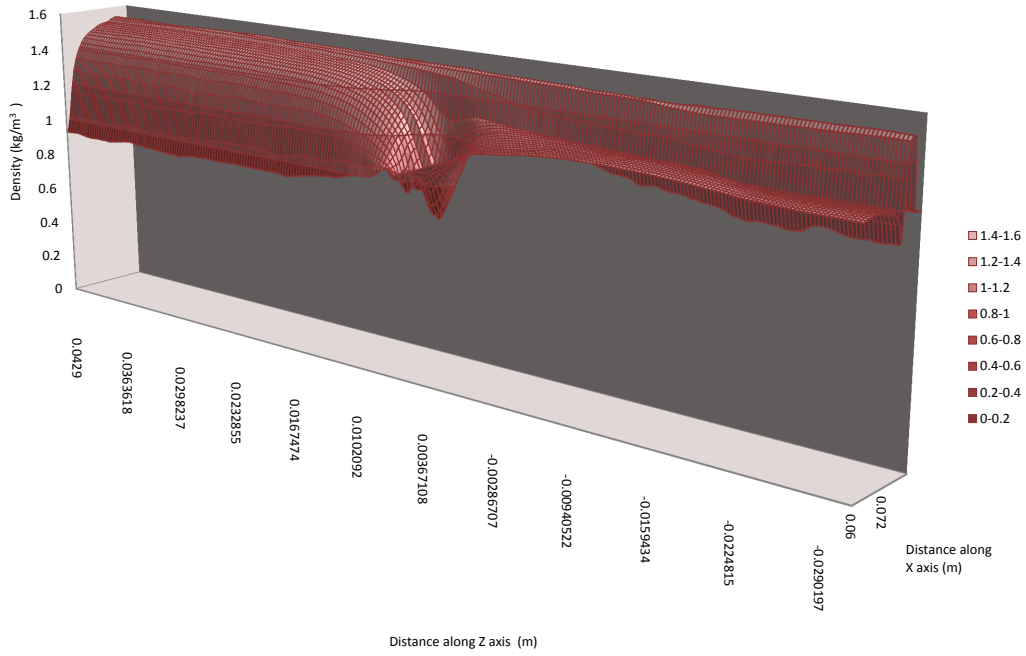

Figure 5.54: Surface plot of density at an angle of 40° for a 20mm model at a time of 54μs

its development; on the up and downstream edges. Given that it is one diffracted shock wave, a point of uniformity is reached, a point of constant density (seen in figure 5.55).

Similar features are seen on the vorticity magnitude surface plots. There is a distinction in the values on the up and downstream edges. The downstream edge has higher values of vorticity, which suggests that the vorticity magnitude is a function of the geometry of the model. On the upstream edge, there is a portion of the plot which is close to zero. This point coupled with the fact that the peaks of vorticity magnitude occur at different locations along the x axis (figure 5.56), further highlights the effect of geometry.

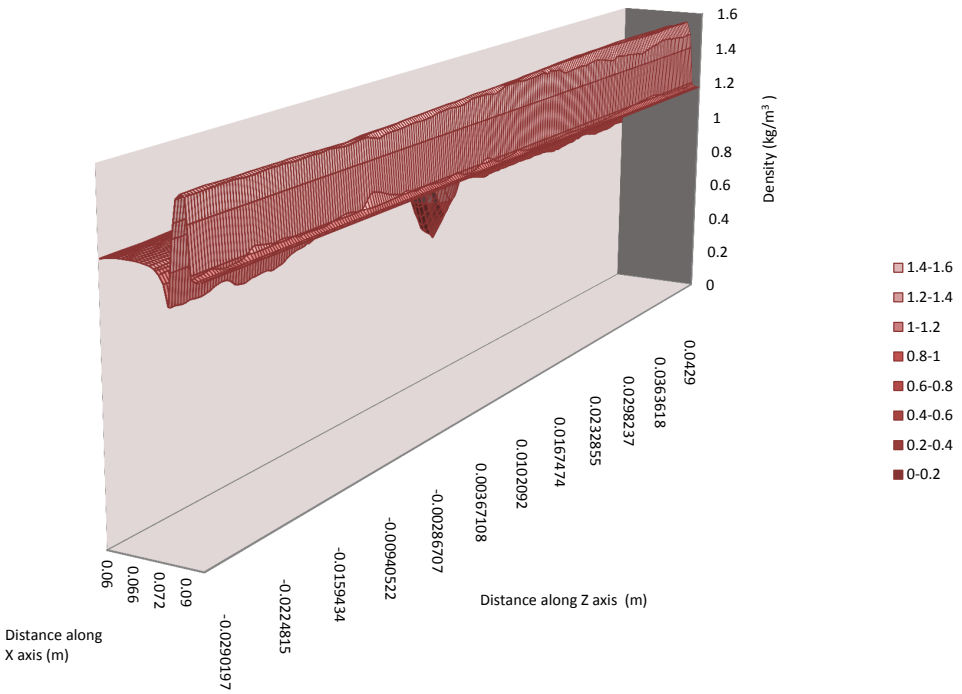

Figure 5.55: Surface plot of density at an angle of 120° for a 20mm model at a time of 54μs

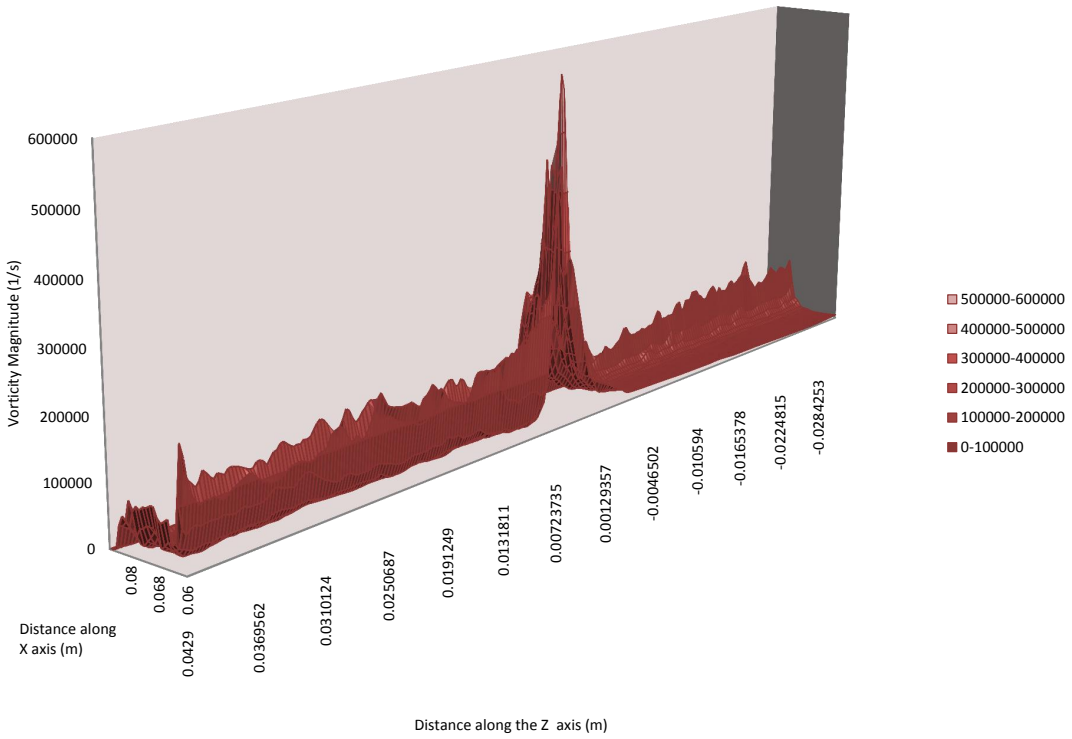

Figure 5.56: Surface plot of vorticity magnitude at an angle of 310° for a 20mm model at a time of 54μs

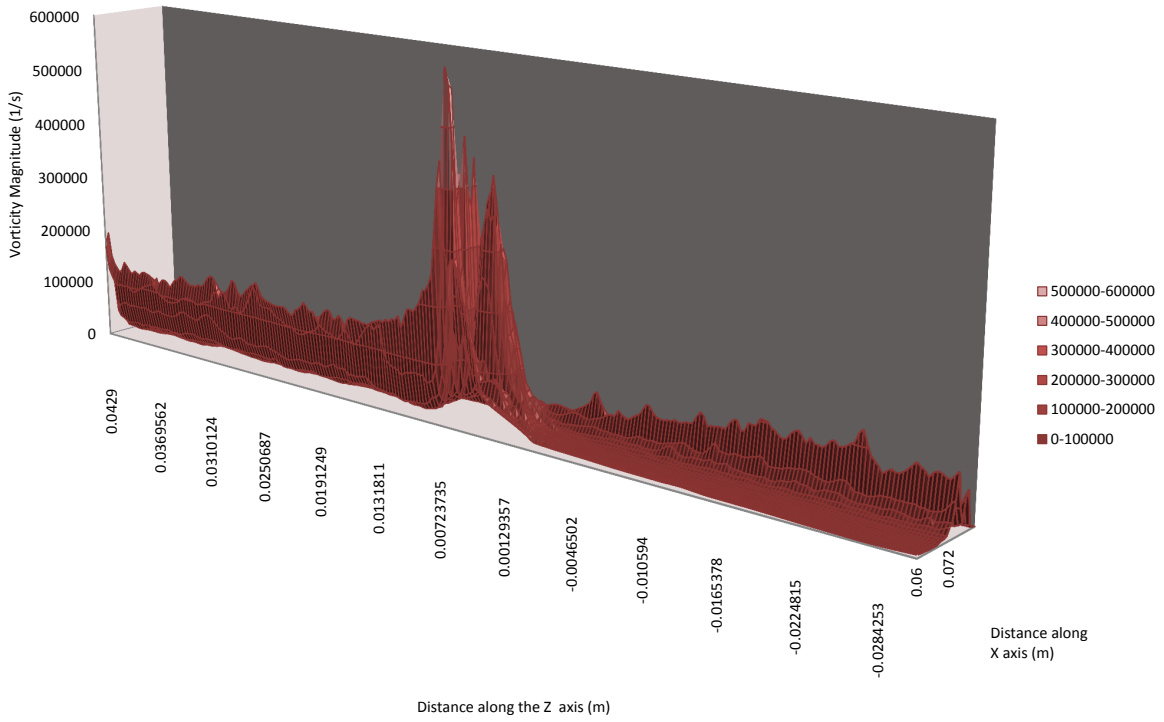

Figure 5.57: Surface plot of vorticity magnitude at an angle of 40° for a 20mm model at a time of 54μs

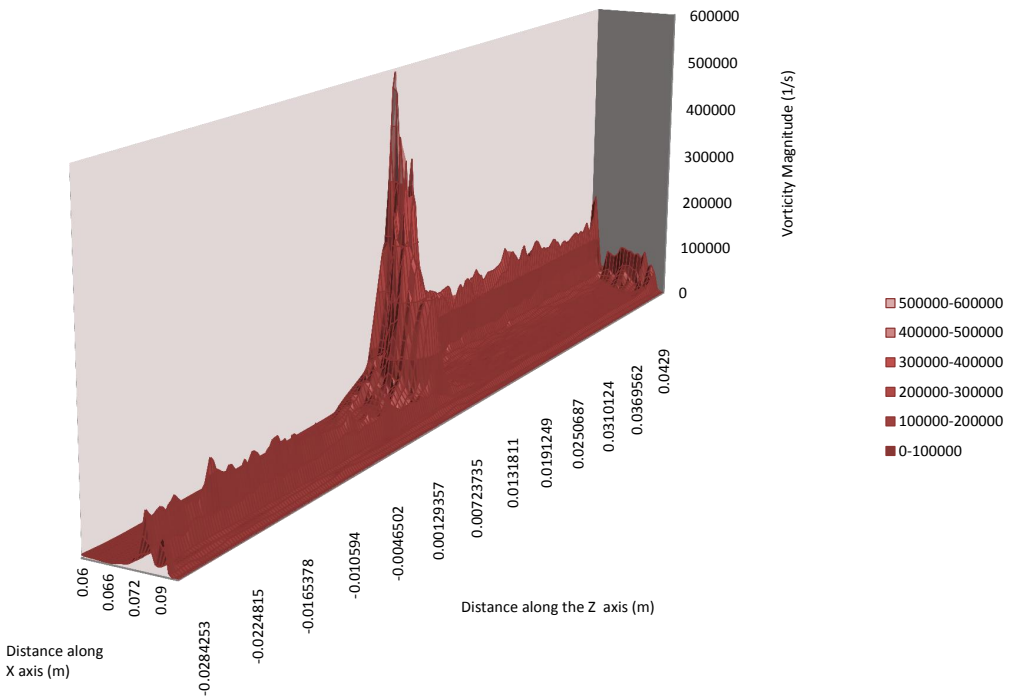

Figure 5.58: Surface plot of vorticity magnitude at an angle of 120° for a 20mm model at a time of 54μs

5.4 Mach 1.42

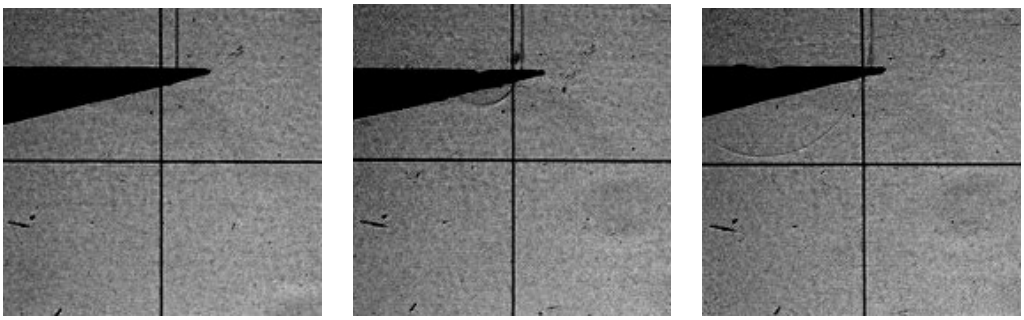

Figure 5.59: Experimental image of shock diffraction for Mach 1.42 at a time of ± -7μs

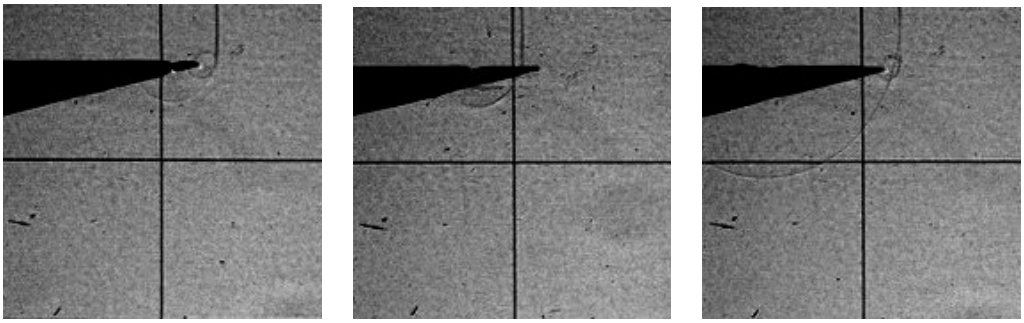

Figure 5.60: Experimental image of shock diffraction for Mach 1.42 at a time of ± 2μs

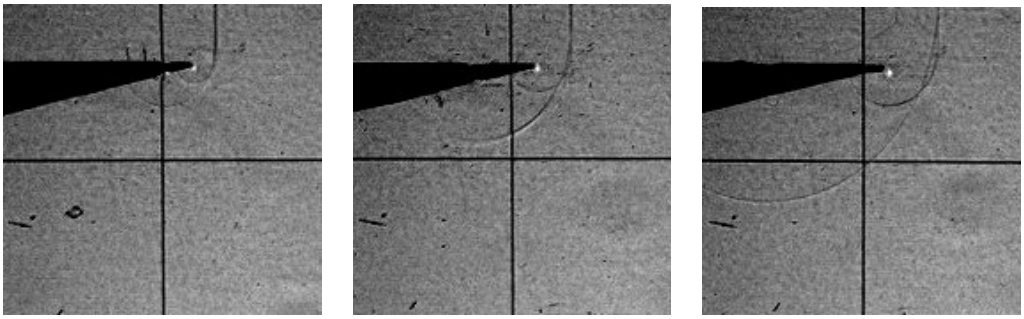

Figure 5.61: Experimental image of shock diffraction for Mach 1.42 at a time of ± 11μs

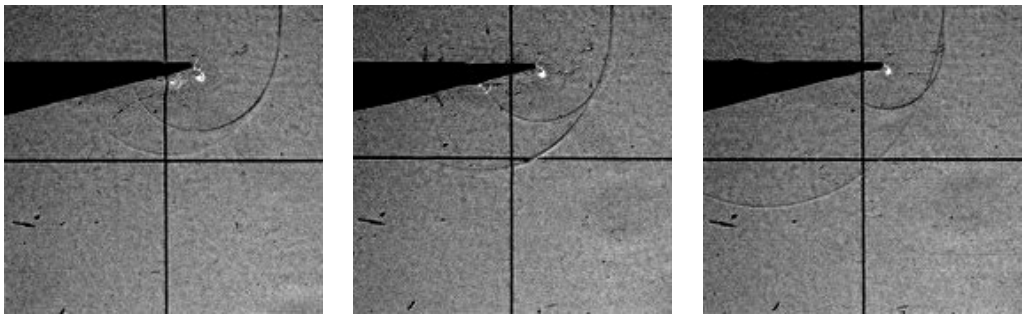

Figure 5.62: Experimental image of shock diffraction for Mach 1.42 at a time of ± 23μs

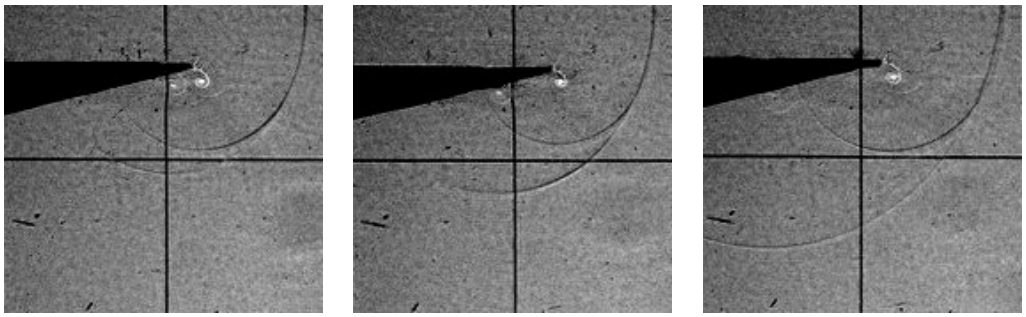

Figure 5.63: Experimental image of shock diffraction for Mach 1.42 at a time of ± 37μs

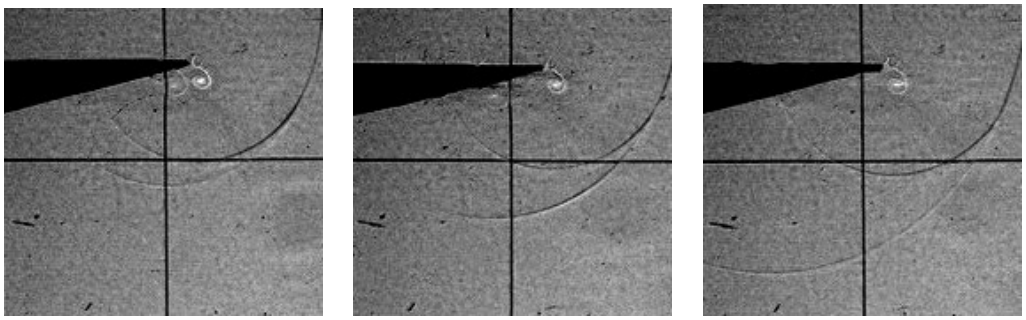

Figure 5.64: Experimental image of shock diffraction for Mach 1.42 at a time of ± 45μs

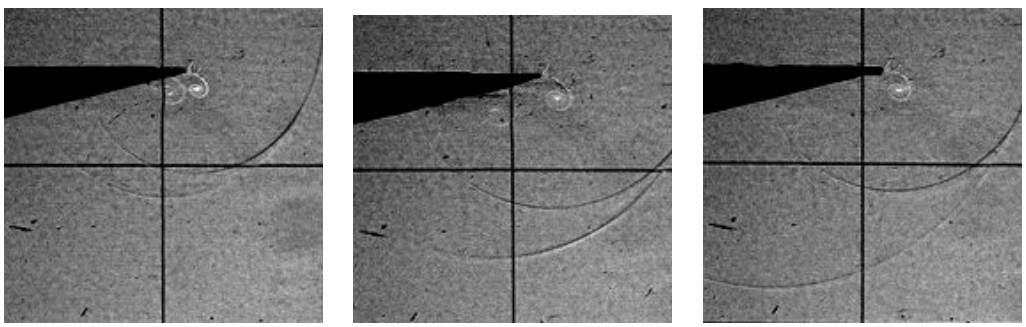

Figure 5.65: Experimental image of shock diffraction for Mach 1.42 at a time of ± 51μs

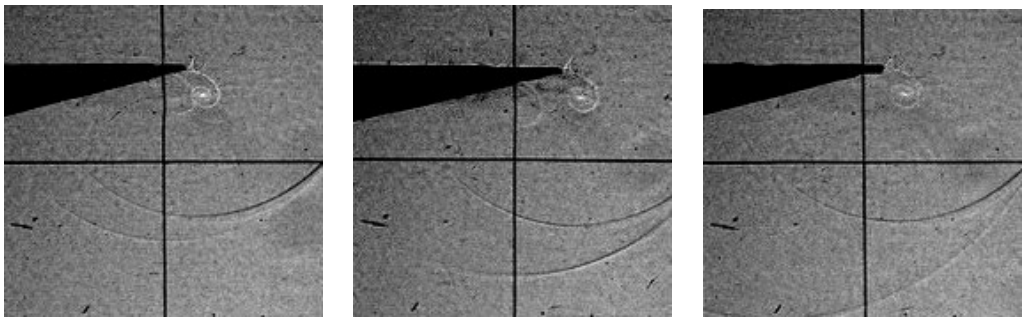

Figure 5.66: Experimental image of shock diffraction for Mach 1.42 at a time of ± 67μs

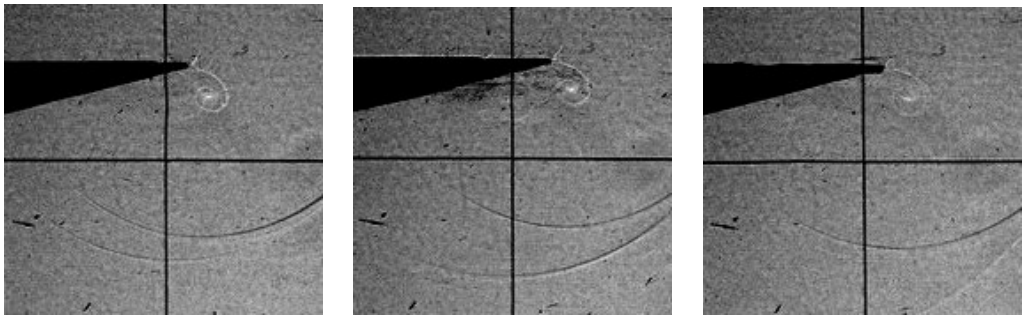

Figure 5.67: Experimental image of shock diffraction for Mach 1.42 at a time of ± 75μs

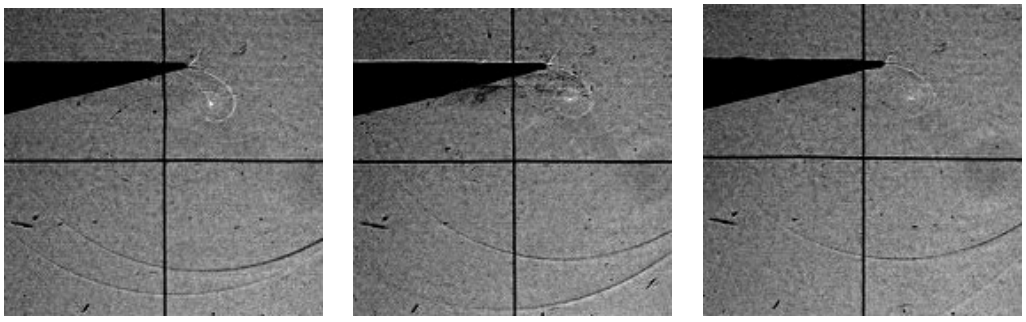

Figure 5.68: Experimental image of shock diffraction for Mach 1.42 at a time of ± 86μs

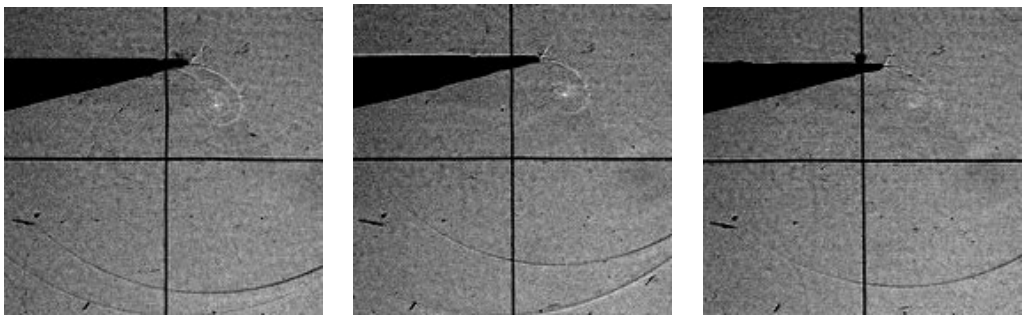

Figure 5.69: Experimental image of shock diffraction for Mach 1.42 at a time of ± 94μs

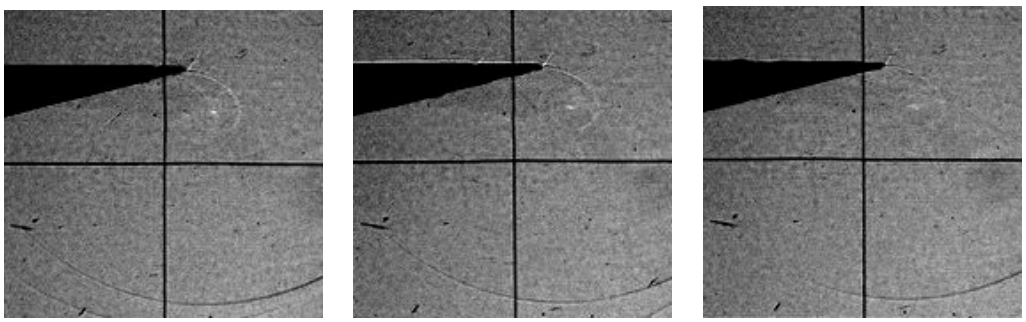

Figure 5.70: Experimental image of shock diffraction for Mach 1.42 at a time of ± 101μs

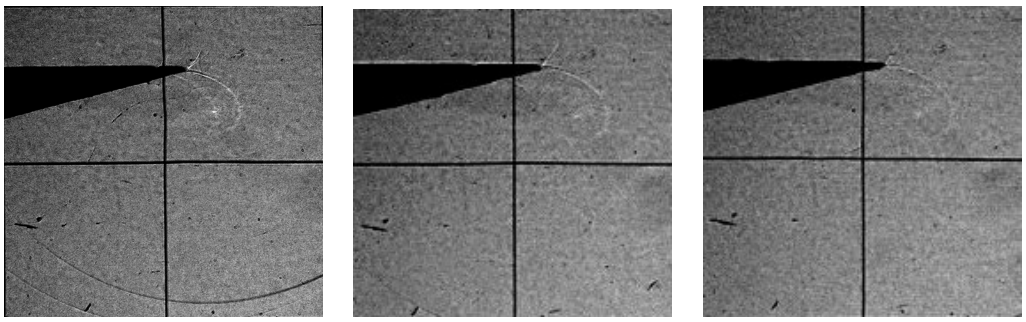

Figure 5.71: Experimental image of shock diffraction for Mach 1.42 at a time of ± 111μs

5.4.1 Effect of change in Mach number

The shadowgraph imaging provides a different insight to what is going on in the flow regime. The vortices are seen to have a defined shape and structure.

The vortex shed of the downstream edge can be seen clearly on all three models (figures 5.62 to 5.67). From figure 5.66 and beyond, it can be shown that the downstream vortex expands at different rates for the various sized offsets. The larger the discontinuity, the quicker the downstream vortex expands. For the 20mm model, the flow over the upstream edge diffracts before either the 5mm or 10mm models (figure 5.59), when coupled with the fact that the interaction between the vortices decreases with increasing offset edge length could possibly be the cause for the vortices expanding at different rates.

The upstream vortex is less visible in the images with a higher offset edge length. This could be due to the fact for a larger discontinuity the flow is more expanded and therefore more difficult to see (figures 5.67 to 5.71). Alternatively the larger the vortex, the larger the portion of the upstream edge blocked from sight by the model.

In general a number of features risen above were outlined at Mach 1.32. The fundamental difference between the flow at Mach 1.32 and 1.42 is the appearance of shocklets at Mach 1.42. One can therefore infer that the flow features between Mach 1.32 and 1.42 are similar. The shocklets are not seen on the upstream vortex as the shocklets appear on the shear layer, which is hidden by the model for all three offset edge lengths. The primary cause for the formation of shocklets is the velocity of the flow. The velocity around the diffraction edges is transonic, and the transonic flow manifests itself as shocklets.

Reeves (2010) found that an increase in Mach number caused a lengthening of the shear layer and an elliptical profile for the free vortices. Reeves (2010) analysed three Mach numbers; 1.32, 1.42, and 1.65. The results for Mach 1.32 were not presented as it was deemed to be similar to Mach 1.42 and therefore did not provide any additional insight. The effects for a change in Mach number were found by comparing Mach 1.42 to 1.65.

Given that two optics systems were used, it is challenging to gauge the effect of Mach number from experimental images. It is particularly difficult with the free vortices, as the schlieren system portrays vortices as a haze.

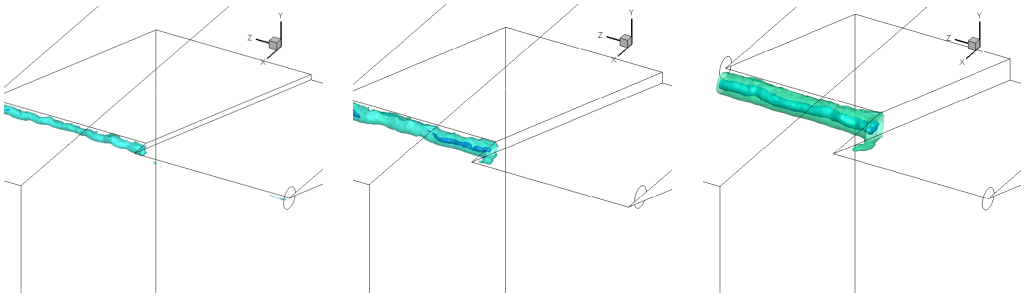

Figure 5.72: Isosurfaces of density of a value of 0.8 kg/m^3 on the inner surface and 1.1kg/m^3 on the outer surface for Mach 1.42 at a time delay of $\pm$ 8μs

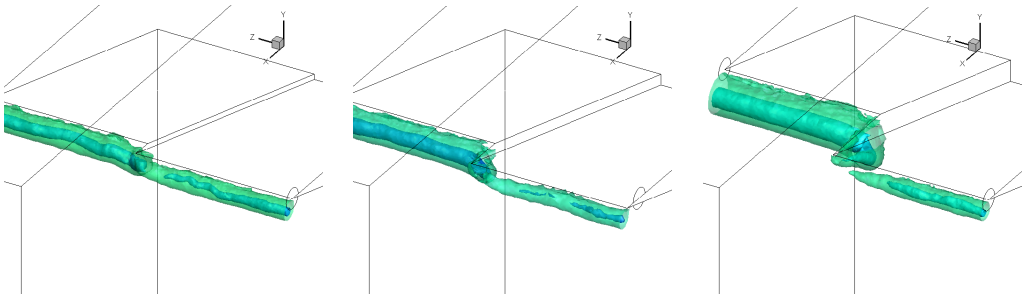

Figure 5.73: Isosurfaces of density of a value of 0.8 kg/m^3 on the inner surface and 1.1kg/m^3 on the outer surface for Mach 1.42 at a time delay of $\pm$ 34μs

The time span in figures 5.18 to 5.21 and in figures 5.72 to 5.75 are similar; $\pm$ 90μs.

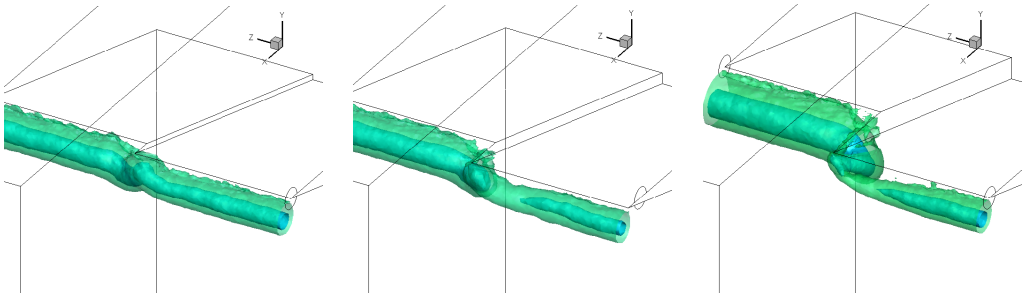

Figure 5.74: Isosurfaces of density for Mach 1.42 a value of 0.8 kg/m^3 on the inner surface and 1.1kg/m^3 on the outer surface for Mach 1.42 at a time delay of $\pm$ 62μs

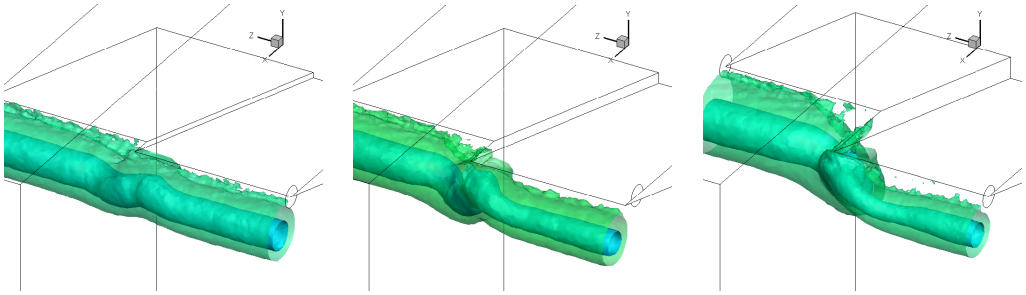

Figure 5.75: Isosurfaces of density of a value of 0.8 kg/m^3 on the inner surface and 1.1kg/m^3 on the outer surface for Mach 1.42 at a time delay of $\pm$ 106μs

The flow develops more rapidly in the case of Mach 1.42. This is an expected result, as the same distance is covered with a quicker speed. This is an indication that an increase in Mach number causes the free vortices to expand at a quicker rate. This feature is demonstrated in figures 5.21 and 5.75 as the isosurfaces at a similar time are larger for Mach 1.42.

The effect on the rate of expanison can be seen in figures 5.73 and 5.74 as the size of the isosurfaces, particularly in terms of diameter of the upstream vortex increases with a larger offset. This feature can vaguely be seen at Mach 1.32 (figures 5.19 and 5.20) but is difficult to identify, mainly due to the gaps in the isosurfaces. The same gaps are not as prevalent at Mach 1.42. The isosurfaces grow at a faster rate at Mach 1.42, which infers that there are less likely changes in density over the same time span.

The isosurfaces are not as smooth in figure 5.73 as the equivalent at Mach 1.32 (figure 5.19). A possible explanation is the regions of transonic flow and the irregularities on the isosurfaces maybe the shocklets expressed in the computational model. However at later times, the isosurfaces are smooth, or are as smooth as the isosurfaces at Mach 1.32. From the experimental images, figures 5.67 and onwards the shocklets are not seen as clearly. One can assume that the shocklets are dissipating with time

which is demonstrated computationally by the smoothing of the isosurfaces.

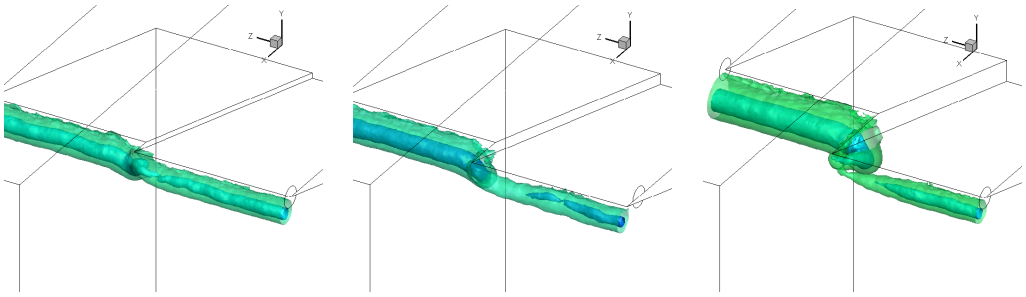

Figure 5.76: Isosurfaces of density for Mach 1.42 of a value of 0.8 kg/m^3 on the inner surface and 1.1kg/m^3 on the outer surface at a time delay of $\pm$ 44μs

There is a small change in density in the isosurfaces for the 5mm model as can be seen in figure 5.73. At a similar time, the density change for the 20mm model extends up until the offset edge length. These results are of similar nature at Mach 1.32, for an equivalent time. The 20mm model has larger changes in density for Mach 1.32 in comparison to Mach 1.42.

A common feature between the two Mach numbers is that the gap between the isosurfaces increases for the 20mm model within a given time; which is seen by comparing figures 5.19 to 5.20 for Mach 1.32 and figures 5.73 to 5.76 for Mach 1.42. The gaps in the isosurfaces occur in similar trends for the different models in the Mach numbers analysed to date.

5.4.2 Effect of Discontinuity

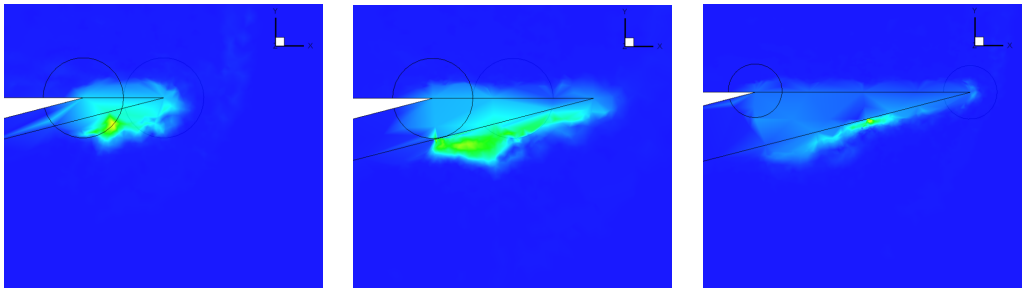

Figure 5.77: Plots of vorticity for Mach 1.42 at a time delay of $\pm$ 8μs

There is a strong resemblance between the plots of vorticity between Mach 1.32 and 1.42 (figures 5.26 to 5.29 and 5.77 to 5.80), mainly in terms of shape. As previously stated, the flow is more developed for Mach 1.42 and can be seen from the vorticity plots.

Similar shapes are formed with the vorticity plots between the two Mach numbers;

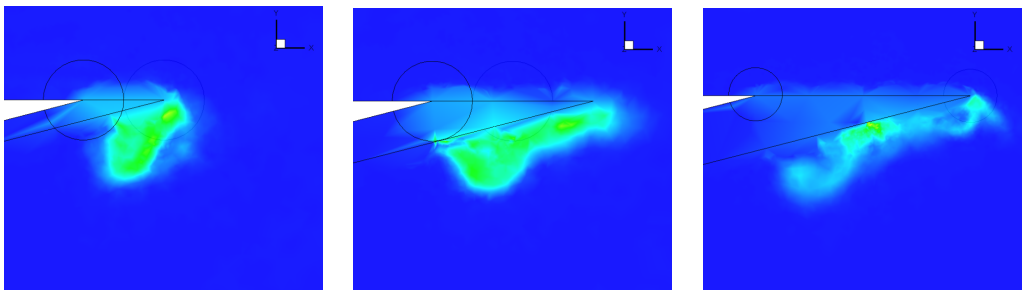

Figure 5.78: Plots of vorticity for Mach 1.42 at a time delay of ± 34μs

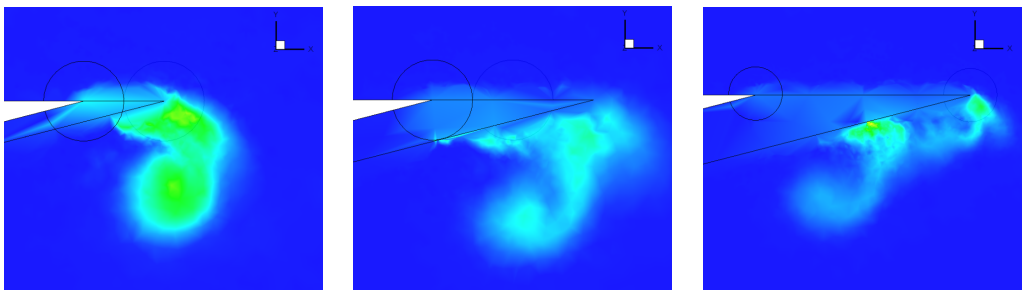

Figure 5.79: Plots of vorticity for Mach 1.42 at a time delay of ± 62μs

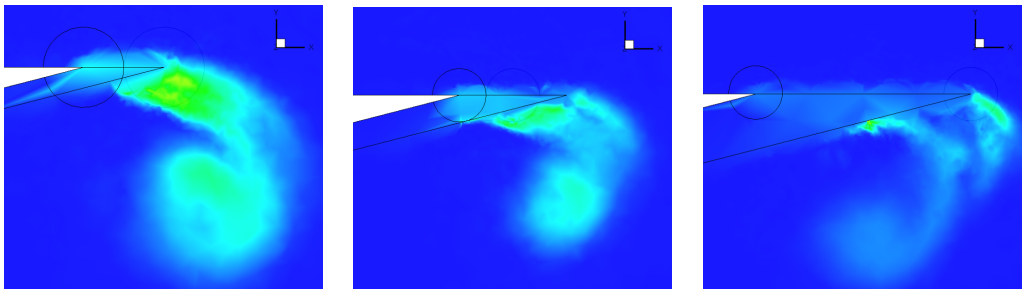

Figure 5.80: Plots of vorticity for Mach 1.42 at a time delay of ± 106μs

however the shapes are formed at different times. This is seen by comparing the vorticity plots at a time of ± 109μs for Mach 1.32 (figure 5.79) to Mach 1.42 at a time of ± 63μs (figure 5.79). The flow demonstrates similar characteristics between Mach 1.32 and 1.42. The regions of high vorticity are close to the diffraction edges. At a time of ± 105μs (figure 5.80) the separation of the vortices from the up and downstream edges can be seen as the models increase in size. The 5mm model shows what seems to be a single free vortex with a large shear layer; which is an indication of the strong interaction of the vortices from the up and downstream edges. The appearance of the vorticity plots for the 10mm is similar to a single vortex that has been heavily distorted. There is a degree of separation as shear layers from each edge can vaguely be seen. On the other hand, there is a clear distinction between the flow from the up and downstream edges for the 20mm model.

For a smaller offset edge length, the vorticity is more concentrated and could be a

contributing factor to the decreasing of the vorticity magnitude with increasing size of the offset edge length. This feature is seen throughout the vorticity plots, but is clearly evident at 105μs. The experimental images show that the vortices expand at different rates for the various models; the decreasing vorticity magnitude could be a reflection of the expanison rate for the different models expressed computationally.

5.4.3 Shape of Diffracted Shock

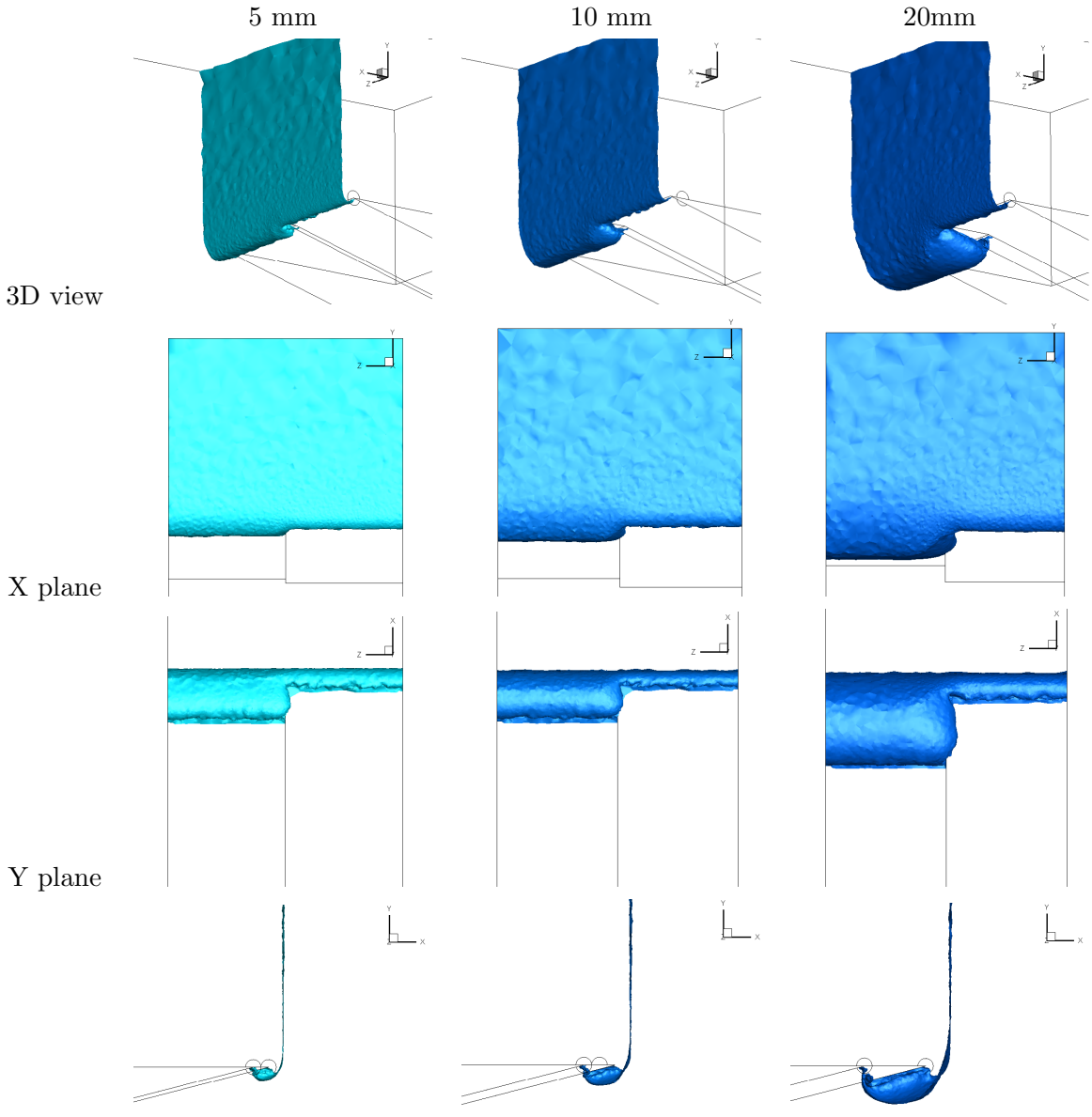

Figure 5.81: Velocity magnitude isosurfaces for Mach 1.42 at a time of ± 10μs at Mach 1.42

The flow features are similar between the two Mach numbers; it comes as no surprise

that there is such similarity in the shape of the diffracted shock wave. Figures 5.33 and 5.81 are analysed at the same time.

The three dimensional view shows that there is no significant size change between the two Mach numbers. This is an unusual result; as the flow for Mach 1.42 develops at a quicker rate. However the time chosen for analysis, $\pm$ 10μs, is early in the flow regime and there is likely to be resemblances as the vortices have not expanded significantly. This suggestion is supported by the plots of vorticity between the two Mach numbers at the same time being alike (figures 5.26 and 5.77).

The velocity plots on the X and Y planes for Mach 1.42 show that there is a larger portion of flow around and underneath the offset edge length, in comparison to Mach 1.32, particularly for the 20mm model. The plots in the X and Y plane show that there may not be such a large change in the size of the diffracted shock but there is a change in the shape. This is evident in the Z plane; where the plots have more of a dip in the curvature of the diffracted shock wave.

The change in shape may be as a result of the quicker development of the flow.

5.5 Mach 1.6

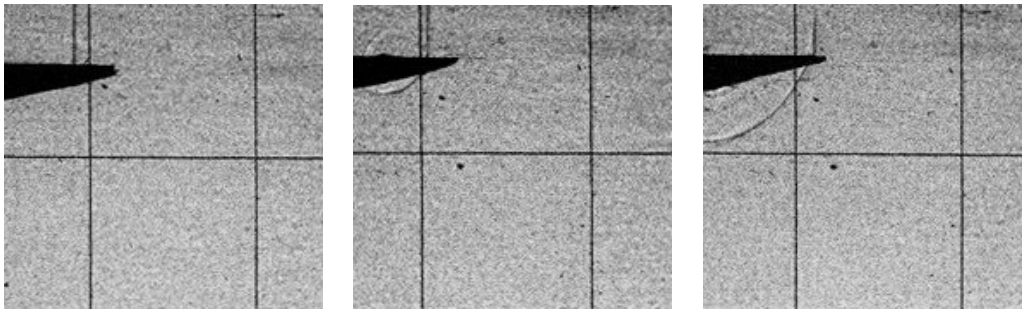

Figure 5.82: Experimental image of shock diffraction for Mach 1.6 at a time of ± -6μs

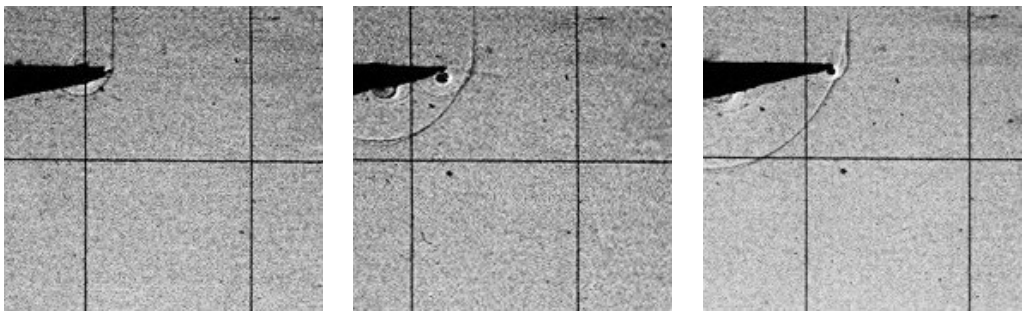

Figure 5.83: Experimental image of shock diffraction for Mach 1.6 at a time of ± 5μs

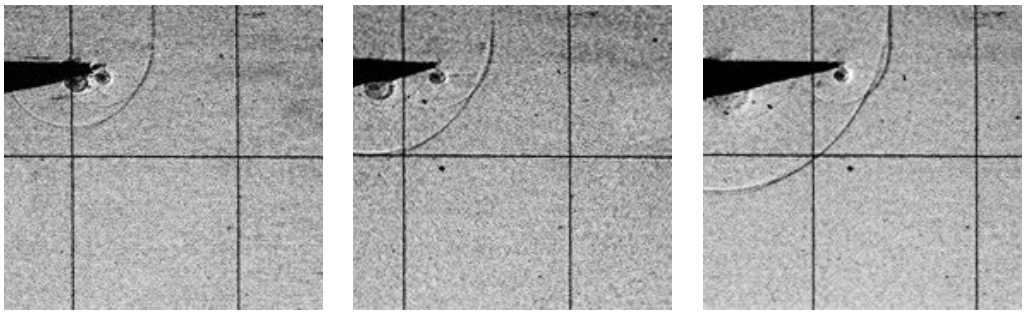

Figure 5.84: Experimental image of shock diffraction for Mach 1.6 at a time of ± 16μs

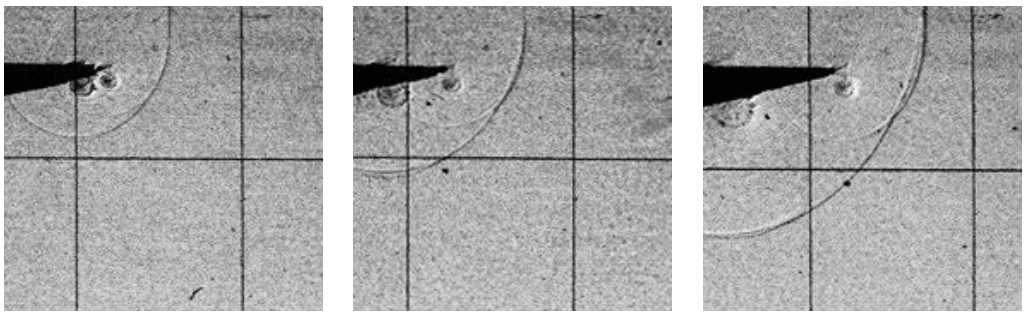

Figure 5.85: Experimental image of shock diffraction for Mach 1.6 at a time of ± 23μs

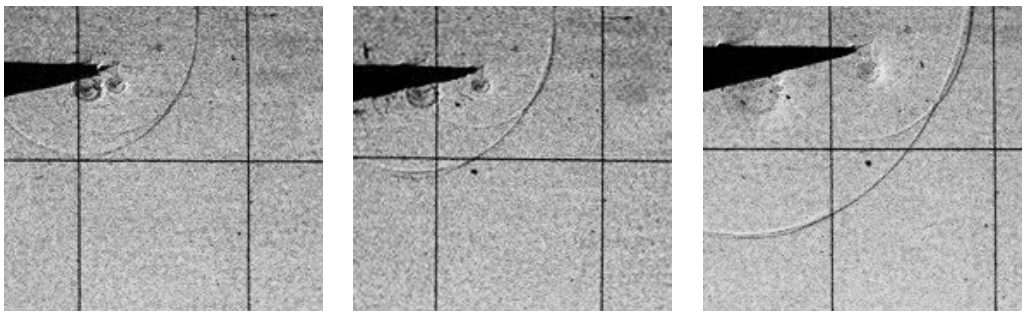

Figure 5.86: Experimental image of shock diffraction for Mach 1.6 at a time of ± 28μs

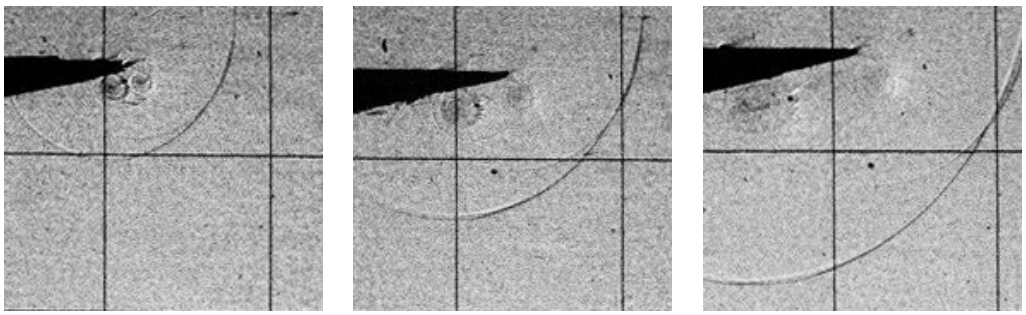

Figure 5.87: Experimental image of shock diffraction for Mach 1.6 at a time of ± 39μs

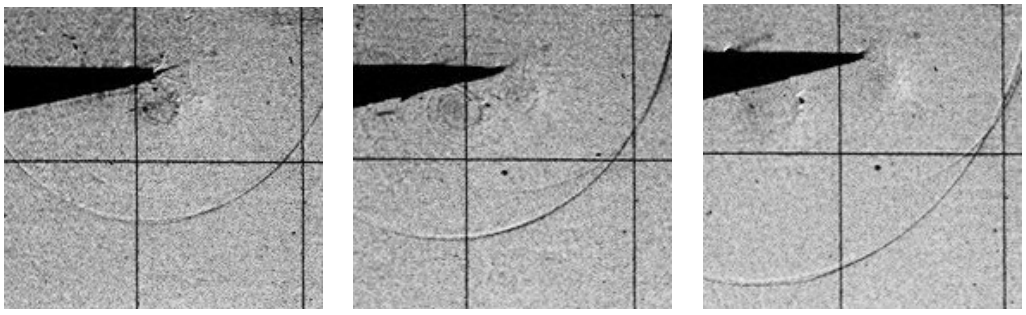

Figure 5.88: Experimental image of shock diffraction for Mach 1.6 at a time of ± 47μs

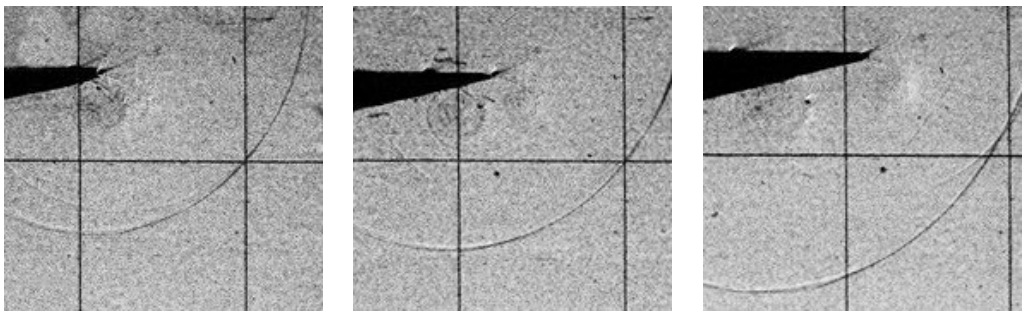

Figure 5.89: Experimental image of shock diffraction for Mach 1.6 at a time of ± 55μs

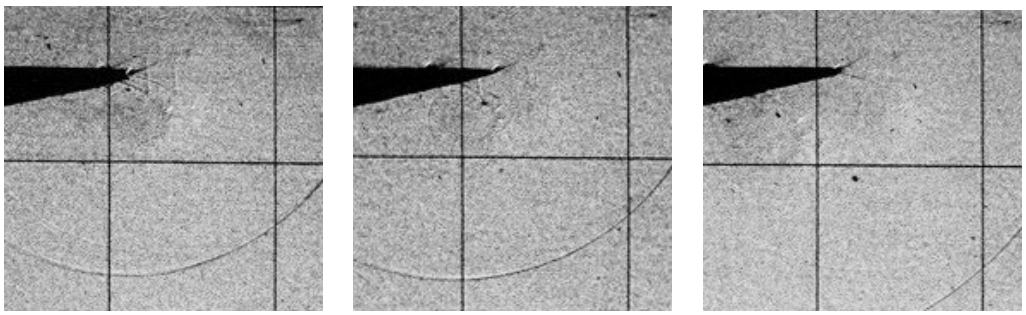

Figure 5.90: Experimental image of shock diffraction for Mach 1.6 at a time of ± 73μs

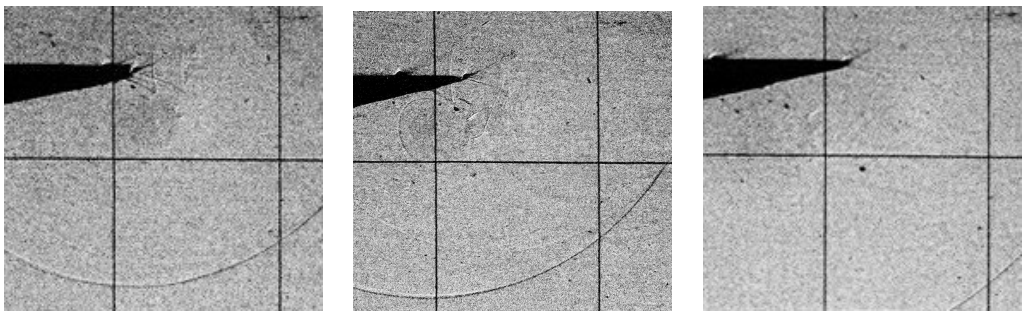

Figure 5.91: Experimental image of shock diffraction for Mach 1.6 at a time of ± 78μs

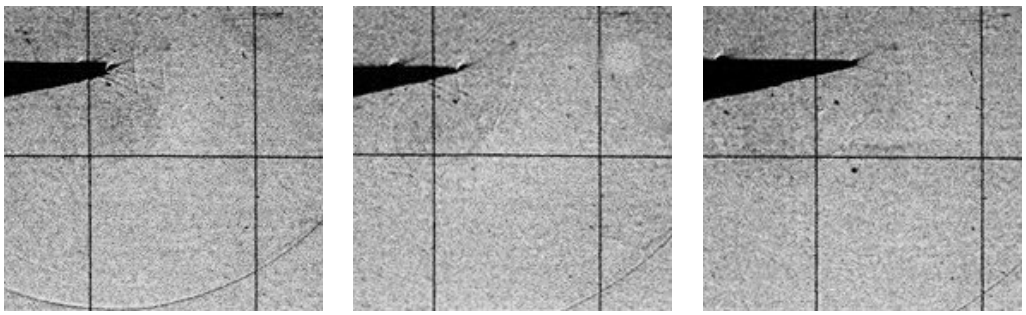

Figure 5.92: Experimental image of shock diffraction for Mach 1.6 at a time of ± 89μs

A higher sensitivity was achieved for Mach 1.6; as demonstrated by comparing experimental images between Mach 1.6 and 1.42. A feature that adds clarity to the images is the correctly applying of masking tape to both sides of the model. If the masking tape is not correctly cut, i.e. there are jagged edges; it can be and is seen in the experimental images (Figures 5.1 to 5.13 - Mach 1.32). The jagged edges have minimal effect on the flow but can be mistakenly identified for flow features.

Mach 1.6 places a great deal of force on the model. This is evident for the 5mm model; where a portion of the masking tape has been torn off (Figures 5.86 to 5.92). The excess flow through the gap of the torn masking tape impedes the flow in terms of the visualization of the free vortices. The implication is that the rate of expansion of the free vortices is affected. Based on the analysis of the Mach 1.42 results; the rate of expansion increases for a larger offset. Before the effect of the masking tape can take place, figure 5.86 supports the idea of an increase in the rate of expansion for a larger offset. The visibility of the free vortices decreases with increasing size of the discontinuity; the free vortices have undergone more or less expansion depending on the size of the offset.

The free vortices across all models can be seen to have an elliptical shape. This is demonstrated clearly by the upstream vortex. In addition to producing a more elliptical profile for the vortex, an increase in Mach number should have the effect of causing the shear layer to lengthen. This feature can be seen by comparing experimental images for the 10mm model at $\pm$ 22μs from Mach 1.42 (figure 5.62) to 1.6 (figure 5.85).

A distinct feature of Mach 1.6 is the appearance of lambda shock configurations. As with the shocklets at Mach 1.42, the effect of the velocity around the diffraction edges becoming transonic is clearly seen on the downstream vortex. Reeves (2010) identified lambda shock configurations at Mach 1.65. He also found that secondary and tertiary shocks appeared at this Mach number. For a two dimensional case, secondary shocks are present at $\pm$ Mach 1.35 (Sun & Takayama (1996)). In a three dimensional case, the Mach number is higher. However, with the current study, no secondary or tertiary shocks are present at Mach 1.6. Possible causes would be that a Mach number of 1.6 is too low, and a Mach number of approximately 1.65 is more appropriate. Reeves (2010) used schlieren imaging at Mach 1.65, which has a higher sensitivity than shadowgraph imaging. The increased sensitivity may have allowed subtle features such as secondary and tertiary shocks to be picked up.

There are more irregularities on the isosurfaces for Mach 1.6 then previous Mach numbers. These irregularities are present for a longer period of time then at Mach

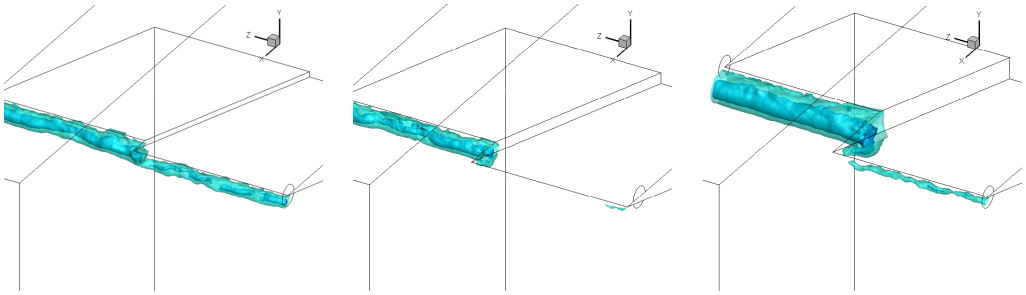

Figure 5.93: Isosurfaces of density for Mach 1.6 of a value of 0.8 kg/m^3 on the inner surface and 1.1kg/m^3 on the outer surface at a time delay of $\pm$ 13μs

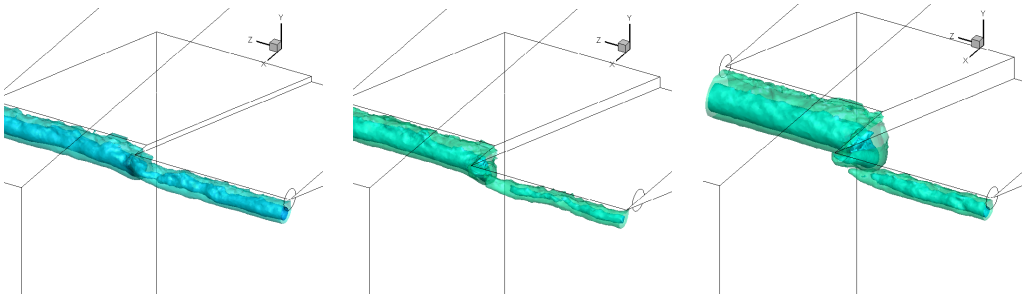

Figure 5.94: Isosurfaces of density for Mach 1.6 of a value of 0.8 kg/m^3 on the inner surface and 1.1kg/m^3 on the outer surface at a time delay of $\pm$ 29μs

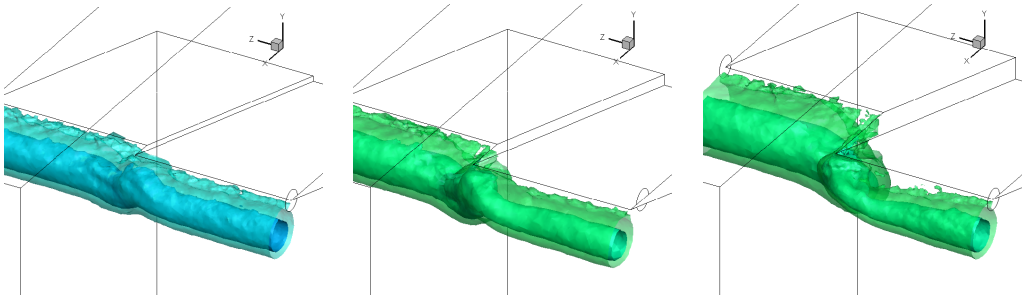

Figure 5.95: Isosurfaces of density for Mach 1.6 of a value of 0.8 kg/m^3 on the inner surface and 1.1kg/m^3 on the outer surface at a time delay of $\pm$ 74μs

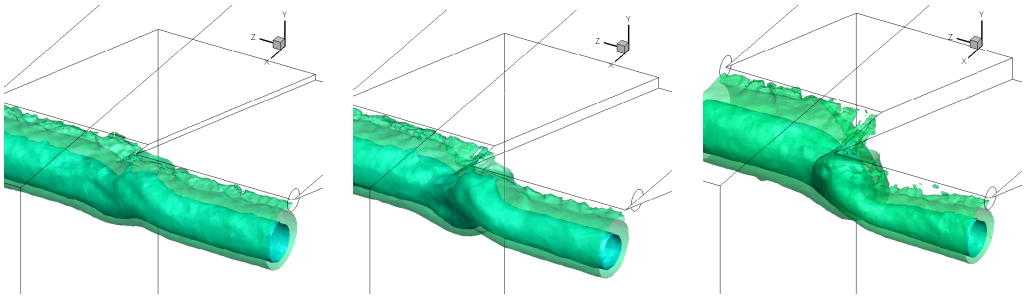

Figure 5.96: Isosurfaces of density for Mach 1.6 of a value of 0.8 kg/m^3 on the inner surface and 1.1kg/m^3 on the outer surface at a time delay of $\pm$ 88μs

1.42. At a time of ± 88μs (figure 5.96) there are irregularities at Mach 1.6, whereas for Mach 1.42 the isosurfaces were fairly smooth by ± 63μs (figure 5.74). This suggests that the flow around the diffraction edges is at a higher velocity then at Mach 1.42; but still transonic (presence of lambda shock configurations). The suggestion is that the lambda shock configurations take a longer time to expand than shocklets.

There are similarities between the various Mach numbers; mainly the gap which is present on the downstream edge adjacent to the offset edge length. This gap, as previously established is the change in density of the downstream vortex adjacent to the offset, is significant for the 20mm model. With regards to the 5mm and 10mm models, this feature is not as significant. One can therefore infer that an increase in Mach number reduces the effect of the offset (to some extent) on the vortex topology. Higher Mach numbers will cover the same distance in a quicker time. This infers that there is a stronger interaction for the same offset but at a higher Mach number, as there is less of a lag between the flow over the up and downstream edges. This is evident by comparing isosurfaces of density for Mach 1.32, 1.42 and 1.6 for the 10mm model (figures 5.21, 5.75 and 5.96).

As expected the flow develops quicker at Mach 1.6 than previous Mach numbers. There is a clear difference in the size of the isosurfaces at a time of ± 30μs for the different offsets (figure 5.94). From times of 75μs to 88μs there is a size difference between the vortices from the different offsets, but it is not as distinct as earlier times. Therefore the rate of expanison is affected by the Mach number. An increase in Mach number causes the vortices, across all models, to expand at a quicker rate. The upper limit (in terms of time instances) for the isosurfaces of density for Mach 1.6 is ± 90μs, which is at least 10μs less than the upper limit for either Mach 1.42 or 1.32. Despite the shorter time span, larger isosurfaces of density are produced. This feature holds true when comparing Mach 1.42 to 1.32.

5.5.1 Effect of Discontinuity

Across the three Mach numbers, the vorticity plots have similar shapes, as the flow progresses with time. The similarity of the shapes of the vorticity plots is a result one would expect, as the geometries among the three Mach numbers remains constant. However the size of the vorticity plots increase with Mach number. The size difference is evident early on in the flow regime, i.e. at a time of ± 30μs (figures 5.27, 5.78 and 5.98). The size difference is due to the fact that the flow develops at a quicker rate for higher Mach numbers.

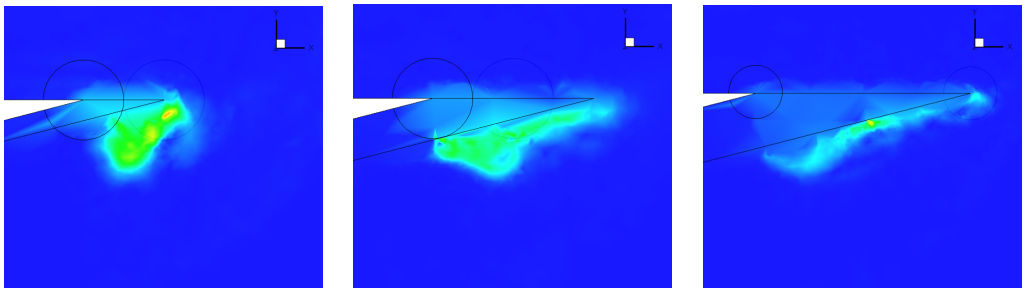

Figure 5.97: Plots of vorticity for Mach 1.6 at a time delay of ± 13μs

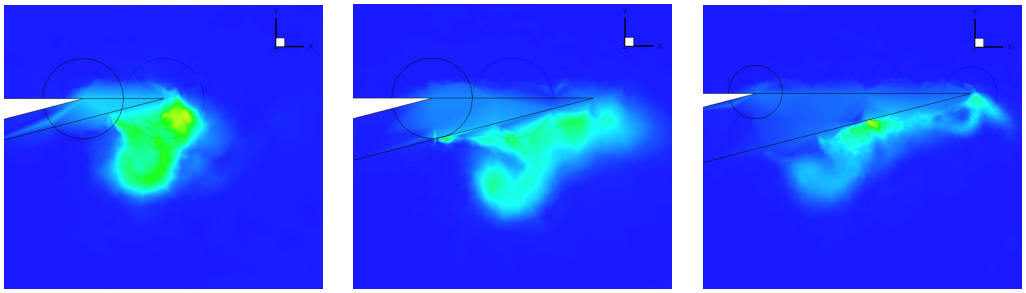

Figure 5.98: Plots of vorticity for Mach 1.6 at a time delay of ± 29μs

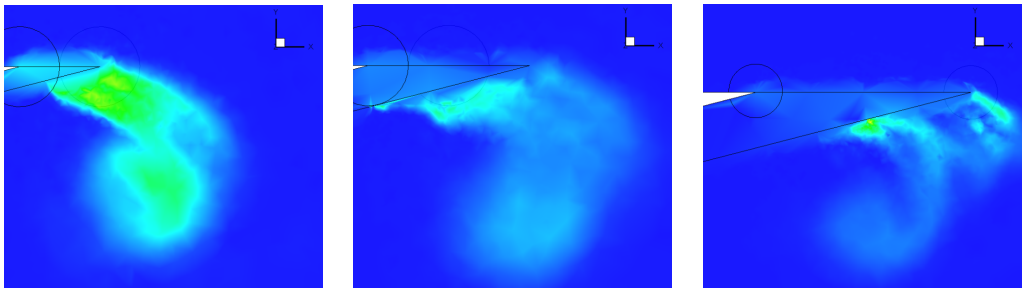

Figure 5.99: Plots of vorticity for Mach 1.6 at a time delay of ± 74μs

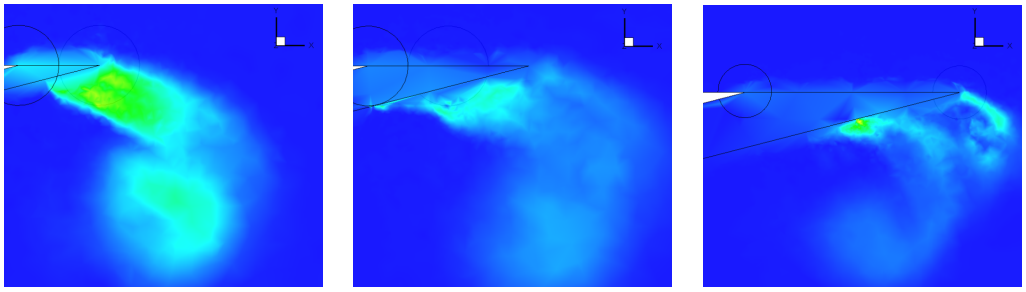

Figure 5.100: Plots of vorticity for Mach 1.6 at a time delay of ± 88μs

While there is a trend in the shape of the vorticity plots for the different Mach numbers; there is a variation in the vorticity magnitude. The magnitude of vorticity is the largest for Mach 1.6, which occurs near the offset edge length and close to the underside of the downstream edge. It has been established that an increase in Mach number affects the rate of expanison. Since vorticity is a measure of rotation of a fluid, it is expected that the vorticity magnitude would increase with Mach number.

The vorticity magnitude not only varies as a result of the Mach number but also because of the geometry. The 5mm model has a larger vorticity magnitude in comparison to remaining models. The interaction between the up and downstream vortices is the strongest for the 5mm model. This suggests that a strong interaction is linked to the magnitude of the vorticity; as in a stronger interaction produces a larger vorticity magnitude.

In terms of shape, size and magnitude; there is not much variation in the plots between figures 5.99 and 5.100. This suggests that the flow is fully developed by a time of 75μs.

5.5.2 Shape of Diffracted Shock

The results of the velocity magnitude contours show that the shape of the diffracted shock wave is similar to the results produced at Mach 1.32 and 1.42. The X and Y planes show as the offset increases, a larger portion of the diffracted shock attaches at the discontinuity and to the underside of the model. This feature is clearly evident in the Z plane.

The Y plane shows little difference between the 5mm and 10mm models, in terms of shape and size; which is also seen at Mach 1.32 and 1.42. The obvious difference is the stretch of the isosurface along the offset edge length.

One noticeable feature is as the offset edge length increases in size, the gap (in the X direction) between the diffracted shock wave and the downstream edge decreases. From figures 5.33 and 5.81, Mach 1.32 and 1.42 exhibit the same features. The most likely explanation is for a bigger discontinuity, the shock wave has diffracted of the upstream edge for a longer period of time. As a result there is more curvature from the portion of the shock wave diffracted of the upstream edge, as shown in the three dimensional view, which reduces the gap between the diffracted shock wave and the downstream edge.

Where there is a change in the diffracted shock wave is in the curvature in the Z plane. As the Mach number increases; there is a greater amount of curvature with regards to the horizontal plane (X plane). At Mach 1.32, the curved portion of the diffracted shock wave is fairly level (figure 5.33), however it takes on a bath tub shape at Mach 1.42 (figure 5.81). Whereas at Mach 1.6 there is a sharp dip (figure 5.101). As the Mach number is increased; there is a change in both the shape of the free vortices and diffracted shock wave. The increase in velocity causes the free

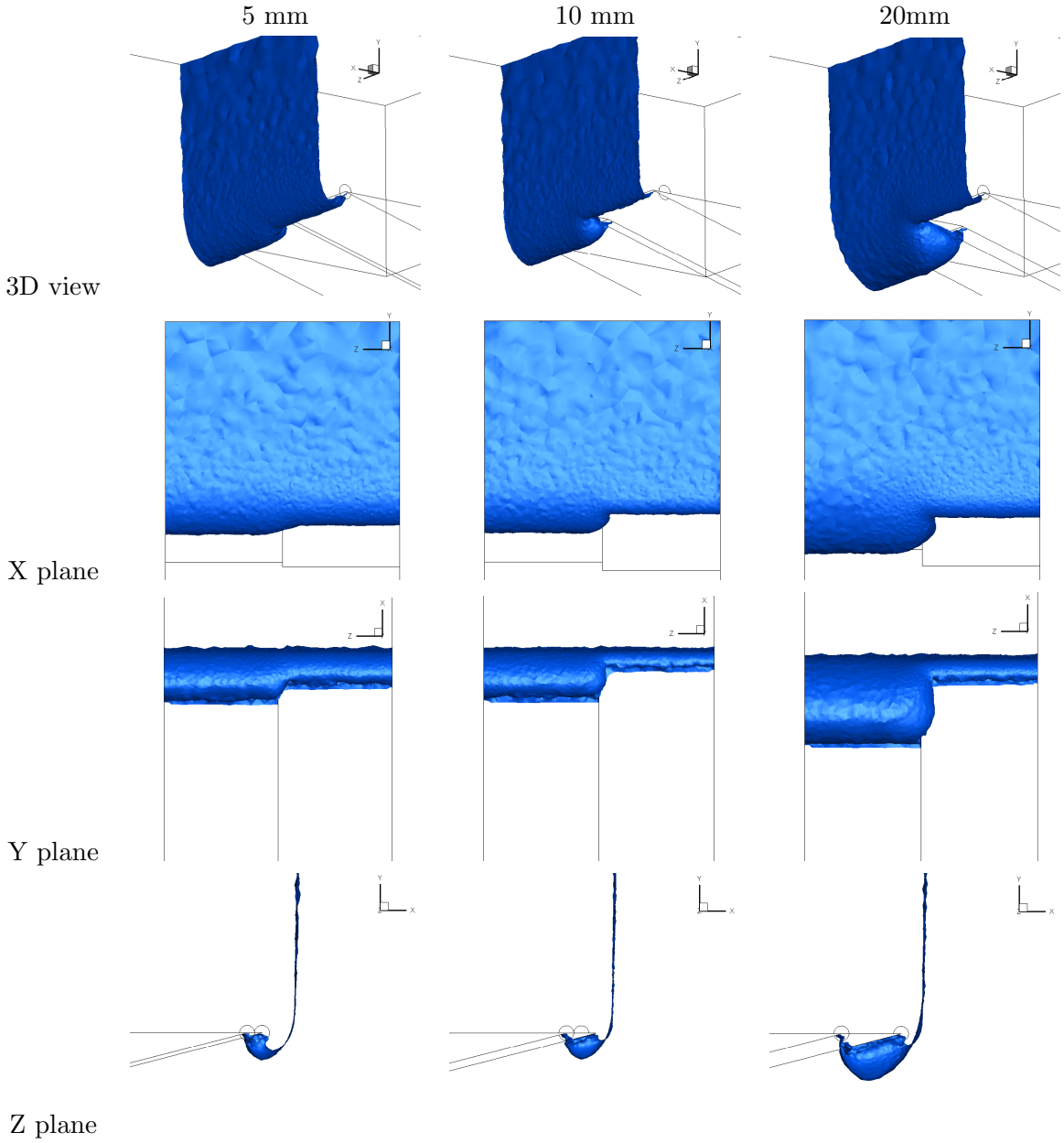

Figure 5.101: Velocity magnitude isosurfaces for Mach 1.6 at a time of $\pm$ 10μs

vortices to become more compact and results in a greater amount of curvature in the diffracted shock wave.

5.5.3 Quantitative Results

The effect of Mach number on the distribution of vorticity magnitude along the z line is given by figure 5.102. As one would expect, the highest Mach number has the highest peak. What is interesting is that on the upstream edge, the larger the Mach number, the smaller the vorticity magnitude. It may simply be the case with

a larger Mach number there is less of a time difference, with regards to the flow between the up and downstream edges. A similar case was seen in the isosurfaces at larger Mach numbers; there was more consistency in the shape of the isosurface on the downstream edge, which may have be as a result of the quicker speed of the flow.

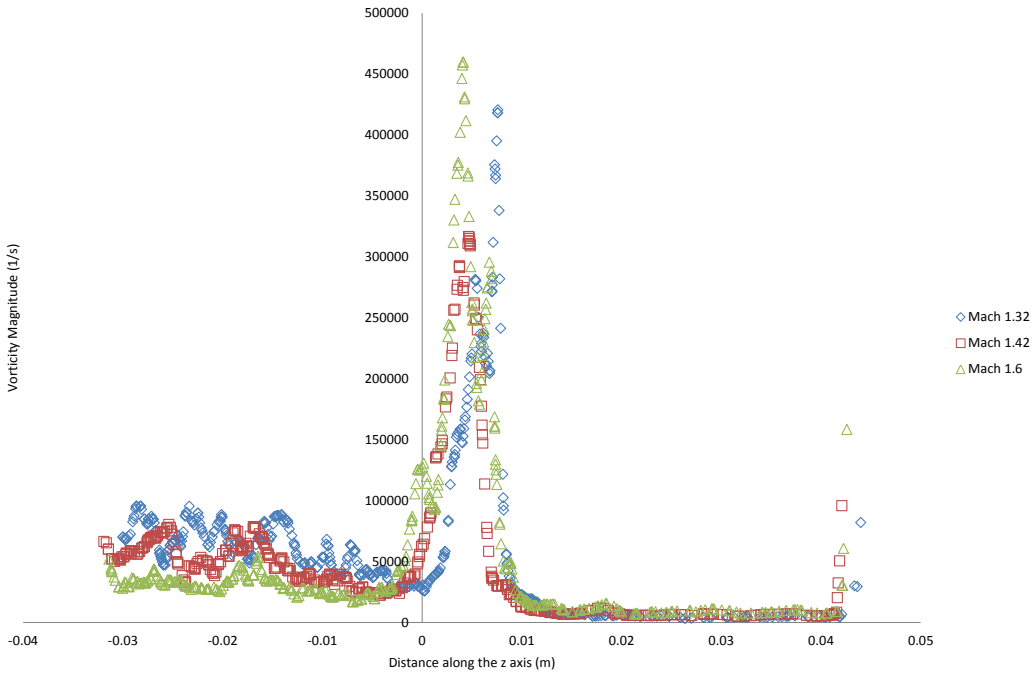

Figure 5.102: Variation of vorticity magnitude along the y line for in the Z plane for the different Mach numbers

The vorticity peak for Mach 1.32 is larger than the peak at Mach 1.42. The peak for Mach 1.32 is slightly to the right in comparison to the remaining peaks. One has to be careful in analysing the data, in that data from a slightly different position can give a different distribution; which may be the reason for the high peak and shift of the peak at Mach 1.32.

The maximum vorticity occurs around the same region for all Mach numbers; on the downstream edge, adjacent to the discontinuity as was the case for the different models. On the downstream edge; all the vorticities effectively tend to zero, which may be an indication of how much or little the flow has developed on the downstream edge.

5.6 Conclusions

The increase in offset edge length caused a number of changes with the vortex flows. The time required for the vortices to merge increased, and the resulting strength of interaction decreased. Once the vortices merged; expansion occurred in the horizontal and vertical directions, with time.

One of the points of interest was the density change of the downstream vortex. There was a significant change in density, in terms of changes in the size of the cross section, at larger offsets. This particular feature was prevalent at lower Mach numbers. Once the Mach number increased, there was more consistency in the density of the downstream vortex. In a sense, an increase in Mach number decreased the effect of the offset edge length.

The rate of vortex expansion is affected by both the Mach number and offset edge length. Both parameters increase the rate of expansion. Therefore the vortices expanded the quickest at Mach 1.6 for the 20mm model.

The maximum vorticity and minimum density occur in similar places for slices taken in the X plane and z line, which is positioned on the downstream edge adjacent to the discontinuity.

At higher Mach numbers there are areas of transonic flow around the diffraction edges. It manifests itself in the flow as shocklets at Mach 1.42 and lambda shock configurations at Mach 1.6.

The diffracted shock wave is not significantly affected by Mach number but by the offset edge length. For a larger offset, the distance between the portion of the diffracted shock wave from the up and downstream edges increase in proportion. The distance remains more or less constant over time.

The topology of the free vortices is consistent along the down and upstream edges. Changes occur in close proximity to and at the offset. There is a major change along the downstream vortex for the 20mm model at Mach 1.32. This effect decreases with decreasing size of the offset and increasing Mach number.

At higher Mach numbers; there are larger spikes in vorticity. The exception was Mach 1.32 which could have been as a result of the data being extracted from a different position in comparison to the remaining Mach numbers.

6 Conclusions and Recommendations

6.1 Conclusions

The study of vortex shedding off a discontinuous edge was investigated by varying two key parameters; the length of the discontinuous edge and the Mach number.

The crux of this study was focused on vortex topology. The increase in size of the discontinuity led to:

The time required for the up and downstream vortices to merge increased. As a result the strength of the interaction between the vortices decreased.

The size of the merged vortex increased in the horizontal and vertical directions, which is an indication of vortex expansion. The vortices expanded at a quicker rate for a larger offset.

At lower Mach numbers the portion of the downstream vortex adjacent to the offset underwent a greater density change than the rest of the vortex structure along the downstream edge. This feature is more prevalent with a larger offset.

The shock wave diffracted over the up and downstream edges. The distance between the portion diffracted over the up and downstream edges increased with size of the offset.

The maximum vorticity and minimum density occur in similar places for slices taken in the X plane and z line, which is positioned on the downstream edge adjacent to the discontinuity.

The vortex topology was also affected by the increase in Mach number:

Reeves (2010) found that for three dimensional flows; the shear layer lengthened, the vortices became more elliptical in profile. The same observations were seen in

this study, although there was an increase in curvature of the diffracted shock wave.

There was a greater portion of transonic flow around the diffraction edges; which was seen as shocklets at Mach 1.42 and lambda shock configurations at Mach 1.6.

The rate of vortex expansion increased.

There is more consistency in terms of structure and shape of vortices along the diffraction edges. There is less of a change in density of the downstream vortex adjacent to the offset, for all models.

There are larger spikes in vorticity. The exception was Mach 1.32 which could have been as a result of the data being extracted from a different position in comparison to the remaining Mach numbers.

6.2 Recommendations

Three dimensional vortex flows can be investigated as a result of shapes that have not been investigated to date, i.e. curved surfaces; particularly aerofoils. The arrangement could be aerofoils side by side with an offset, a study such as this will aid the field of supersonic aerodynamics. The angle of attack can also be altered.

Design and test pieces with a larger offset edge length then 20mm, in order to investigate when the vortices will behave independently. A few cases can be tested experimentally; i.e. 25mm, 30mm and 35mm. However the exact point at which independent behaviour occurs is best investigated computationally.

If access can be gained to a computer with exceptional power; then a refined quadrilateral mesh can be implemented. Combined with mesh adaption techniques, a resolution equivalent to or even greater than the vortices along the diffraction edges with the unstructured triangular mesh can be achieved. In addition other flow features such as the diffracted shock wave will have a higher resolution; as it was with the cases investigated.

Test the current design models at higher Mach numbers to see when secondary and tertiary shocks appear. A key Mach number is Mach 1.65, since at this Mach number Reeves (2010) identified secondary and tertiary shocks. An alternative suggestion is to use schlieren imaging at Mach 1.6, and even at higher Mach numbers.

REFERENCES

Cooppan, S. (2011). Final Year Project - Vortex Shedding from Impulsive Flow over a Discontinuous Edge. Johannesburg: University of Witwatersrand.

Daya, S. (2009). Final Year Project - Low Reynolds Number Vortex Flows. Johannesburg: University of Witwatersrand.

Elsayed, O. A., Omar, A. A., Asrar, W. & Kwon, K. (2011). Effect of Differential Spoiler Settings (DSS) on the Wake Vortices of a Wing at High-Lift Coefficients. *Aerospace Science and Technology*, **Vol. 15**, Issue. 7, 555-566.

Gerz, T. & Ehret, T. (1997). Wingtip Vortices and Exhaust Jets during the Regime of Aircraft Wakes. *Aeropsace Science and Technology*, **Vol. 1**, Issue. 7, 463-474.

Green, S. O. (1995). Fluid Vortices. Kulwer Academic Publishers. **Chapters I** & **VII**, 1-31 and 291-303.

Hall, M. G. (1965). The Structure of Concentrated Vortex Cores. *Royal Aircraft Establishment*. Farnborough. Hampshire.

Lee, S. & Bershader, D. (1994). The structure of compressible starting vortices. *Experiments in Fluids*. **Vol. 16**. 248-254

Reeves, J. O. (2010). MSci Eng Thesis - Unsteady three-dimensional Compressible Vortex Flows. Johannesburg: University of Witwatersrand.

Ripley, R. C., Lien, F. S. & Yovanovich, M. M. (2006). Numerical simulation of shock diffraction on unstructured meshes. *Computers & Fluids*, **Vol. 35**, 1420-1431.

Skews, B. W. (1966). PhD Thesis - Shock Wave Diffraction. Johannesburg: University of Witwatersrand, **Vol. 1**.

Skews, B. W. (1966). PhD Thesis - Shock Wave Diffraction. Johannesburg: University of Witwatersrand, **Vol. 2**.

Sun, M. & Takayama, K. (1996). The formation of a Secondary Shock Wave behind a Shock Wave Diffracting at a Convex Corner. *Shock Waves*, **Vol. 7**, 287-295.

Sun, M. & Takayama, K. (2002). Vorticity production in Shock Diffraction. *J. Fluid Mechanics*, **Vol. 478**, 237-256.

Sun, M. & Takayama, K. (2003). A note on simulation of vortical structures in shock diffraction. *Shock Waves*, **Vol. 13**, 25-32.

Takayama, K. & Inoue, O. (1991). Shock wave diffraction over a 90 degreesharp corner - Poster presented at 18th ISSW. *Shock Waves*. **Vol. 1**. 301-312.

APPENDIX A Apparatus Specifications

Seitz Shock tube (all dimensions in mm)

Table A.1: Seitz Shock tube specifications

Test Section	$180 \times 76 \times 350$
Expansion Chamber	$6000 \times 180 \times 76$
Compression Chamber	2000×300(internal diameter)
Viewing window thickness and diameter	250×55

Compression Chamber

Table A.2: Compression Chamber specifications

Design Pressure	2000kPa
Hydrostatic Pressure tested to	3000kPa
Design Temperature	50°C
Capacity	$0.155m^3$

Electric Motor

Table A.3: Electric Motor specifications

Siemens Three Phase Motor	50Hz, 7Amps, 3kW
Squirrel Cage Induction Motor	

Optics

Table A.4: Optics specifications

Xenon Light Source	Hamamatsu
Light Source Power Box	Serial No:91050364
Parabolic Mirror (diameter)	254mm
Camera	12MP Fujifilm S3 Serial Number:62903532